Title
A Finite Element Method for Modeling Surface Growth and Resorption of Deformable Bodies with Applications to Cell Migration

Author
Bergel, Guy Leshem

Publication Date
2019

Peer reviewed|Thesis/dissertation

A Finite Element Method for Modeling Surface Growth and Resorption of Deformable Bodies with Applications to Cell Migration

by

Guy Leshem Bergel

A dissertation submitted in partial satisfaction of the

requirements for the degree of

Doctor of Philosophy

in

Civil and Environmental Engineering

in the

Graduate Division

of the

University of California, Berkeley

Committee in charge:

Professor Panayiotis Papadopoulos, Co-chair
Professor Robert L. Taylor, Co-chair
Professor Sanjay Govindjee
Professor Per-Olof Persson

Spring 2019

Abstract

A Finite Element Method for Modeling Surface Growth and Resorption of Deformable Bodies with Applications to Cell Migration

by

Guy Leshem Bergel

Doctor of Philosophy in Civil and Environmental Engineering

University of California, Berkeley

Professor Panayiotis Papadopoulos, Co-chair

Professor Robert L. Taylor, Co-chair

Surface growth/resorption is the process wherein material is added to or removed from the boundary of a physical body. As a consequence, the set of material points constituting the body is time-dependent and thus lacks a static reference configuration. In this dissertation, kinematics and balance laws are formulated for a body undergoing surface growth/resorption and finite deformation. This is achieved by defining an evolving reference configuration termed the intermediate configuration which tracks the set of material points constituting the body at a given time.

An extension of the Arbitrary Lagrangian-Eulerian finite element method is introduced to solve the discretized set of balance laws on the grown/resorpted body, alongside algorithmic implementations to track the evolving boundary of the physical body. The effect of accreting material with no prior history of deformation onto a body undergoing rigid motions as well as a loaded body is discussed. Moreover, the correlation between growth/resorption rate and the spatial and temporal convergence of the finite element approximations of fields are illustrated.

The numerical implementation for surface growth and resorption is used to simulate a migrating cell which moves in an apparent "treadmilling" motion on a substrate by polymerizing and depolymerizing microfilaments along its boundary. An example is presented which defines a surface growth law based on the nucleation and dissociation of chemical species, and the steady-state treadmilling velocity is computed for various assumed cell shapes. Lastly, simulation results are shown for an idealized cell colliding with external barriers, leading to a re-orientation of the surface growth/resorption direction. The effects of dynamic contact on the surface growth/resorption as well as the stress and deformation are discussed.

Contents

List of Figures

List of Tables

List of Algorithms

List of Symbols

$\mathcal{A}^{\tau+t}$	Domain consisting of ablated/resorpted material points at an elapsed time $\tau+t$ relative to the reference time τ
$\boldsymbol{F}$	Total deformation gradient
$\boldsymbol{F}_{\tau+t_g}^{\tau+t}$	Incremental deformation gradient at time $\tau+t$ relative to $\tau+t_g$
$\mathcal{G}^{\tau+t}$	Domain consisting of accreted material points at an elapsed time $\tau+t$ relative to the reference time τ
J	Determinant of the deformation gradient
$\mathcal{M}^{\tau+t}$	Domain consisting of material points that are neither accreted nor resorpted at an elapsed time $\tau+t$ relative to the reference time τ
$\boldsymbol{Q}$	Non-equilibrium (viscous) stress in the reference configuration
$\mathcal{R}^{\tau}$, $\mathcal{R}^{\tau+t}$	Set of material points comprising the body in the spatial configuration at reference time τ and elapsed time $\tau+t$
$\tilde{\mathcal{R}}^{\tau+t}$	Set of material points comprising the body in the intermediate configuration at time $\tau+t$
$\boldsymbol{S}$	Second Piola-Kirchhoff stress tensor
$\boldsymbol{T}$	Cauchy stress tensor
$\mathbf{V}$	Cell treadmilling velocity
$\boldsymbol{n}$	Outward unit normal in the current configuration
$\tilde{\boldsymbol{n}}$	Outward unit normal in the intermediate configuration
$\boldsymbol{t}$	Traction vector in the current configuration
$\boldsymbol{u}$	Material displacement vector
$\mathbf{v}$	Material velocity vector

$\mathbf{v}_g$	Growth/Resorption velocity vector at a point along the domain boundary
$\mathbf{x}$	position vector of material point in the spatial configuration
$\tilde{\mathbf{x}}$	position vector of material point in the intermediate configuration
Γ_a	Domain of the boundary undergoing surface ablation/resorption
Γ_g	Domain of the boundary undergoing surface growth
Δt	Time increment
Ψ	Helmholtz free energy
Ω	Spatially discretized domain in the current configuration
$\tilde{\Omega}$	Spatially discretized domain in the intermediate configuration
ρ	Material density
φ	Surface-bound variable such as G-actin concentration
χ_d	Mapping of material points from reference/material configuration to current/spatial configuration
χ_g	Mapping of boundary from reference/material configuration to intermediate configuration
$\overline{\chi}_g$	Mapping of material points from initial location and time of existence to intermediate configuration

Chapter 1

Introduction

1.1 Motivation and Prior Works

Surface growth and resorption occur in numerous biological phenomena and engineering applications, such as the accretion of seashells and antelope horns [1, 2], bone erosion [3], electrodeposition [4], epitaxial growth of thin films [5], built-up structures [6], and metal solidification [7]. In contrast to volumetric growth where addition of mass is manifested through a global balance law that modifies the density of material points, surface accretion or resorption uniquely define the evolution of the boundary in terms of the addition or removal of finite layers of mass [8].

Among the first works on surface accretion of elastic bodies, [9] studied a simple example of an isotropic linear elastic sphere subjected to an incrementally increasing self-weight as each layer is deposited over time. The authors in [9] note that the accretion of layers onto a loaded body introduces a discontinuity in the stress along the newly formed interface. The continuity of material along the growth interface implies that the body must contain residual stresses upon unloading, as shown in Figure 1.1. The authors conclude that the state of the body at any given time depends on the manner in which material is deposited onto its surface, and is thus incremental in nature. The same notion of stress discontinuities was introduced in [10] by constructing a hypothetical case where an arbitrary subdomain of an infinite elastic medium is cut, and subsequently endowed with a displacement relative to its parent domain. A state of self stress is subsequently generated once the domains are re-connected. Both [9] and [10] arrived at the same conclusion that material placed onto a deformed or loaded body can introduce residual stress in order to fit without any gaps or overlaps.

The authors in [11] and [12] postulate that the formation of residual stresses due to layered accretion introduces energy that can only be released by cutting the body into disjoint parts. Although the spatial representation of a simply connected body at any fixed point in time consists only of continuous material without overlaps or holes, its corresponding stress-free reference configuration contains disjoint segments. This implies that a mapping between configurations cannot solely rely on the reference coordinates of a material point. A classic hypothetical example supporting this claim was constructed in [13]. Suppose a sphere is accreting layers on its boundary while simultaneously undergoing a compressive pressure. If the displacement due to the applied

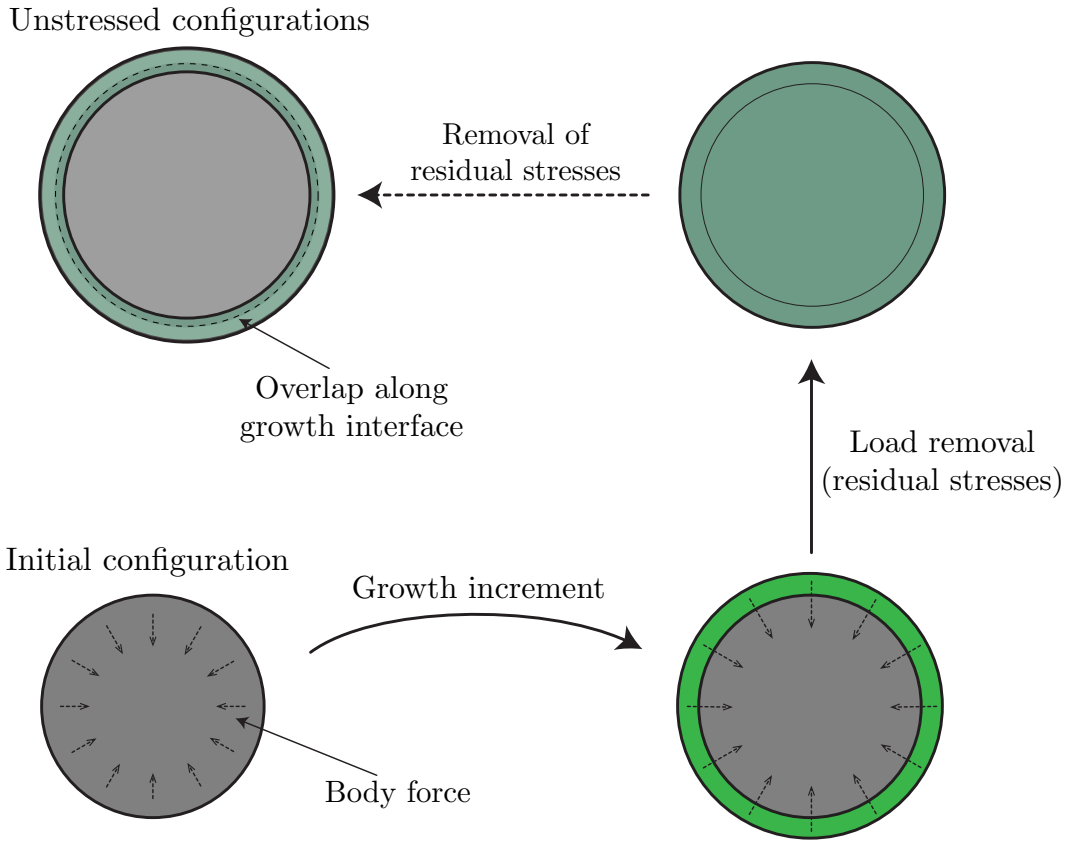

Figure 1.1: *Residual stresses resulting from the self-gravitation of an accreting sphere*

pressure is equal and opposite to that of the accreting growth, the boundary will remain stationary. This example indicated that the spatial coordinates of an accreted layer at the time of attachment are thus not a valid identifier of its reference configuration. The work in [14] separately came to the same conclusion by asserting that cases where material is either attached to the same point in space at different times, or is continuously deposited at the same point, define a reference configuration that cannot be described by conventional Lagrangian mechanics. Both works argued that deformation mappings must inherit information about the accretion history of a physical body, such as the time of existence of a given material point. Various other notable works constructed similar arguments to define the current state of an accreting body with respect to its growth history. Both [15] and [1] assert similar claims to that of [14] and [13], namely that the spatial representation of an accreting body must necessarily have a time-dependent component which captures the history of growth in some sense. In [16], concepts of mixture theory were used to justify the use of a "natural" stress-free configuration, with similar ramifications as those stated in [11] and [12]. Additionally, [7] and [17] argue that the spatial description of a growing body can be represented by rate-type constitutive and kinematic laws that obey certain properties such as non-dissipativeness.

Although a complete theory of surface growth and resorption remains largely elusive, various numerical and analytical examples that capture these effects have been successfully implemented. The work in [18] introduces a kinematic description of discrete accretion and resorption increments

on the surface of deformable bodies based on the theory of the Arbitrary Lagrangian-Eulerian (ALE) finite element method as described in [19]. This technique is implemented in [20] and [21] to simulate a one-dimensional treadmilling cell. These works provide a fundamental basis for describing discrete kinematics of a body undergoing surface growth with an emphasis on an ALE finite element implementation, and hence is of particular importance to the theory and fundamentals presented herein. The work of [6] analyzes the effects of surface growth on a winding composite cylinder undergoing finite deformation. In [22], balance laws are derived for a rigid body undergoing surface growth, and applies the theory to a snowball rolling downhill. In [23], various closed-form solutions of the boundary-value problem of an accreting body are formulated. These authors define a material metric tensor that characterizes the coupling between growth and deformation, and subsequently analyze the residual stress profile of an accreting cylinder in plane strain. The works of [24, 3, 25, 26] developed a thermomechanical set of balance laws based on concepts from configurational mechanics, and applied the formulations to model the accretion of antlers triggered by nutrients, as well as bone erosion and ossification. In [27, 4, 5], numerical methods are developed that utilize an Eulerian grid to solve a global set of boundary-value problems while tracking the growth and resorption front using the level set method. Examples implemented in these works include etching, lithography, electrodeposition of copper, and epitaxial growth of thin films.

1.2 Objectives and Outline

The current work offers a general approach to simulating complex surface growth/resorption phenomena on deformable bodies without restrictions on the geometry of the domain that exist in the prior implementations of [18, 20]. The primary goals of the current work are as follows:

- Formulate a kinematic description and finite element implementation that can capture the evolution in the shape of a two-dimensional body undergoing surface growth/resorption,
- Demonstrate the effect of surface growth/resorption on the stresses and deformations within the body,
- Assess the spatial and temporal convergence properties for a body undergoing surface growth/resorption and finite deformation,
- Apply the proposed algorithm to cell migration.

The preliminary framework in Chapter 2 introduces the kinematics and balance laws of a deformable body undergoing surface growth/resorption. In Chapter 3, the weak forms of the balance laws are presented, and the spatial and temporal discretizations are formulated. The general algorithmic procedure is described within the framework of the Arbitrary Lagrangian-Eulerian (ALE) finite element method. Additionally, examples are presented that demonstrate consistency for a growing/resorpting body undergoing rigid motions, and the spatial and temporal convergence rates of a hollow elliptical cylinder with an imposed internal pressure and surface

growth or resorption on the outer surface. In Chapter 4, the biological phenomenon of cell migration is introduced. The dynamics and kinetics that drive cell movement are described in terms of the molecular interactions, and its correlation to the observed cell motion is highlighted within the context of surface growth and resorption. Furthermore, simulation results are presented that correlate the evolution of chemical concentrations of a surface-bound variable to cell shape. The last such example features an idealized migrating cell encountering multiple barriers. The examples in this chapter demonstrate the usefulness of the proposed algorithms in solving complex surface growth/resorption problems occurring in real-world phenomena. A summary of the findings from the work presented in this dissertation as well as potential future extensions of the current research are discussed in Chapter 5. The details of the algorithmic implementation are provided in Appendix A, and the structure of the code used to produce the results is highlighted in Appendix B.

Chapter 2

Continuum Mechanics of Surface Growth and Resorption

2.1 Overview

In this chapter, the physical characteristics of a body undergoing surface growth/resorption and deformation are introduced. A kinematic description of a growing and deforming body is defined in Section 2.2. Additionally, the physical balance laws are introduced in their global and local forms in Section 2.3 in the context of a growing/resorpting deformable body. Lastly, the notion of extended fields in the newly grown and accreted regions is described and the associated initial/boundary-value problem is stated.

2.2 Kinematics

Consider a physical body which is elastically deforming while simultaneously exchanging mass with the surrounding region through its boundary. In such a setting, material that is passing through the boundary ultimately alters the region which constitutes the body. The motion of material points must hence be defined relative to an evolving reference configuration due to the fact that the existence of these points within the body is itself time-dependent. In the ensuing developments, the motion of a body undergoing concurrent surface growth/resorption and deformation will be defined in terms of an evolving reference configuration termed the intermediate configuration.

The domain of a body with imposed surface growth and resorption is defined in the three-dimensional Euclidean point space $\mathcal{E}^3$ at the reference time τ and current time $\tau + t$ as $\mathcal{R}^\tau$ and $\mathcal{R}^{\tau+t}$, respectively. The superscripts τ and $\tau + t$ denote the time associated with a specific configuration or variable. The position vectors of particles in $\mathcal{R}^\tau$ and $\mathcal{R}^{\tau+t}$ are denoted $\mathbf{x}^\tau$ and $\mathbf{x}^{\tau+t}$, respectively. The part of the reference domain boundary that undergoes surface growth is denoted Γ_g^τ; the part that undergoes surface resorption is denoted Γ_a^τ, where it naturally follows that $\Gamma_g^\tau \cap \Gamma_a^\tau = \emptyset$. The set containing all portions of the boundary undergoing surface growth and/or resorption is denoted $\partial\mathcal{R}_g^\tau = \overline{\Gamma_g^\tau \sqcup \Gamma_a^\tau}$, where the symbol $\sqcup$ denotes the disjoint union.

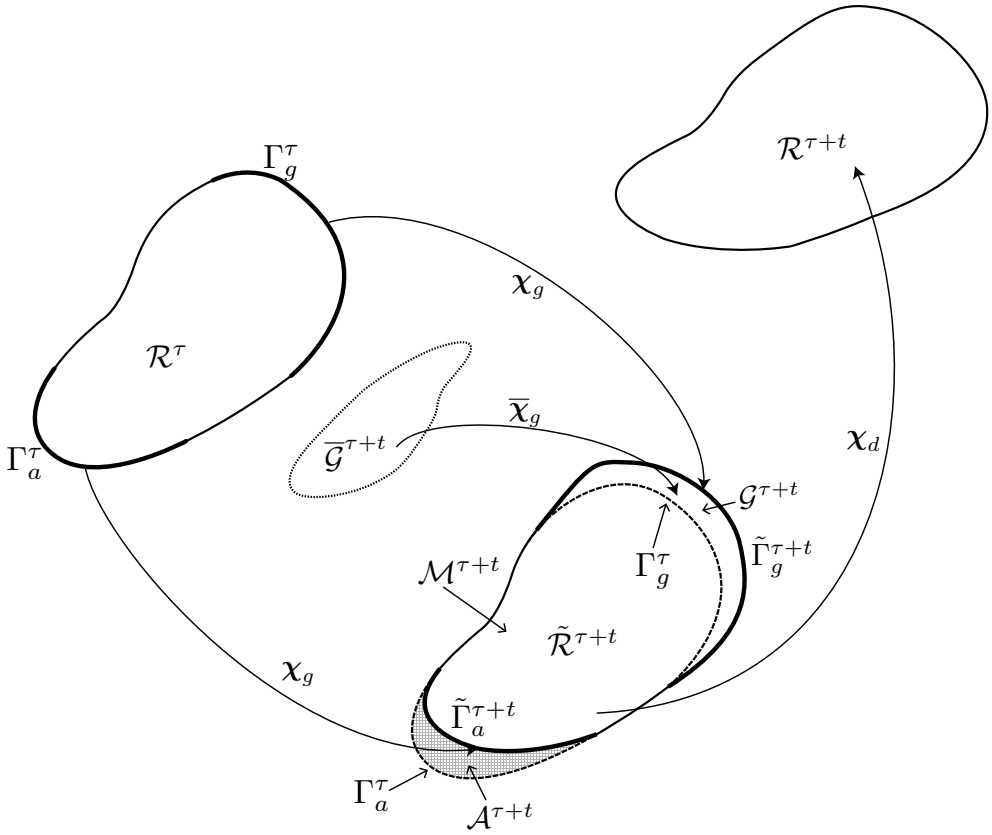

Figure 2.1: *Kinematics of surface growth*

As shown in Figure 2.1, surface growth and resorption is characterized by a diffeomorphic boundary transformation defined as $\boldsymbol{\chi}_g : \partial\mathcal{R}^\tau \times \mathbb{R} \mapsto M^2$. This mapping results in a new boundary $\partial\tilde{\mathcal{R}}^{\tau+t}$, which encloses a volume $\tilde{\mathcal{R}}^{\tau+t}$ termed the intermediate configuration. The resulting surface, M^2, is a simply connected two-dimensional manifold embedded in $\mathcal{E}^3$, and represents the positions along the intermediate configuration boundary $\partial\tilde{\mathcal{R}}^{\tau+t}$. The mapping $\boldsymbol{\chi}_g$ is assumed to be bijective, hence the growth and resorption surfaces remain always disjoint. Moreover, the portion of the boundary which does not undergo surface growth/resorption remains unaltered, and hence $\boldsymbol{\chi}_g$ maps these points to their identical positions.

As a consequence of the surface transformation, the interior of the intermediate configuration contains a subset of material points that did not exist in $\mathcal{R}^\tau$, which constitute the domain of the growth region $\mathcal{G}^{\tau+t}$. The homeomorphism $\overline{\boldsymbol{\chi}}_g : \overline{\mathcal{G}}^{\tau+t} \times \mathbb{R} \mapsto \mathcal{E}^3$ maps each grown material point from its initial time of existence $\tau + t_g \in (\tau, \tau + t]$ and position $\mathbf{x}^{\tau+t_g}$ to its location in the grown region $\mathcal{G}^{\tau+t}$ of the intermediate configuration. The manifold $\overline{\mathcal{G}}^{\tau+t}$ is a simply-connected three-dimensional surface embedded in a four-dimensional space-time (the time dimension signifies the progression of surface growth, which is assumed to be continuous) which is formed by new material as it is extruded along the direction of growth. Its image formed by $\overline{\boldsymbol{\chi}}_g$ generates a growth region in the intermediate configuration which is defined purely through its spatial position in $\mathcal{E}^3$. The

subset of points that were contained within the interior of $\mathcal{R}^\tau$ and are now outside the boundary of $\tilde{\mathcal{R}}^{\tau+t}$ defines the resorption domain $\mathcal{A}^{\tau+t}$ in the intermediate configuration. The region that remains unaltered by χ_g is denoted $\mathcal{M}^{\tau+t}$. The two-dimensional manifold Γ_g^τ separates the unaltered domain $\mathcal{M}^{\tau+t}$ and growth domain $\mathcal{G}^{\tau+t}$. The intermediate configuration can be formally defined as

$$\tilde{\mathcal{R}}^{\tau+t} = \overline{\mathcal{G}^{\tau+t} \sqcup \mathcal{M}^{\tau+t} \sqcup \Gamma_g^\tau} \,. \tag{2.1}$$

A unique characteristic of the intermediate configuration is that it contains subdomains that have reference configurations defined at different times. For instance, the set of material points in $\mathcal{M}^{\tau+t}$ is always defined by the material existing at time τ. In contrast, $\mathcal{G}^{\tau+t}$ contains material that has come into existence at varying times in the range $(\tau, \tau + t]$. Although these regions accrete at different times, together they form the intermediate configuration as a continuous manifold in $\mathcal{E}^3$ which evolves only when material accretes or resorpts through its boundary.

The intermediate configuration introduces a means of tracking and evolving the boundary of a growing/resorpting body independent of other sources of motion such as elastic deformation. Through this definition of an evolving reference configuration, it can be assumed that variables associated with material points can be continuously mapped to the spatial configuration $\mathcal{R}^{\tau+t}$. This notion of a configuration constituting the grown and existing material in an intermediate state was similarly explored in prior works. For instance, [23] defines a material manifold endowed with its own metric which describes the combined history of surface growth and deformation. Moreover, the associated manifold defined in [13] corresponds to an arbitrary intermediate domain in which both pre-existing and grown material form a continuum corresponding to the evolving reference configuration.

The deformation of the physical body is defined as the homeomorphism $\chi_d : \tilde{\mathcal{R}}^{\tau+t} \times \mathbb{R} \mapsto \mathcal{E}^3$. It can be reasonably assumed that this mapping has the conventional properties of being bijective since the configurations $\tilde{\mathcal{R}}^{\tau+t}$ and $\mathcal{R}^{\tau+t}$ share the same material points. The total motion occurring in the interval $(\tau, \tau + t]$ which includes both deformation and surface growth is defined as

$$\chi = \begin{cases} \chi_d & \text{in } \mathcal{M}^{\tau+t} \\ \chi_d \circ \overline{\chi}_g & \text{in } \mathcal{G}^{\tau+t} \\ \text{undefined} & \text{in } \mathcal{A}^{\tau+t} \end{cases} , \tag{2.2}$$

where the $\circ$ symbol is defined as the functional composition, emphasizing that χ depends on the motion of material between $\tilde{\mathcal{R}}^{\tau+t}$ and $\mathcal{R}^{\tau+t}$, as well as between $\overline{\mathcal{G}}^{\tau+t}$ and $\mathcal{G}^{\tau+t}$ for accreted material points. To ensure continuity of material, the total motion also maintains continuity along the growth interface, *i.e.*,

$$[\![\chi]\!] = 0 \qquad \text{on } \Gamma_g^\tau \,, \tag{2.3}$$

where $[\![\chi]\!]$ denotes the Euclidean vector norm of the difference in the material motion across a given surface. In enforcing the continuity of the motion along the growth interface, it is inherently assumed that material accretes onto the surface without having to deform at the instant of attachment.

From a practical perspective, the motion defined in Equation (2.2) implies that any given material point which comes into existence at time $\tau + t_g \in (\tau, \tau + t]$ with initial position $\mathbf{x}^{\tau+t_g}$ must

have an associated mapping $\overline{\boldsymbol{\chi}}_g$ that is explicitly prescribed based on an assumed knowledge of prior deformation induced on the body within the range $(\tau, \tau + t_g]$. In order to properly describe the deformation at the current time $\tau + t$, the transformation $\boldsymbol{\chi}_d$ must therefore map the material point and its associated initial position $\mathbf{x}^{\tau+t_g}$ (through the dependence on $\overline{\boldsymbol{\chi}}_g$) to its current spatial position $\mathbf{x}^{\tau+t}$. Consequently, at a given position $\mathbf{x}^{\tau+t_g}$, the mapping $\boldsymbol{\chi}_d$ is defined locally with respect to the physical configuration of the body as it appears at the instant of time $\tau + t_g$ at which the material point comes into existence.

The incremental deformation gradient $\boldsymbol{F}^{\tau+t}_{\tau+t_g}$ is defined as the tensor that maps a tangent vector of a material point at the location $\mathbf{x}^{\tau+t_g}$ and configuration corresponding to its initial time of existence in the closed interval $\tau + t_g \in [\tau, \tau + t]$ to the current configuration $\mathcal{R}^{\tau+t}$, and hence takes the following form:

$$\boldsymbol{F}^{\tau+t}_{\tau+t_g} = \begin{cases} \frac{\partial \boldsymbol{\chi}_d}{\partial \mathbf{x}^{\tau}} & \text{in } \mathcal{M}^{\tau+t} \\ \frac{\partial \boldsymbol{\chi}_d}{\partial \tilde{\mathbf{x}}^{\tau+t}} \frac{\partial \overline{\boldsymbol{\chi}}_g}{\partial \mathbf{x}^{\tau+t_g}} & \text{in } \mathcal{G}^{\tau+t} \\ \text{undefined} & \text{in } \mathcal{A}^{\tau+t} \\ \text{undefined} & \text{on } \Gamma_g^{\tau} \end{cases} . \tag{2.4}$$

The superscript and subscript times in the deformation gradient defined in Equation (2.4) denote the reference time associated with the point $\mathbf{x}^{\tau+t_g}$, and the current time $\tau + t$, respectively. For material in the growth region $\mathcal{G}^{\tau+t}$, the gradient of $\overline{\boldsymbol{\chi}}_g$ is taken with respect to the coordinates defining the physical body at the reference time $\tau + t_g$. Therefore, the deformation gradient of an accreted material point at the current time $\tau + t$ which comes into existence at time $\tau + t_g$ depends on its deformation occurring relative to the configuration of the body at $\tau + t_g$.

A variant of the kinematics as presented in [18] maps the physical deformation $\boldsymbol{\chi}_d$ from the reference configuration onto the intermediate configuration, and $\boldsymbol{\chi}_g$ maps the surface of the intermediate configuration to the current configuration based on the applied surface growth and/or resorption. The inherent assumption is that the grown region simply attaches to the body in a stress-free state with no initial deformation. Here, the current configuration $\mathcal{R}^{\tau+t}$ accounts for all deformation occurring in the interval $(\tau, \tau + t]$ in both the grown and ungrown domains $\mathcal{M}^{\tau+t}$ and $\mathcal{G}^{\tau+t}$, respectively. In the present context, the intermediate configuration simply tracks the set of material points at a given time, and thus does not correspond to an ungrown deformed state as it does in [18].

The material displacement of a given point at the current time $\tau + t$ relative to its position at the initial time of existence is defined as

$$\boldsymbol{u}^{\tau+t}_{\tau+t_g} = \begin{cases} \boldsymbol{\chi} - \mathbf{x}^{\tau} & \text{in } \mathcal{M}^{\tau+t} \\ \boldsymbol{\chi} - \mathbf{x}^{\tau+t_g} & \text{in } \mathcal{G}^{\tau+t} \\ \text{undefined} & \text{in } \mathcal{A}^{\tau+t} \end{cases} . \tag{2.5}$$

In the case where the initial deformation just after τ occurs simultaneously with the initial surface growth/resorption on Γ_g^{τ} and Γ_a^{τ}, the jump in the material displacement vanishes along the Γ_g^{τ}, that is,

$$[\![\boldsymbol{u}^{\tau+t}_{\tau+t_g}]\!] = 0 \quad \text{on } \Gamma_g^{\tau} . \tag{2.6}$$

The jump condition in Equation (2.6) does not hold when the initial configuration $\mathcal{R}^\tau$ is in a deformed state since material is assumed to accrete onto the boundary without any prior history of deformation. This scenario results in a discontinuity in the material displacement along the initial growth interface Γ_g^τ. Such a setting naturally occurs in the discretization of surface growth/resorption, and is elaborated in greater detail in Section 3.5.

The material velocity is defined as the material time derivative (fixing the coordinates $\mathbf{x}^\tau$ for points in $\mathcal{M}^{\tau+t}$ and $\mathbf{x}^{\tau+t_g}$ for points in $\mathcal{G}^{\tau+t}$) of the total motion

$$\mathbf{v} = \frac{d\boldsymbol{\chi}}{dt} \,. \tag{2.7}$$

In Equation (2.7), d/dt denotes the material time derivative. Neglecting the presence of shock waves, and assuming that surface growth and resorption are continuous in time, the jump in the material velocity likewise vanishes on Γ^τ, that is,

$$[\![\mathbf{v}]\!] = 0 \qquad \text{on } \Gamma_g^\tau \,. \tag{2.8}$$

The growth/resorption velocity is defined as

$$\mathbf{v}_g \;=\; \frac{d\boldsymbol{\chi}_g}{dt} \,. \tag{2.9}$$

Growth is defined to occur when $\mathbf{v}_g \cdot \tilde{\boldsymbol{n}} > 0$ and resorption occurs when $\mathbf{v}_g \cdot \tilde{\boldsymbol{n}} < 0$, where $\tilde{\boldsymbol{n}}$ is the outward-facing unit normal vector on $\partial\tilde{\mathcal{R}}^{\tau+t}$. The surface motion $\boldsymbol{\chi}_g$ results in a net mass change rate of

$$\frac{dM}{dt} \;=\; \int_{\partial\tilde{\mathcal{R}}^{\tau+t}} \tilde{\rho}\mathbf{v}_g \cdot \tilde{\boldsymbol{n}} \; da \,, \tag{2.10}$$

where $\tilde{\rho}$ is the mass density in $\tilde{\mathcal{R}}^{\tau+t}$.

2.3 Balance Laws

The current configuration resembles a physical body in the traditional sense where each material point in the domain is associated with an inverse mapping to a single point in a given reference configuration, which in the case of surface growth, is the intermediate configuration $\tilde{\mathcal{R}}^{\tau+t}$. It is therefore convenient to derive the physical balance laws in the current configuration. Note that although the material itself is continuous along the initial growth interface Γ_g^τ, no such continuity requirement exists for the deformation gradient defined in Equation (2.4). The balance laws are thus not well-defined on Γ_g^τ, and are assumed to hold only in $\mathcal{M}^{\tau+t}$ and $\mathcal{G}^{\tau+t}$ [1]. It is assumed that all time-dependent variables are evaluated at time $\tau + t$, and the superscript and subscript times will be selectively omitted for brevity when possible.

The mass density ρ is defined as a local measure at a given spatial position $\mathbf{x}$ in the current

[1] Discontinuities in the deformation gradient along the growth interface are approximated by steep gradients in the discretized setting (as elaborated in Chapter 3), and thus lead to well-defined global balance laws.

configuration $\mathcal{R}^{\tau+t}$ through the limit

$$\rho = \lim_{\delta \to 0} \frac{m(\mathcal{L}_\delta)}{vol(\mathcal{P}_\delta)} \,, \tag{2.11}$$

where $m(\mathcal{L}_\delta)$ is the mass of the region $\mathcal{L}_\delta \subset \mathcal{R}^{\tau+t}$ defined as

$$m(\mathcal{L}_\delta) = \int_{\mathcal{L}_\delta} dm = \int_{\mathcal{L}_\delta} \rho \, dv \,, \tag{2.12}$$

and $vol(\mathcal{P}_\delta)$ is the volume of a sphere $\mathcal{P}_\delta \subset \mathcal{E}^3$ centered at $\mathbf{x}$ with radius $\delta > 0$. The mass density in Equation (2.11) characterizes the mass per current volume of a given material point existing in $\mathcal{R}^{\tau+t}$. In principle, the accreting material has no knowledge of the mass density near the boundary of the existing body. Therefore, ρ is not well-defined on the growth boundary Γ_g^τ since its value can be discontinuous along this interface.

Considering an arbitrary volume $\mathcal{P} \subset \mathcal{R}^{\tau+t}$, global mass balance is stated as

$$\begin{aligned} \frac{d}{dt} \int_{\mathcal{P}} \rho \, dv &= \int_{\bar{\mathcal{P}}} \left(\frac{d\rho}{dt} + \rho \, \mathrm{div}\mathbf{v} \right) J \, d\bar{v} \\ &= \int_{\mathcal{P}} \left(\frac{d\rho}{dt} + \rho \, \mathrm{div}\mathbf{v} \right) dv = 0 \,. \end{aligned} \tag{2.13}$$

Here, J is the determinant of the deformation gradient defined in Equation (2.4), $\bar{\mathcal{P}} \subset \tilde{\mathcal{R}}^{\tau+t} \sqcup \overline{\mathcal{G}}^{\tau+t}$, and $d\bar{v}$ is the differential volume of a material region in $\tilde{\mathcal{R}}^{\tau} \sqcup \overline{\mathcal{G}}^{\tau+t}$. Although the domain of the growth region in the intermediate configuration is time-dependent, the representation of a given point that comes into existence at a time $\tau + t_g \in (\tau, \tau + t]$ in the growth domain $\overline{\mathcal{G}}^{\tau+t}$ does not depend on time after $\tau + t_g$ since the point occupies this region only in its original state. Pulling back to the time-independent regions of $\tilde{\mathcal{R}}^{\tau+t} \sqcup \overline{\mathcal{G}}^{\tau+t}$ thus allows interchanging time differentiation and volume integration in Equation (2.13). By the localization theorem,

$$\frac{d\rho}{dt} + \rho \, \mathrm{div}\mathbf{v} \;=\; 0 \,. \tag{2.14}$$

It is assumed that Equation (2.14) holds for each material point existing in the interior of $\mathcal{R}^{\tau+t}$ since mass is conserved in this region. Linear momentum balance is stated as

$$\frac{d}{dt} \int_{\mathcal{P}} \rho \mathbf{v} \, dv = \int_{\mathcal{P}} \rho \boldsymbol{b} \, dv + \int_{\partial \mathcal{P}} \boldsymbol{t} \, da \,. \tag{2.15}$$

Upon enforcing mass balance as stated in Equation (2.14), the relation between the traction and Cauchy stress $\boldsymbol{T}\boldsymbol{n} = \boldsymbol{t}$, and divergence theorem, the balance of linear momentum is

$$\int_{\mathcal{P}} \rho \frac{d\mathbf{v}}{dt} \, dv = \int_{\mathcal{P}} \rho \boldsymbol{b} \, dv + \int_{\mathcal{P}} \mathrm{div}\boldsymbol{T} \, dv \,. \tag{2.16}$$

where $\boldsymbol{b}$ is the body force per unit mass and $\boldsymbol{T}$ is the Cauchy stress tensor. Interchanging differentiation and integration in Equation (2.16) uses the same assumptions as was done in Equation (2.13). Using Equation (2.16), the point wise form of linear momentum is

$$\rho \frac{d\mathbf{v}}{dt} = \rho \boldsymbol{b} + \text{div}\boldsymbol{T} \ . \tag{2.17}$$

Angular momentum is stated as

$$\frac{d}{dt} \int_{\mathcal{P}} \mathbf{x} \times \rho \mathbf{v} \, dv = \int_{\mathcal{P}} \mathbf{x} \times \rho \boldsymbol{b} \, dv + \int_{\partial \mathcal{P}} \mathbf{x} \times \boldsymbol{t} \, da \ . \tag{2.18}$$

Invoking mass balance and the relation between the traction and Cauchy stress, it follows that

$$\int_{\mathcal{P}} \rho \left(\mathbf{x} \times \frac{d\mathbf{v}}{dt} \right) dv = \int_{\mathcal{P}} \mathbf{x} \times \rho \boldsymbol{b} \, dv + \int_{\mathcal{P}} \left(\boldsymbol{e}[\boldsymbol{T}^T] + \mathbf{x} \times \text{div}\boldsymbol{T} \right) dv \, , \tag{2.19}$$

where $\boldsymbol{e}[\boldsymbol{T}^T]$ is the permutation tensor acting on the transpose of the Cauchy tensor. Inserting the results of Equation (2.19) into Equation (2.18) and invoking linear momentum balance leads to the standard result that imposing

$$\boldsymbol{T} = \boldsymbol{T}^T \tag{2.20}$$

automatically satisfies angular momentum.

Mechanical energy balance is derived via the theorem of expended work, which is stated for some region $\mathcal{P} \subset \mathcal{R}^{\tau+t}$ as

$$\frac{d}{dt} \int_{\mathcal{P}} \frac{1}{2} \rho \mathbf{v} \cdot \mathbf{v} \, dv + \int_{\mathcal{P}} \boldsymbol{T} \cdot \boldsymbol{D} \, dv = \int_{\partial \mathcal{P}} \boldsymbol{t} \cdot \mathbf{v} \, da + \int_{\mathcal{P}} \rho \boldsymbol{b} \cdot \mathbf{v} \, dv \, , \tag{2.21}$$

where $\boldsymbol{D}$ is the symmetric part of the spatial velocity gradient $d\mathbf{v}/d\mathbf{x}$. The above follows directly from the balances of mass, and linear/angular momentum.

Total energy balance is stated as

$$\frac{d}{dt} \int_{\mathcal{P}} \left(\rho \epsilon + \frac{1}{2} \rho \mathbf{v} \cdot \mathbf{v} \right) dv = \int_{\partial \mathcal{P}} \left(\boldsymbol{t} \cdot \mathbf{v} + h \right) da + \int_{\mathcal{P}} \left(\rho \boldsymbol{b} \cdot \mathbf{v} + \rho r \right) dv \ . \tag{2.22}$$

Considering adiabatic processes (no heat flux/source, *i.e.*, $h = r = 0$), and utilizing the theorem of expended work and mass balance,

$$\int_{\mathcal{P}} \boldsymbol{T} \cdot \boldsymbol{D} \, dv = \int_{\mathcal{P}} \rho \frac{d\epsilon}{dt} \, dv \, , \tag{2.23}$$

thus leading to the point wise relation

$$\boldsymbol{T} \cdot \boldsymbol{D} = \rho \frac{d\epsilon}{dt} \ . \tag{2.24}$$

In summary, the initial/boundary-value problem is formally stated as follows:

Find the mass density $\rho : \mathcal{R}^{\tau+t} \times \mathcal{I} \mapsto \mathbb{R}^+$ *and material velocity* $\mathbf{v} : \mathcal{R}^{\tau+t} \times \mathcal{I} \mapsto \mathcal{E}^3$ *in the time interval* $\mathcal{I} = (\tau, \tau + t]$ *that satisfy Equations* (2.14) *and* (2.17) *in* $\mathcal{R}^{\tau+t} \times \mathcal{I}$*, subject to the initial conditions*

$$\begin{cases} \rho &= \rho_0(\mathbf{x}), \quad \text{in } \mathcal{R}^\tau \\ \mathbf{v} &= \mathbf{v}_0(\mathbf{x}), \quad \text{in } \mathcal{R}^\tau \end{cases}, \tag{2.25}$$

the boundary conditions

$$\begin{cases} \mathbf{v} &= \bar{\mathbf{v}}(\mathbf{x}, t), \quad \text{on } \Gamma_{v_i}^{\tau+t} \times \mathcal{I} \\ \boldsymbol{t} &= \bar{\boldsymbol{t}}(\mathbf{x}, t), \quad \text{on } \Gamma_{q_i}^{\tau+t} \times \mathcal{I} \end{cases}, \tag{2.26}$$

the prescribed surface motion of the intermediate configuration

$$\mathbf{v}_g = \bar{\mathbf{v}}_g(\mathbf{x}, t), \quad \text{on } \partial\tilde{\mathcal{R}}_g^{\tau+t} \times \mathcal{I}\,, \tag{2.27}$$

the growth/resorption extensions

$$\begin{cases} \rho &= \hat{\rho}(\mathbf{x}, t), \quad \text{on } \partial\tilde{\mathcal{R}}_g^{\tau+t} \times \mathcal{I} \\ \mathbf{v} &= \hat{\mathbf{v}}(\mathbf{x}, t), \quad \text{on } \partial\tilde{\mathcal{R}}_g^{\tau+t} \times \mathcal{I} \end{cases}, \tag{2.28}$$

and a constitutive law that obeys Equations (2.20) *and* (2.24).

In Equation (2.26), the i^{th} component of the surface with prescribed Neumann and Dirichlet boundary conditions are denoted Γ_{q_i} and Γ_{v_i}, respectively. These subdomains satisfy the traditional requirements

$$\begin{cases} \partial\mathcal{R}^{\tau+t} &= \overline{\Gamma_v^{\tau+t} \cup \Gamma_q^{\tau+t}} \\ \Gamma_q^{\tau+t} &= \bigcup_{i=1}^{3} \Gamma_{q_i}^{\tau+t}; \quad \Gamma_v^{\tau+t} = \bigcup_{i=1}^{3} \Gamma_{v_i}^{\tau+t} \\ \Gamma_{q_i}^{\tau+t} \cap \Gamma_{v_i}^{\tau+t} &= \emptyset \end{cases}. \tag{2.29}$$

The surface growth/resorption velocity in Equation (2.27) defines the motion of a non-material interface existing between the body and its external environment as material enters or exits the physical domain. In contrast, the conventional Neumann and Dirichlet boundary conditions on Γ_q and Γ_v, though also defined on the surface, uniquely determine the way in which the body deforms rather than defining the material which constitutes the body. Although surface growth/resorption and conventional Neumann/Dirichlet boundary conditions each define their own distinct characteristics of the initial/boundary-value problem, they are not necessarily mutually exclusive. For instance, when Neumann/Dirichlet boundary conditions are prescribed on a growing/resorpting surface, the fields defined for the set of material points constituting Γ_q and/or Γ_v are constrained to satisfy the corresponding boundary values at the instant they accrete to or resorpt from the surface. Since Γ_q and Γ_v are prescribed on a non-material interface, it is assumed that the portion of the surface constituting Neumann/Dirichlet boundary conditions is prescribed within the entire time interval $\mathcal{I}$.

The surface growth or resorption velocity in Equation (2.27) can either be imposed or solved

through a separate set of balance laws. The latter case may be pertinent when it is important to quantify the surface growth/resorption velocity in terms of the evolution of certain physical phenomena occurring directly on the interface such as a phase change or polymerization reaction. In this case, the normal growth/resorption velocity can be defined in terms of a surface-bound scalar variable φ representing a field such as the concentration of a given molecule. The balance law of the variable φ is posed for a subset of the closed surface defining the intermediate configuration boundary $\tilde{\Gamma} \subset \partial\tilde{\mathcal{R}}^{\tau+t}$ as

$$\frac{d_{\tilde{\Gamma}}}{dt}\int_{\tilde{\Gamma}} \varphi \, d\gamma \;=\; \int_{\partial\tilde{\Gamma}} \left(\varphi \mathbf{v}_g \cdot \boldsymbol{\nu}_{\tilde{\Gamma}} - \tilde{\boldsymbol{q}} \cdot \boldsymbol{\nu}_{\tilde{\Gamma}}\right) ds + \int_{\tilde{\Gamma}} f(\varphi)\, d\gamma \quad , \tag{2.30}$$

where $\boldsymbol{\nu}_{\tilde{\Gamma}}$ defines the tangent on the boundary of the curve $\tilde{\Gamma}$, $\tilde{\boldsymbol{q}}$ is the non-convective flux of the primary variable φ, and $f(\varphi)$ quantifies the reaction and source terms. Additionally, $d_{\tilde{\Gamma}}/dt$ denotes the time derivative with respect to points on the non-material surface $\tilde{\Gamma}$. It is assumed that the growth velocity is normal to the curve $\tilde{\Gamma}$ (*i.e.*, no tangential surface growth velocity), and hence, the first term on the right-hand side of Equation (2.30) vanishes, leading to

$$\frac{d_{\tilde{\Gamma}}}{dt}\int_{\tilde{\Gamma}} \varphi \, d\gamma \;=\; \int_{\partial\tilde{\Gamma}} -\tilde{\boldsymbol{q}} \cdot \boldsymbol{\nu}_{\tilde{\Gamma}}\, ds + \int_{\tilde{\Gamma}} f(\varphi)\, d\gamma \quad , \tag{2.31}$$

Applying Reynolds' transport theorem on a surface [28, Chapter 3], [29, 30, 31], the left-hand side in Equation (2.31) simplifies to

$$\frac{d_{\tilde{\Gamma}}}{dt}\int_{\tilde{\Gamma}} \varphi \, d\gamma \;=\; \int_{\tilde{\Gamma}} \left(\frac{d_{\tilde{\Gamma}}\varphi}{dt} - \mathbf{v}_{\tilde{\Gamma}} \cdot \mathrm{grad}_{\tilde{\Gamma}}\varphi - 2H\varphi(\mathbf{v} + \mathbf{v}_g) \cdot \tilde{\boldsymbol{n}} \right) d\gamma + \int_{\partial\tilde{\Gamma}} \varphi \mathbf{v}_{\tilde{\Gamma}} \cdot \boldsymbol{\nu}_{\tilde{\Gamma}}\, ds \quad . \tag{2.32}$$

Here, H is the mean curvature and $\tilde{\boldsymbol{n}}$ is the outward-facing unit normal vector on the curve $\tilde{\Gamma}$. The last term in Equation (2.32) represents the convection of the variable φ across the boundary, which is assumed to exist when $\partial\tilde{\Gamma} \neq \emptyset$ and the tangential component of the material velocity $\mathbf{v}_{\tilde{\Gamma}} \neq \mathbf{0}$.

Assuming $\tilde{\boldsymbol{q}} = -K\mathrm{grad}_{\tilde{\Gamma}}\varphi$ where K is a constant positive diffusion coefficient, Equation (2.30) is further simplified via the surface divergence theorem [28, Chapter 3], [32] under the assumption of normal surface growth, and is thus expressed as

$$\int_{\tilde{\Gamma}} \left(\frac{d_{\tilde{\Gamma}}\varphi}{dt} + \varphi \,\mathrm{div}_{\tilde{\Gamma}}\mathbf{v}_{\tilde{\Gamma}} - 2H\varphi\,(\mathbf{v} + \mathbf{v}_g) \cdot \tilde{\boldsymbol{n}} \right) d\gamma \;=\; \int_{\tilde{\Gamma}} \left(\mathrm{div}_{\tilde{\Gamma}}\left[K\mathrm{grad}_{\tilde{\Gamma}}\varphi\right] + f(\varphi) \right) d\gamma \quad . \tag{2.33}$$

Upon using the localization theorem, the strong form of Equation (2.33) becomes

$$\frac{d_{\tilde{\Gamma}}\varphi}{dt} + \varphi \,\mathrm{div}_{\tilde{\Gamma}}\mathbf{v}_{\tilde{\Gamma}} - 2H\varphi(\mathbf{v} + \mathbf{v}_g) \cdot \tilde{\boldsymbol{n}} \;=\; \mathrm{div}_{\tilde{\Gamma}}\left[K\mathrm{grad}_{\tilde{\Gamma}}\varphi\right] + f(\varphi) \quad . \tag{2.34}$$

The normal growth/resorption velocity is assumed to hold the generic functional form $\mathrm{v}_{gn} = \mathbf{v}_g \cdot \tilde{\boldsymbol{n}} = \hat{\mathrm{v}}_{gn}(\varphi, \dot{\varphi})$. Supposing that $\partial\tilde{\mathcal{R}}^{\tau+t}$ is a closed surface, the initial-value problem for the surface-bound variable φ is stated below:

Find $\varphi : \partial\tilde{\mathcal{R}}^{\tau+t} \times \mathcal{I} \mapsto \mathbb{R}^+$ *in the time interval* $\mathcal{I} = (\tau, \tau + t]$ *that satisfies Equation* (2.34) *on* $\partial\tilde{\mathcal{R}}^{\tau+t} \times \mathcal{I}$*, subject to the initial conditions:*

$$\varphi = \varphi_0(\mathbf{x}), \quad \text{on } \partial\tilde{\mathcal{R}}^{\tau} \quad . \tag{2.35}$$

2.4 Concluding Remarks

In this chapter, the kinematics of surface growth was introduced. The complete description of motion for a body consists of a surface growth/resorption transformation $\boldsymbol{\chi}_g$ mapping the boundary of a reference domain $\partial\mathcal{R}^{\tau}$ to an intermediate configuration $\partial\tilde{\mathcal{R}}^{\tau+t}$ which encloses a new volume containing the material points and fields existing at time $\tau + t$, a homeomorphism $\overline{\boldsymbol{\chi}}_g$ mapping grown particles from their positions at the instant they come into existence onto the growth region of the intermediate configuration $\mathcal{G}^{\tau+t}$, and lastly, a deformation motion $\boldsymbol{\chi}_d$ mapping all material points existing at the current time $\tau + t$ in the intermediate configuration to the current configuration $\mathcal{R}^{\tau+t}$. The deformation gradient mapping a material tangent vector from its initial configuration onto the current configuration was defined based on the material gradient of the total motion at a given point, which includes both $\boldsymbol{\chi}_d$ and $\overline{\boldsymbol{\chi}}_g$ for accreted regions.

Using the kinematics describing growth, the global balance of mass, linear momentum, angular momentum, and total energy were posed for a growing/resorpting body. Additionally, a global balance law was derived for a surface-bound scalar variable φ, such that the surface growth/resorption velocity can be defined through the evolution of a surface variable, $\mathbf{v}_g = \hat{\mathbf{v}}_g(\varphi, \dot{\varphi})$. The set of point wise balance laws were posed using the localization theorem, and the formal initial/boundary-value problem was stated for a deformable body undergoing surface growth/resorption. In the next chapter, an algorithmic implementation based on the Arbitrary Lagrangian-Eulerian finite element method will be introduced to numerically solve the set of discretized balance laws for a two-dimensional body.

Chapter 3

Finite Element Approximation

3.1 Overview

This chapter focuses on the numerical solution strategy to solve the balance laws presented in Chapter 2. The weak forms of the balance laws are derived in Section 3.2 using a weighted residual formulation. The spatially and temporally discretized weighted residuals are presented in Section 3.3. The meshing algorithm is briefly described in Section 3.4. Lastly, two examples are presented in Section 3.5: The first consisting of an elliptical cylinder undergoing surface growth and resorption without any imposed loads or deformations, and the second consisting of a hollow elliptical cylinder with an internal applied pressure and surface growth/resorption on its outer surface. These examples illustrate the consistency for a set of trivial model problems, and highlight the numerical and physical characteristics of a deforming body undergoing discrete surface growth/resorption at different length and time scales.

3.2 Weak Forms

In this section, the weak forms of the governing balance laws are presented in two spatial dimensions. Consider the spaces of weight functions σ and densities ρ defined as follows:

$$\begin{aligned} \mathcal{S} &= \left\{ \sigma \in H^0(\mathcal{R}^{\tau+t}) \right\}, \\ \mathcal{P} &= \left\{ \rho \in H^0(\mathcal{R}^{\tau+t}) \mid \rho > 0,\ \rho(\mathbf{x},\tau) = \rho_0(\mathbf{x}) \right\}, \end{aligned} \tag{3.1}$$

where $H^m(\mathcal{R}^{\tau+t})$ is the Sobolev space of order m in the space variables for all scalar functions defined in $\mathcal{R}^{\tau+t}$. The weighted residual form of mass balance is stated as

$$R_\rho = \int_{\mathcal{R}^{\tau+t}} \sigma \left(\frac{d\rho}{dt} + \rho \, \mathrm{div}\mathbf{v} \right) dv = 0 \,. \tag{3.2}$$

The space of weight functions $\boldsymbol{\xi}$ and velocities $\mathbf{v}$ are defined as

$$\begin{aligned}\mathcal{X} &= \left\{\boldsymbol{\xi} \in \boldsymbol{H}^1(\mathcal{R}^{\tau+t}) \mid \xi_i = 0 \text{ on } \Gamma_{v_i}^{\tau+t},\ i = 1,2\right\},\\ \mathcal{V} &= \left\{\mathbf{v} \in \boldsymbol{H}^1(\mathcal{R}^{\tau+t}) \mid \mathbf{v}(\mathbf{x},\tau) = \mathbf{v}_0(\mathbf{x}),\ \mathrm{v}_i = \bar{\mathrm{v}}_i(\mathbf{x},t) \text{ on } \Gamma_{v_i}^{\tau+t},\ i = 1,2\right\},\end{aligned} \tag{3.3}$$

where $\boldsymbol{H}^m(\mathcal{R}^{\tau+t})$ defines the Sobolev space of order m for the space variables of all two-dimensional vector functions defined in $\mathcal{R}^{\tau+t}$. The weighted residual for the balance of linear momentum is

$$R_v = \int_{\mathcal{R}^{\tau+t}} \boldsymbol{\xi} \cdot \left(\rho\frac{d\mathbf{v}}{dt} - \rho\boldsymbol{b} - \mathrm{div}\boldsymbol{T}\right) dv + \sum_{i=1}^{2}\int_{\Gamma_{q_i}^{\tau+t}} \xi_i(t_i - \bar{t}_i)\, da = 0\,. \tag{3.4}$$

Upon employing the product rule and divergence theorem, the reduced weighted residual for the balance of linear momentum becomes

$$\int_{\mathcal{R}^{\tau+t}} \left(\boldsymbol{\xi} \cdot \rho\dot{\mathbf{v}} + \frac{\partial^s \boldsymbol{\xi}}{\partial \mathbf{x}} \cdot \boldsymbol{T}\right) dv = \int_{\mathcal{R}^{\tau+t}} \rho\boldsymbol{b}\, dv + \sum_{i=1}^{2}\int_{\Gamma_{q_i}^{\tau+t}} \xi_i \bar{t}_i\, da\,. \tag{3.5}$$

Lastly, considering the space of surface-bound weight functions ω and variable φ, define

$$\begin{aligned}\mathcal{W} &= \left\{\omega \in H^1(\partial\tilde{\mathcal{R}}^{\tau+t})\right\},\\ \mathcal{O} &= \left\{\varphi \in H^1(\partial\tilde{\mathcal{R}}^{\tau+t}) \mid \varphi > 0,\ \varphi(\mathbf{x},\tau) = \varphi_0(\mathbf{x})\right\}.\end{aligned} \tag{3.6}$$

Upon using the divergence theorem on the surface, the weighted residual for the surface balance law in Equation (2.34) takes the form

$$\int_{\partial\tilde{\mathcal{R}}^{\tau+t}} \left(\omega\frac{d_{\tilde{\Gamma}}\varphi}{dt} + \omega\varphi\,\mathrm{div}_{\tilde{\Gamma}}\mathbf{v}_{\tilde{\Gamma}} - 2H\,\omega\varphi(\mathbf{v}+\mathbf{v}_g)\cdot\boldsymbol{n}\right) da = \int_{\partial\tilde{\mathcal{R}}^{\tau+t}} \left(-\mathrm{grad}_{\tilde{\Gamma}}\omega \cdot K\mathrm{grad}_{\tilde{\Gamma}}\varphi + \omega f(\varphi)\right) da\,. \tag{3.7}$$

The full statement of weak form of the initial/boundary-value problem is as follows:

Given the data $\bar{\boldsymbol{t}}, \boldsymbol{b}$, a constitutive law satisfying Equations (2.20) *and* (2.24)*, a growth law for $\mathbf{v}_g$, and prescribed growth/resorption extensions of the velocity and density on $\partial\tilde{\mathcal{R}}_g^{\tau+t} \times \mathcal{I}$, find the mass density $\rho \in \mathcal{P}$, material velocity $\mathbf{v} \in \mathcal{V}$, and $\varphi \in \mathcal{O}$, such that Equations* (3.2)*,* (3.5) *and* (3.7) *are satisfied for any $\sigma \in \mathcal{S}$, $\boldsymbol{\xi} \in \mathcal{X}$, and $\omega \in \mathcal{W}$.*

3.3 Discretization

3.3.1 Spatial Discretization of the Balance Laws

Define a spatially discretized domain Ω and its boundary $\partial\Omega$ occupying the two-dimensional and one-dimensional Euclidean space (respectively) as

$$\begin{aligned} \Omega &= \overline{\bigcup_{e=1}^{\texttt{nel}} \Omega^e}, \\ \partial\Omega &\subseteq \overline{\bigcup_{e=1}^{\texttt{nsurf\_el}} \partial\Omega^e}, \end{aligned} \tag{3.8}$$

and its corresponding representation in the intermediate configuration,

$$\begin{aligned} \tilde{\Omega} &= \overline{\bigcup_{e=1}^{\texttt{nel}} \tilde{\Omega}^e}, \\ \partial\tilde{\Omega} &\subseteq \overline{\bigcup_{e=1}^{\texttt{nsurf\_el}} \partial\tilde{\Omega}^e}, \end{aligned} \tag{3.9}$$

where an attached superscript e denotes a single element subdomain, and `nel` and `nsurf_el` are the total number of interior and boundary elements, respectively.

Considering the classical Bubnov-Galerkin semi-discretization approach, the interpolated variables for a given finite element Ω^e are defined as

$$\begin{aligned} \rho_h^e(\mathbf{x},t) &= \sum_{i=1}^{\texttt{nem}} \bar{N}_i^e(\mathbf{x})\rho_i^e(t) = \bar{\boldsymbol{N}}^e\hat{\boldsymbol{\rho}}^e; \quad \sigma_h^e(\mathbf{x}) = \sum_{i=1}^{\texttt{nem}} \bar{N}_i^e(\mathbf{x})\sigma_i^e = \bar{\boldsymbol{N}}^e\hat{\boldsymbol{\sigma}}^e, \\ \mathbf{v}_h^e(\mathbf{x},t) &= \sum_{i=1}^{\texttt{nen}} N_i^e(\mathbf{x})\mathbf{v}_i^e(t) = \boldsymbol{N}^e\hat{\mathbf{v}}^e; \quad \boldsymbol{\xi}_h^e(\mathbf{x}) = \sum_{i=1}^{\texttt{nen}} N_i^e(\mathbf{x})\boldsymbol{\xi}_i^e = \boldsymbol{N}^e\hat{\boldsymbol{\xi}}^e, \\ \varphi_h^e(\mathbf{x}^\Gamma,t) &= \sum_{i=1}^{\texttt{nsn}} \bar{\bar{N}}_i^e(\mathbf{x}^\Gamma)\varphi_i^e(t) = \bar{\bar{\boldsymbol{N}}}^e\hat{\boldsymbol{\varphi}}^e; \quad \omega_h^e(\mathbf{x}^\Gamma) = \sum_{i=1}^{\texttt{nsn}} \bar{\bar{N}}_i^e(\mathbf{x}^\Gamma)\omega_i^e = \bar{\bar{\boldsymbol{N}}}^e\hat{\boldsymbol{\omega}}^e, \end{aligned} \tag{3.10}$$

where `nen`, `nem`, and `nsn` are the number of element nodes, density degrees of freedom per element, and boundary element nodes, respectively. Moreover, $\hat{\boldsymbol{\rho}}^e$, $\hat{\boldsymbol{\sigma}}^e$, $\hat{\mathbf{v}}^e$, $\hat{\boldsymbol{\xi}}^e$, $\hat{\boldsymbol{\varphi}}$, and $\hat{\boldsymbol{\omega}}$ are the nodal values ordered in vector form. The element interpolation matrices are defined as follows

$$
\begin{aligned}
\bar{\boldsymbol{N}}^e &= \begin{bmatrix} \bar{N}_1^e & \bar{N}_2^e & \dots & \bar{N}_{\mathtt{nem}}^e \end{bmatrix} , \\
\boldsymbol{N}^e &= \begin{bmatrix} N_1^e & 0 & N_2^e & 0 & \dots & N_{\mathtt{nen}}^e & 0 \\ 0 & N_1^e & 0 & N_1^e & \dots & 0 & N_{\mathtt{nen}}^e \end{bmatrix} , \\
\bar{\bar{\boldsymbol{N}}}^e &= \begin{bmatrix} \bar{\bar{N}}_1^e & \bar{\bar{N}}_2^e & \dots & \bar{\bar{N}}_{\mathtt{nsn}}^e \end{bmatrix} .
\end{aligned}
\tag{3.11}
$$

The spaces of admissible functions are

$$
\begin{aligned}
\mathcal{P}_h &= \left\{ \rho_h \in H^0(\Omega^e) \mid \rho_h(\mathbf{x},\tau) = \rho_0(\mathbf{x}),\ \rho_h(\mathbf{x},t) > 0 \right\} , \\
\mathcal{S}_h &= \left\{ \sigma_h \in H^0(\Omega^e) \right\} , \\
\mathcal{V}_h &= \left\{ \mathbf{v}_h \in \boldsymbol{H}^1(\Omega^e) \mid \mathbf{v}_h(\mathbf{x},\tau) = \mathbf{v}_0(\mathbf{x}),\ \mathrm{v}_i(\mathbf{x},t) = \bar{\mathrm{v}}_i(\mathbf{x},t) \text{ on } \Gamma_{v_i}^{\tau+t},\ i = 1,2 \right\} , \\
\mathcal{X}_h &= \left\{ \boldsymbol{\xi}_h \in \boldsymbol{H}^1(\Omega^e) \mid \xi_i(\mathbf{x},t) = 0 \text{ on } \Gamma_{v_i}^{\tau+t},\ i = 1,2 \right\} , \\
\mathcal{O}_h &= \left\{ \varphi_h \in H^1(\partial\tilde{\Omega}^e) \right\} , \\
\mathcal{W}_h &= \left\{ \omega_h \in H^1(\partial\tilde{\Omega}^e) \right\} .
\end{aligned}
\tag{3.12}
$$

Using the interpolated variables, the weak balance of mass is

$$
\bar{\boldsymbol{M}}^e \overset{\square}{\boldsymbol{\rho}}^e + \bar{\boldsymbol{F}}^e \hat{\boldsymbol{\rho}}^e = \mathbf{0} ,
\tag{3.13}
$$

where $\overset{\square}{\boldsymbol{\rho}}^e$ is the discretized material time derivative of the density in vector form, *i.e.*,

$$
\overset{\square}{\boldsymbol{\rho}}^e = \frac{\hat{\boldsymbol{\rho}}_{n+1}^e - \hat{\bar{\boldsymbol{\rho}}}_n^e}{\Delta t_{n+1}} .
\tag{3.14}
$$

Here, the subscripts n or $n+1$ attached to a given variable indicates that it is evaluated at t_n or t_{n+1} (respectively), and $\Delta t_{n+1} = t_{n+1} - t_n$ is the time increment. Additionally, $\bar{\boldsymbol{M}}$ and $\bar{\boldsymbol{F}}$ are defined as

$$
\begin{aligned}
\bar{\boldsymbol{M}}^e &= \int_{\Omega^e} (\bar{\boldsymbol{N}}^e)^T \bar{\boldsymbol{N}}^e \, dv , \\
\bar{\boldsymbol{F}}^e &= \int_{\Omega^e} (\bar{\boldsymbol{N}}^e)^T \bar{\boldsymbol{N}}^e (\boldsymbol{\Delta}^e \hat{\mathbf{v}}^e) \, dv .
\end{aligned}
\tag{3.15}
$$

Here, $\boldsymbol{\Delta}^e$ is the divergence operator acting on $\boldsymbol{N}^e$ defined as

$$
\boldsymbol{\Delta}^e = \begin{bmatrix} \frac{d\bar{N}_1^e}{d\mathrm{x}_1} & \frac{d\bar{N}_1^e}{d\mathrm{x}_2} & \dots & \frac{d\bar{N}_{\mathtt{nen}}^e}{d\mathrm{x}_1} & \frac{d\bar{N}_{\mathtt{nen}}^e}{d\mathrm{x}_2} \end{bmatrix} .
\tag{3.16}
$$

The discretized weak form of the balance of linear momentum is

$$\boldsymbol{M}^e \overset{\square}{\mathbf{v}}^e + \boldsymbol{F}^e_{int} - \boldsymbol{F}^e_{ext} \;=\; \mathbf{0}\,, \tag{3.17}$$

where $\boldsymbol{M}^e$, $\boldsymbol{F}^e_{int}$ and $\boldsymbol{F}^e_{ext}$ are defined as

$$\begin{aligned}
\boldsymbol{M}^e &= \int_{\Omega^e} (\boldsymbol{N}^e)^T (\bar{\boldsymbol{N}}^e \hat{\boldsymbol{\rho}}^e) \boldsymbol{N}^e \, dv\,, \\
\boldsymbol{F}^e_{int} &= \int_{\Omega^e} (\boldsymbol{B}^e)^T \hat{\boldsymbol{T}}^e \, dv\,, \\
\boldsymbol{F}^e_{ext} &= \int_{\Omega^e} (\boldsymbol{N}^e)^T (\bar{\boldsymbol{N}}^e \hat{\boldsymbol{\rho}}^e) \boldsymbol{b} \, dv + \int_{\partial\Omega^e \cap \Gamma_q^{\tau+t}} (\boldsymbol{N}^e)^T \bar{\boldsymbol{t}} \, da + \int_{\partial\Omega^e \setminus \Gamma_q^{\tau+t}} (\boldsymbol{N}^e)^T \boldsymbol{t} \, da\,,
\end{aligned} \tag{3.18}$$

and $\overset{\square}{\mathbf{v}}^e$ is the discretized material time derivative of the velocity (equivalent to the material acceleration), which is expressed as

$$\overset{\square}{\mathbf{v}}^e = \frac{\hat{\mathbf{v}}^e_{n+1} - \hat{\mathbf{v}}^e_n}{\Delta t_{n+1}}\,. \tag{3.19}$$

Additionally, $\hat{\boldsymbol{T}}$ is the Cauchy stress in vector form, and $\boldsymbol{B}^e$ is a gradient operator acting on $\boldsymbol{N}^e$ defined as

$$\boldsymbol{B}^e \;=\; \begin{bmatrix} \frac{dN^e_1}{d\mathrm{x}_1} & 0 & \dots & \frac{dN^e_{\mathrm{nen}}}{d\mathrm{x}_1} & 0 \\ 0 & \frac{dN^e_1}{d\mathrm{x}_2} & \dots & 0 & \frac{dN^e_{\mathrm{nen}}}{d\mathrm{x}_2} \\ \frac{dN^e_1}{d\mathrm{x}_2} & \frac{dN^e_1}{d\mathrm{x}_1} & \dots & \frac{dN^e_{\mathrm{nen}}}{d\mathrm{x}_2} & \frac{dN^e_{\mathrm{nen}}}{d\mathrm{x}_1} \end{bmatrix}\,. \tag{3.20}$$

The discretized surface balance is expressed as

$$\bar{\bar{\boldsymbol{M}}}^e \overset{\square}{\boldsymbol{\varphi}}^e + \bar{\bar{\boldsymbol{L}}}^e \hat{\boldsymbol{\varphi}}^e + \bar{\bar{\boldsymbol{K}}}^e \hat{\boldsymbol{\varphi}}^e - \bar{\bar{\boldsymbol{F}}}^e \;=\; \mathbf{0}\quad. \tag{3.21}$$

In Equation (3.21), $\overset{\square}{\boldsymbol{\varphi}}^e$ is the discretized time derivative of the concentration with respect to fixed coordinates of the boundary $\partial\tilde{\Omega}$, which is expressed as

$$\overset{\square}{\boldsymbol{\varphi}}^e = \frac{\hat{\boldsymbol{\varphi}}^e_{n+1} - \hat{\boldsymbol{\varphi}}^e_n}{\Delta t_{n+1}}\,. \tag{3.22}$$

The surface arrays are defined as

$$\begin{aligned}
\bar{\bar{\boldsymbol{M}}}^e &= \int_{\partial\tilde{\Omega}^e} (\bar{\bar{\boldsymbol{N}}}^e)^T \bar{\bar{\boldsymbol{N}}}^e \, d\gamma \,, \\
\bar{\bar{\boldsymbol{L}}}^e &= \int_{\partial\tilde{\Omega}^e} (\bar{\bar{\boldsymbol{N}}}^e)^T \bar{\bar{\boldsymbol{N}}}^e \left(\bar{\bar{\boldsymbol{\Delta}}}^e \hat{\mathbf{v}}^e - 2H(\hat{\mathrm{v}}_n^e + \mathrm{v}_{gn}) \right) d\gamma \,, \\
\bar{\bar{\boldsymbol{K}}}^e &= \int_{\partial\tilde{\Omega}^e} K(\bar{\bar{\boldsymbol{B}}}^e)^T \bar{\bar{\boldsymbol{B}}}^e \, d\gamma \,, \\
\bar{\bar{\boldsymbol{F}}}^e &= \int_{\partial\tilde{\Omega}^e} (\bar{\bar{\boldsymbol{N}}}^e)^T \hat{\boldsymbol{f}}^e \, d\gamma \,.
\end{aligned} \tag{3.23}$$

In Equation (3.23), $\hat{\mathrm{v}}_n^e$ and v_{gn} are the normal components of the material and growth/resorption velocity, respectively. The discrete element divergence and gradient operators $\bar{\bar{\boldsymbol{\Delta}}}^e$ and $\bar{\bar{\boldsymbol{B}}}^e$ (respectively) are equivalent for a one-dimensional curve embedded in a two-dimensional Euclidean space, and are defined as

$$\bar{\bar{\boldsymbol{\Delta}}}^e = \bar{\bar{\boldsymbol{B}}}^e = \begin{bmatrix} \frac{d\bar{\bar{N}}_1^e}{d\mathrm{x}^\Gamma} & \frac{d\bar{\bar{N}}_2^e}{d\mathrm{x}^\Gamma} & \cdots & \frac{d\bar{\bar{N}}_{\mathtt{nsn}}^e}{d\mathrm{x}^\Gamma} \end{bmatrix} . \tag{3.24}$$

The mean curvature H in Equation (3.23) for a given node along the surface of a mesh is determined by computing the central difference of the neighboring tangent vectors,

$$H = \frac{1}{2} \frac{(\hat{\boldsymbol{t}}_R - \hat{\boldsymbol{t}}_L) \cdot \boldsymbol{n}}{l} \,, \tag{3.25}$$

where $\hat{\boldsymbol{t}}_R$ and $\hat{\boldsymbol{t}}_L$ are the tangent vectors of the right and left neighboring nodes (computed as the average tangent vectors of the surface elements adjacent to the right and left nodes), and l is the total length of the surface elements adjacent to the given node. It is assumed that the out-of-plane curvature is zero (*i.e.* the surface is flat in this direction), therefore the mean curvature is simply half of the in-plane curvature.

Considering the standard assumption that $\hat{\boldsymbol{\xi}}^e$, $\hat{\boldsymbol{\sigma}}^e$, and $\hat{\boldsymbol{\omega}}^e$ are arbitrary, Equations (3.13), (3.17) and (3.21) lead to a coupled nonlinear system of equations for the solution vectors $\hat{\boldsymbol{\rho}}^e$, $\hat{\mathbf{v}}^e$, and $\hat{\boldsymbol{\varphi}}^e$. The global solution of the fields $\hat{\boldsymbol{\rho}}$ and $\hat{\mathbf{v}}$ is obtained for the entire finite-element domain through an assembly of Equations (3.13) and (3.17) for each Ω^e. The global system of equations for the density is stated as

$$\bar{\boldsymbol{M}} \overset{\square}{\hat{\boldsymbol{\rho}}} + \bar{\boldsymbol{F}} \hat{\boldsymbol{\rho}} = \mathbf{0} \,, \tag{3.26}$$

where $\bar{\boldsymbol{M}}$ and $\bar{\boldsymbol{F}}$ are defined as

$$\begin{aligned}
\bar{\boldsymbol{M}} &= \mathop{\mathsf{A}}_{e=1}^{\mathtt{nel}} \int_{\Omega^e} (\bar{\boldsymbol{N}}^e)^T \bar{\boldsymbol{N}}^e \, dv \,, \\
\bar{\boldsymbol{F}} &= \mathop{\mathsf{A}}_{e=1}^{\mathtt{nel}} \int_{\Omega^e} (\bar{\boldsymbol{N}}^e)^T \bar{\boldsymbol{N}}^e \boldsymbol{\Delta}^e \mathbf{v}^e \, dv \,.
\end{aligned} \tag{3.27}$$

Global linear momentum balance is stated as

$$\boldsymbol{M}\,\overset{\square}{\mathbf{v}} - \hat{\boldsymbol{F}} \;=\; \mathbf{0}\,, \tag{3.28}$$

where $\boldsymbol{M}$ and $\hat{\boldsymbol{F}}$ are defined as

$$\begin{aligned}
\boldsymbol{M} &= \mathop{\mathtt{A}}_{e=1}^{\mathtt{nel}} \left[\int_{\Omega^e} (\boldsymbol{N}^e)^T (\bar{\boldsymbol{N}}^e \hat{\boldsymbol{\rho}}^e) \boldsymbol{N}^e \, dv \right], \\
\hat{\boldsymbol{F}} &= \mathop{\mathtt{A}}_{e=1}^{\mathtt{nel}} \left[\int_{\Omega^e} -(\boldsymbol{B}^e)^T \hat{\boldsymbol{T}}^e \, dv + \int_{\partial\Omega^e \cap \Gamma_q} (\boldsymbol{N}^e)^T \bar{\boldsymbol{t}} \, da + \int_{\Omega^e} (\boldsymbol{N}^e)^T (\bar{\boldsymbol{N}}^e \hat{\boldsymbol{\rho}}^e) \boldsymbol{b} \, dv \right].
\end{aligned} \tag{3.29}$$

The global vector of the surface-bound variable $\hat{\boldsymbol{\varphi}}$ is obtained for the entire surface of the finite-element domain through the assembly of Equation (3.21) for each individual surface $\partial\tilde{\Omega}^e$. The system of equations for the global balance of $\hat{\boldsymbol{\varphi}}$ is stated as

$$\bar{\bar{\boldsymbol{M}}} \overset{\square}{\hat{\boldsymbol{\varphi}}} + \bar{\bar{\boldsymbol{L}}} \hat{\boldsymbol{\varphi}} + \bar{\bar{\boldsymbol{K}}} \hat{\boldsymbol{\varphi}} - \bar{\bar{\boldsymbol{F}}} \;=\; \mathbf{0}\,, \tag{3.30}$$

where the assembled global matrices $\bar{\bar{\boldsymbol{M}}}$, $\bar{\bar{\boldsymbol{L}}}$, $\bar{\bar{\boldsymbol{K}}}$, and $\bar{\bar{\boldsymbol{F}}}$ are defined as

$$\begin{aligned}
\bar{\bar{\boldsymbol{M}}} &= \mathop{\mathtt{A}}_{e=1}^{\mathtt{nsurf_el}} \int_{\partial\tilde{\Omega}^e} (\bar{\bar{\boldsymbol{N}}}^e)^T \bar{\bar{\boldsymbol{N}}}^e \, d\gamma\,, \\
\bar{\bar{\boldsymbol{L}}} &= \mathop{\mathtt{A}}_{e=1}^{\mathtt{nsurf_el}} \int_{\partial\tilde{\Omega}^e} (\bar{\bar{\boldsymbol{N}}}^e)^T \bar{\bar{\boldsymbol{N}}}^e \left(\bar{\bar{\boldsymbol{\Delta}}}^e \hat{\mathbf{v}}^e - 2H(\hat{\mathrm{v}}^{en} + \mathrm{v}^{gn}) \right) d\gamma\,, \\
\bar{\bar{\boldsymbol{K}}} &= \mathop{\mathtt{A}}_{e=1}^{\mathtt{nsurf_el}} \int_{\partial\tilde{\Omega}^e} K(\bar{\bar{\boldsymbol{B}}}^e)^T \bar{\bar{\boldsymbol{B}}}^e \, d\gamma\,, \\
\bar{\bar{\boldsymbol{F}}} &= \mathop{\mathtt{A}}_{e=1}^{\mathtt{nsurf_el}} \int_{\partial\tilde{\Omega}^e} (\bar{\bar{\boldsymbol{N}}}^e)^T \hat{\boldsymbol{f}}^e(\hat{\boldsymbol{\varphi}}) \, d\gamma\,.
\end{aligned} \tag{3.31}$$

3.3.2 Temporal Discretization of the Balance Laws

The time discretization of Equations (3.26), (3.28) and (3.30) is highlighted below. For brevity, the reference time τ is omitted, and the current time is denoted as t_{n+1}. Additionally, the subscript $n+1$ attached to a variable or domain indicates that it is associated with the time t_{n+1}.

The density, velocity, and surface variable are coupled using a staggered solution algorithm. Considering a finite element mesh with N nodes in which S nodes lie on the surface, the staggered algorithm maintains global matrices that are $N \times N$, $2N \times 2N$, and $S \times S$ for balances of mass, linear momentum, and surface-bound variable, respectively. This avoids solving a global $(3N + S) \times (3N + S)$ system of equations that would be required using a monolithic solution strategy at the cost of performing multiple iterations to generate a global solution at t_{n+1}. However, the convergence and accuracy of the field variables using this solution methodology depends on the initial guess and time increment. In the results presented in this work, the time increment and

tolerance in the convergence of the fields are chosen to be sufficiently small to maintain stability of the staggered iterations. The algorithmic details of the staggering scheme used in this work is provided in Appendix A.1.

A staggered trapezoidal method is used to obtain the mass density based on Equation (3.13) for a given time t_{n+1}. With this solution strategy, the density at time t_{n+1} can be determined implicitly with the following system of equations:

$$\bar{\boldsymbol{M}}_{n+1}(\hat{\boldsymbol{\rho}}_{n+1} - \hat{\bar{\boldsymbol{\rho}}}_n) \;=\; -\frac{\Delta t_{n+1}}{2}\left(\bar{\boldsymbol{F}}_n\hat{\bar{\boldsymbol{\rho}}}_n + \bar{\boldsymbol{F}}_{n+1}\hat{\boldsymbol{\rho}}_{n+1}\right), \tag{3.32}$$

where $\hat{\bar{\boldsymbol{\rho}}}_n$ is the global vector of the density at time t_n in the intermediate configuration, and $\Delta t_{n+1} = t_{n+1} - t_n$ is the current time increment size. The arrays $\bar{\boldsymbol{M}}_{n+1}$ and $\bar{\boldsymbol{F}}_{n+1}$ correspond to their equivalent global matrices in Equation (3.27) evaluated at time t_{n+1}. Since the velocity and density at t_{n+1} are solved in a staggered manner, the velocities at t_{n+1} and t_n are known in Equation (3.27). Therefore, the density of the current staggered iteration is the only unknown in Equation (3.32).

The velocities at time t_{n+1} are obtained using the Newmark-β time integration scheme as introduced in [33], with $\gamma = 1/2$, corresponding to the trapezoidal method. This leads to a discretized system of equations which are generally nonlinear functions of the velocity at t_{n+1}. Therefore, the residual at the k^{th} iteration is defined as follows:

$$\hat{\boldsymbol{R}}(\mathbf{v}^k_{n+1}) = \boldsymbol{M}^k_{n+1}\left(\hat{\mathbf{v}}^k_{n+1} - \hat{\tilde{\mathbf{v}}}_n\right) - \frac{\Delta t_{n+1}}{2}\left(\hat{\boldsymbol{F}}^k_{n+1} + \hat{\bar{\boldsymbol{F}}}_n\right) \;=\; \mathbf{0}\,. \tag{3.33}$$

The solution for the velocities that satisfies Equation (3.33) is obtained iteratively using Newton's method which is defined for the k^{th} iteration as

$$\hat{\mathbf{v}}^{k+1}_{n+1} = \hat{\tilde{\mathbf{v}}}_n - \left[D\hat{\boldsymbol{R}}(\mathbf{v}^k_{n+1})\right]^{-1}\hat{\boldsymbol{R}}(\mathbf{v}^k_{n+1})\,, \tag{3.34}$$

where $D\hat{\boldsymbol{R}}(\hat{\mathbf{v}}^k_{n+1})$ is the tangent matrix evaluated at the current iterate of the material velocity $\hat{\mathbf{v}}^k_{n+1}$ and $\tilde{\mathbf{v}}_n$ is the material velocity at time t_n in the intermediate configuration. Since the velocity at t_{n+1} is obtained in a staggered manner, the current density at t_{n+1} is assumed to be known when computing the global matrices in Equation (3.29). Therefore, $\hat{\mathbf{v}}_{n+1}$ is the only unknown in Equation (3.33).

Once the solution vector of velocities $\hat{\mathbf{v}}_{n+1}$ is obtained, the accelerations and displacements are directly determined using the Newmark-β time integration scheme,

$$\begin{cases} \hat{\boldsymbol{a}}_{n+1} = \frac{2}{\Delta t_{n+1}}\left(\hat{\mathbf{v}}_{n+1} - \hat{\tilde{\mathbf{v}}}_n\right) - \hat{\tilde{\boldsymbol{a}}}_n \\ \hat{\boldsymbol{u}}_{n+1} = \hat{\tilde{\boldsymbol{u}}}_n + \Delta t_{n+1}\hat{\tilde{\mathbf{v}}}_n + \frac{1-2\beta}{2}\Delta t^2_{n+1}\hat{\tilde{\boldsymbol{a}}}_n + \beta\Delta t^2_{n+1}\hat{\boldsymbol{a}}_{n+1} \end{cases}. \tag{3.35}$$

The value of β is chosen as $1/4$, thus corresponding to the trapezoidal method for both displacements and velocities.

The material displacements at a given point can be formulated incrementally by additively separating the contribution from each time step as follows

$$
\begin{aligned}
\boldsymbol{u}_{n+1} &= \boldsymbol{u}_n + \Delta\boldsymbol{u}_{n+1} \\
&= \boldsymbol{u}_{n-1} + \Delta\boldsymbol{u}_n + \Delta\boldsymbol{u}_{n+1} \\
&= \boldsymbol{u}_k + \Delta\boldsymbol{u}_{k+1} + \ldots + \Delta\boldsymbol{u}_{n+1} \,,
\end{aligned}
\tag{3.36}
$$

where for a given time step t_{n+1}, the displacement increment is defined as $\Delta\boldsymbol{u}_{n+1} = \mathbf{x}_{n+1} - \tilde{\mathbf{x}}_n$, and $\Delta\boldsymbol{u}_k$ corresponds to the initial change in coordinates of a material particle that comes into existence at $t_k < t_{n+1}$. With this definition, the temporally discretized deformation gradient according to Equation (2.4) becomes

$$
\begin{aligned}
\boldsymbol{F}_k^{n+1} &= \frac{\partial \boldsymbol{\chi}_{d,n+1}}{\partial \mathbf{x}_n} \boldsymbol{F}_k^n \, \boldsymbol{I} \\
&= \left(\boldsymbol{I} + \frac{\partial \Delta\boldsymbol{u}_{n+1}}{\partial \mathbf{x}_n} \right) \boldsymbol{F}_k^n \, \boldsymbol{I} \\
&= \left(\boldsymbol{I} + \frac{\partial \Delta\boldsymbol{u}_{n+1}}{\partial \mathbf{x}_n} \right) \left(\boldsymbol{I} + \frac{\partial \Delta\boldsymbol{u}_n}{\partial \mathbf{x}_{n-1}} \right) \boldsymbol{F}_k^{n-1} \, \boldsymbol{I} \\
&= \left(\boldsymbol{I} + \frac{\partial \Delta\boldsymbol{u}_{n+1}}{\partial \mathbf{x}_n} \right) \left(\boldsymbol{I} + \frac{\partial \Delta\boldsymbol{u}_n}{\partial \mathbf{x}_{n-1}} \right) \ldots \left(\boldsymbol{I} + \frac{\partial \Delta\boldsymbol{u}_{k+1}}{\partial \mathbf{x}_k} \right) \boldsymbol{I}
\end{aligned}
\tag{3.37}
$$

for a material which comes into existence at time t_k. In Equation (3.37), $\boldsymbol{I}$ is the mixed identity tensor. The spatial coordinates of the body are updated based on the incremental displacement as follows

$$
\mathbf{x}_{n+1} = \tilde{\mathbf{x}}_n + \Delta\boldsymbol{u}_{n+1} \,. \tag{3.38}
$$

Note that the description of the discrete deformation gradient in Equation (3.37) is equivalent to the implementation used for the updated Lagrangian finite element method. The total deformation gradient $\boldsymbol{F}_{n+1}$ is generally necessary to compute the stress for hyperelastic materials, however, the total displacement $\boldsymbol{u}_{n+1}$ is not required since the coordinates are updated incrementally according to Equation (3.38). Therefore, the array of nodal displacements that is stored for each time step is the increment $\Delta\boldsymbol{u}_{n+1}$. With this in mind, the displacement update using the Newmark-β integration scheme is

$$
\Delta\hat{\boldsymbol{u}}_{n+1} = \Delta t_{n+1} \hat{\dot{\mathbf{v}}}_n + \frac{1-2\beta}{2} \Delta t_{n+1}^2 \hat{\dot{\mathbf{a}}}_n + \Delta t_{n+1}^2 \beta \hat{\mathbf{a}}_{n+1} \,. \tag{3.39}
$$

The tangent matrix in Equation (3.34) is derived by computing the Fréchet derivative of the residual for the discretized balance of linear momentum in Equation (3.33) with respect to the material velocity at t_{n+1}. Assuming the body forces and tractions do not depend on the material velocity, the elemental tangent matrix is computed as

$$
D\hat{\boldsymbol{R}}^e(\mathbf{v}_{n+1}^k) = D\left[\int_{\Omega_{n+1}^{e,k}} \left((\boldsymbol{N}^e)^T \boldsymbol{N}^e \bar{\boldsymbol{N}}^e \hat{\boldsymbol{\rho}}_{n+1}^e + (\boldsymbol{B}^e)^T \hat{\boldsymbol{T}}_{n+1}^e \right) dv \right] (\mathbf{v}_{n+1}^k) \,. \tag{3.40}
$$

In general, integration with respect to the spatial configuration can be pulled-back to a static reference configuration, and the expression shown on the right-hand side of Equation (3.40) simplifies to

$$\int_{\Omega_0^e} D\left[(\boldsymbol{N}^e)^T \boldsymbol{N}^e \bar{\boldsymbol{N}}^e \hat{\boldsymbol{\rho}}^e_{0,n+1} + (\boldsymbol{B}^e)^T \hat{\boldsymbol{T}}^e_{n+1} J^e_{n+1}\right](\mathbf{v}^k_{n+1})\, dV\,, \tag{3.41}$$

where Ω_0^e is the undeformed configuration of the material element, $J^e_{n+1} = det(\boldsymbol{F}^e_{n+1})$ is the determinant of the total deformation gradient at t_{n+1}, and $\hat{\boldsymbol{\rho}}^e_{0,n+1}$ is the mass density at t_{n+1} given as a function of the referential ordinates. In the case where the domain itself depends on the addition or removal of mass along the surface, Ω^e may contain material that came into existence at different times. In this setting, the pull-back of the given element to its reference domain Ω_0^e is non-trivial, and this domain itself may contain gaps or overlaps in an unstressed state. An approximate tangent can be computed by simply differentiating the terms inside the integral in Equation (3.40), leading to

$$D\hat{\boldsymbol{R}}^e(\mathbf{v}^k_{n+1}) \approxeq \int_{\Omega^e} D\left[(\boldsymbol{N}^e)^T \boldsymbol{N}^e \bar{\boldsymbol{N}}^e \hat{\boldsymbol{\rho}}^e_{n+1} + (\boldsymbol{B}^e)^T \hat{\boldsymbol{T}}^e_{n+1}\right](\mathbf{v}^k_{n+1})\, dv\,. \tag{3.42}$$

The tangent shown in Equation (3.42) is sufficiently accurate for cases when the material deformation is small, although it inherits errors as the kinematics become increasingly nonlinear. The tangent matrix in Equation (3.42) is sufficient for the simulations conducted in this dissertation. In the most extreme cases when the deformation becomes large, other approximate gradient methods such as Broyden's method [34, Chapter 11] may be used, although this was not explored in the current work.

Assuming a stress-deformation constitutive law that is explicitly a function of the gradient of the material displacements at the current iterate $\boldsymbol{u}^k_{n+1}$, and accounting for the temporal discretization shown in Equation (3.35), the derivative in Equation (3.42) further simplifies to

$$D\hat{\boldsymbol{R}}^e(\mathbf{v}^k_{n+1}) \approxeq \int_{\Omega^e} \left[(\boldsymbol{N}^e)^T \boldsymbol{N}^e \bar{\boldsymbol{N}}^e \hat{\boldsymbol{\rho}}^e_{n+1} + (\boldsymbol{B}^e)^T \left[D\hat{\boldsymbol{T}}^e_{n+1}(\boldsymbol{u}^k_{n+1})\right]\beta\Delta t^2_{n+1}\right] dv\,, \tag{3.43}$$

where $D\hat{\boldsymbol{T}}^e(\boldsymbol{u}^k_{n+1})$ is the Fréchet derivative of the Cauchy stress with respect to the current iterate of the material displacements.

For a body in equilibrium where inertia does not play a significant role, the incremental material displacement $\Delta\boldsymbol{u}$ becomes the primary variable rather than the material velocities. In this setting, the value of $\Delta\boldsymbol{u}_{n+1}$ at a given time t_{n+1} is obtained by solving the nonlinear system of equations, which is expressed for the k^{th} iteration as

$$\hat{\boldsymbol{F}}^k_{n+1}(\Delta\boldsymbol{u}^k_{n+1}) \;=\; \mathbf{0}\,. \tag{3.44}$$

Note that Equation (3.44) does not involve any time integration since the acceleration is zero.

The updated value of the surface-bound variable $\hat{\boldsymbol{\varphi}}_{n+1}$ at the time t_{n+1} is computed using the backward Euler method, and thus must satisfy the residual defined for the k^{th} iteration as

$$\hat{\boldsymbol{R}}_{\varphi}(\hat{\boldsymbol{\varphi}}^{k}_{n+1}) \;=\; \bar{\bar{\boldsymbol{M}}}^{k}_{n+1}(\hat{\boldsymbol{\varphi}}^{k}_{n+1} - \hat{\boldsymbol{\varphi}}_{n}) + \Delta t_{n+1}\left[\bar{\bar{\boldsymbol{L}}}^{k}_{n+1} + \bar{\bar{\boldsymbol{K}}}^{k}_{n+1}\right]\hat{\boldsymbol{\varphi}}^{k}_{n+1} - \Delta t_{n+1}\bar{\bar{\boldsymbol{F}}}(\hat{\boldsymbol{\varphi}}^{k}_{n+1}) \;=\; \boldsymbol{0}\,, \tag{3.45}$$

Due to the staggering of the global variables, the material velocity at t_{n+1} shown in Equation (3.31) is decoupled from the solution of $\hat{\boldsymbol{\varphi}}_{n+1}$. With the additional assumption that normal surface growth is explicitly a function of φ, the only unknown in Equation (3.45) is the surface-bound variable at the current time, $\hat{\boldsymbol{\varphi}}_{n+1}$.

3.3.3 Discretization of Surface Growth

In general, it can be impractical to know the domain of the intermediate configuration and the growth/resorption extensions for the entire time domain $\mathcal{I}$. For this reason, it is convenient to "freeze" time and evaluate the weighted residual only in space. The fields are thus evaluated for the entire spatial domain at discrete time intervals. Consequently, new material accreting on a body undergoing surface growth must do so in a discrete manner based on the selected time increment.

It is convenient to assume that the time interval Δt_{n+1} between two adjacent discrete time steps $(t_n, t_{n+1}]$ corresponds to a single instantaneous accretion/resorption increment. Moreover, each discrete time step is associated with a set of material points constituting a new reference state of the body. Therefore, the regions comprising the intermediate configuration at t_{n+1}, namely $\mathcal{M}^{t_{n+1}}$ and $\mathcal{G}^{t_{n+1}}$, are determined based on the single growth increment occuring in $(t_n, t_{n+1}]$, as schematically shown in Figure 3.1. It is additionally assumed that time-dependent Dirichlet and Neumann boundary conditions evolve in the same discrete manner prescribed by the increment size. In the case where surface growth/resorption takes place only on traction-free surfaces, as assumed in the examples presented in Section 3.5, no deformation occurs in the growth area during the interval $(t_n, t_{n+1}]$. Therefore, the initial position of a given accreting particle is determined based solely on the growth velocity, and $\overline{\boldsymbol{\chi}}_g$ trivially maps points from the initial positions at t_n to their identical current positions t_{n+1}. Assuming that the accreting particles have no associated residual stresses, the points that constitute the region $\mathcal{G}^{t_{n+1}}$ are deposited in a stress-free state in the intermediate configuration. The displacements of material points relative to their state of initial existence are zero, and correspondingly, $\boldsymbol{F}_{t_n}^{t_{n+1}} = \boldsymbol{I}$ in $\mathcal{G}^{t_{n+1}}$. For bodies containing points with non-zero velocity, material that is accreted at some time $t_g \in (t_n, t_{n+1}]$ in a stress-free state is assumed to have a velocity equal to that of the nearest point on the boundary of the body at time t_n. In essence, grown material is taken to move rigidly with the surface it is created from in the discrete interval $(t_n, t_{n+1}]$ during which its accretion occurs. Accordingly, the material acceleration of all points in the growth region $\mathcal{G}^{t_{n+1}}$ is the zero vector. With the aforementioned simplifications, the discretization strategy closely mirrors that of [18].

The resorption of the surface replaces the fields such as densities and velocities on the original boundary $\Gamma_a^{t_n}$ with those located at the positions of $\tilde{\Gamma}_a^{t_{n+1}}$ as an initial solution in the intermediate configuration, as shown in Figure 3.1. The set of material points, $\mathcal{M}^{t_{n+1}}$, that belong to the interior of the body carry all fields from the previous ungrown state onto the new intermediate configuration. This new reference state has an initial solution in $\mathcal{M}^{t_{n+1}}$ and on $\tilde{\Gamma}_a^{t_{n+1}}$ that conforms to the physical

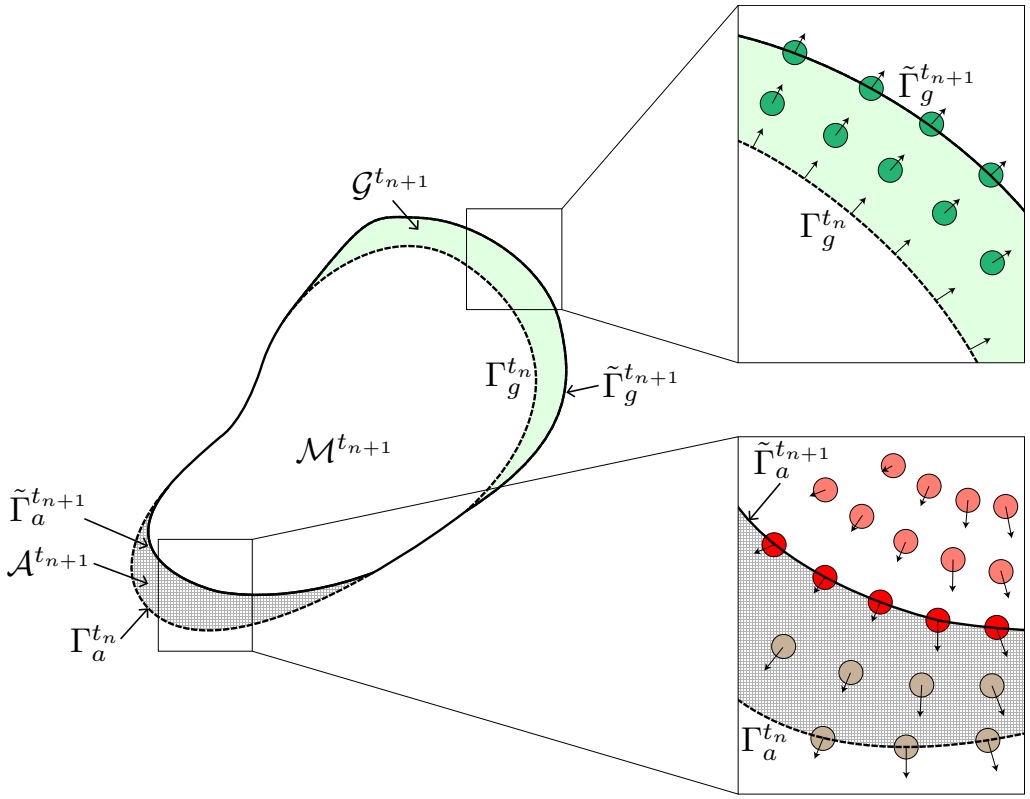

Figure 3.1: *Discretization of surface growth/resorption: Particles entering the body (shown schematically as green circles) between the discrete time increment* $(t_n, t_{n+1}]$ *are assumed to instantaneously accrete at* t_{n+1} *in a deformation-free/stress-free state, with velocities (shown as arrows) equal to the nearest neighbor of the ungrown boundary at* t_n*. Particles exiting the body (shown schematically as gray circles) between the discrete time increment* $(t_n, t_{n+1}]$ *are assumed to instantaneously resorpt at* t_{n+1}*. The new resorpted boundary coincides with locations previously located inside the body (shown as red circles).*

balance laws in its prior ungrown state, whereas the newly grown material in $\mathcal{G}^{t_{n+1}}$ and $\tilde{\Gamma}_g^{t_{n+1}}$ contains no prior history. This mismatch between the fields in $\mathcal{M}^{t_{i+1}}$ and $\mathcal{G}^{t_{n+1}}$ is manifested by discontinuities in the deformation gradient along the growth interface $\Gamma_g^{t_n}$.

The discretization of growth and resorption into finite increments which depend only on the state of the body at the evaluated time steps entails a connection between the increment size and the physics that the proposed numerical scheme aims to capture. Although discretized/discontinuous and continuous surface growth are fundamentally different processes, the numerical examples in Section 3.5 will illustrate that differences in the fields become negligible as the step size decreases and the growth increments appear increasingly continuous.

3.4 Meshing Algorithm

The incremental application of surface growth and resorption, as highlighted in the preceding section, requires an algorithm that can track boundary motion and adjust the surrounding mesh accordingly. Eulerian grids in conjunction with the level-set method have been used in the past to simulate surface growth phenomena, such as electrodeposition of copper and epitaxial growth of thin films [27, 5]. These implementations require infrastructure to activate/deactivate nodes, enforce boundary conditions along a moving interface, and solve multiple balance laws in different phases. Alternatively, surface growth/resorption applications can be modeled using an extension of the Arbitrary Lagrangian-Eulerian (ALE) method that isolates the domain of interest to a single phase (assumed here to be a solid), thus neglecting interactions with the ambient environment, as also done in [18]. The extended ALE method utilizes a mesh that conforms to the interface of the growing/resorpting domain, thus inherently capturing the combined motion of a body due to deformation and growth/resorption. In such a setting, the boundary of the mesh evolves based on the imposed mass flux across the surface, whereas the interior mesh is optimized to maintain various parameters, such as its initial shape or spatial uniformity. Given either an imposed surface growth/resorption velocity or one that is obtained through the solution of an interfacial variable such as φ in Equation (2.34), the mesh motion of the interior domain is obtained by solving Equation (3.17) with fixed boundary velocity.

3.5 Examples

3.5.1 Overview

In this section, two highly idealized examples are presented to demonstrate the numerical consistency and spatial/temporal convergence of the proposed surface growth/resorption algorithm. The first example consists of an ellipsoidal cylinder undergoing surface growth/resorption and rigid body motions, while the second example involves a hollow elliptical cylinder with an imposed time-dependent pressure on its inner boundary and surface growth/resorption on its outer boundary. In both cases, the material constitution is a neo-Hookean hyperelastic model of the form

$$\boldsymbol{T} \;=\; \frac{\mu}{J}\big(\boldsymbol{b}-\boldsymbol{i}\big)+\lambda\frac{log J}{J}\boldsymbol{i}\,, \tag{3.46}$$

where $J = det(\boldsymbol{F})$, $\boldsymbol{b} = \boldsymbol{F}\boldsymbol{F}^T$ is the left Cauchy-Green tensor, $\boldsymbol{i}$ is the spatial rank-two identity tensor, and λ, μ are material parameters akin to the Lamé constants of linear elasticity with values selected as $7.1E{+}02\ MPa$ and $1.8E{+}02\ MPa$ (respectively), which are typical for various plastics. With these parameters, the material is compressible with an infinitesimal Poisson's ratio of $\nu = 0.4$ under small deformation.

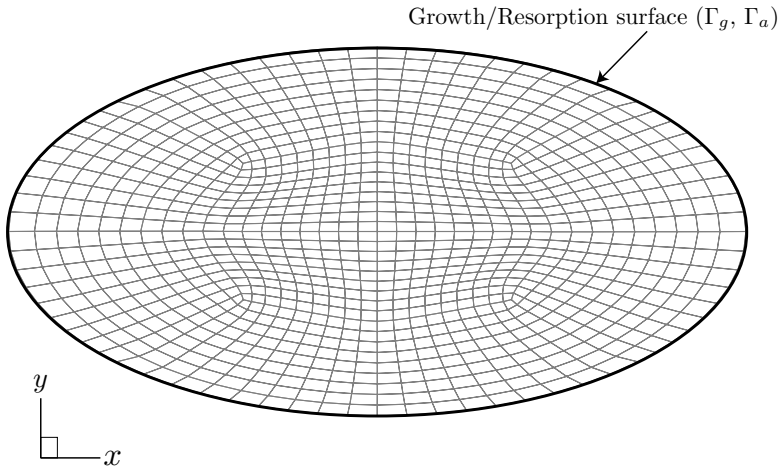

Figure 3.2: *Surface growth/resorption under rigid-body motions: Discretized ellipse in its initial state*

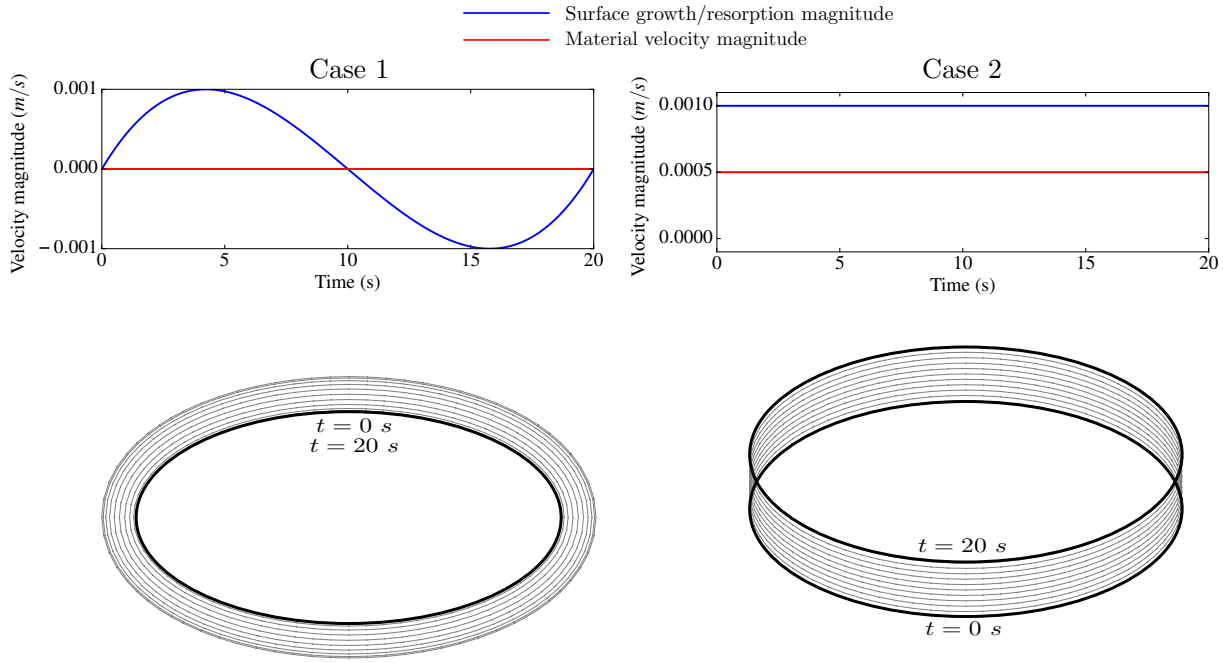

Figure 3.3: *Surface growth/resorption under rigid-body motions: Temporal evolution of growth/resorption and material velocities for Case 1 (left) and Case 2 (right), and the corresponding surface positions (shown in 2 s intervals with bold line indicating initial and final positions). Note that the initial and final positions for Case 1 coincide.*

3.5.2 Surface Growth and Resorption under Rigid-Body Motion

The first example consists of an ellipse with major and minor axes of diameters 80 *mm* and 40 *mm*, respectively. The discretized domain is shown in Figure 3.2. The mesh consists of 1044 bilinear quadrilaterals, and numerical integration of the weak forms is performed using a 2×2 Gauss-Legendre quadrature.

Two cases are examined:

1. Time-dependent uniform normal growth velocity:

$$\mathbf{v}_g \cdot \boldsymbol{n} = 5.2e\text{-}4\ t - 7.8e\text{-}5\ t^2 + 2.6e\text{-}6\ t^3 \quad m/s$$

2. Constant uniform growth velocity $\mathrm{v}_{gy} = 1.0e\text{-}3\ m/s$ throughout the external boundary and a constant material velocity $\mathrm{v}_y = 5.0e\text{-}4\ m/s$

The uniformly imposed growth/resorption and material velocities are plotted in Figure 3.3. Both cases assume a time step $\Delta t = 1\ s$ for $t \in (0, 20]\ s$ and an initial density $\rho = 1.0e3\ kg/m^3$. The ellipse is assumed to be in the state of plane strain with no external loading.

In both cases, the elliptical cylinder experiences addition or removal of particles under rigid-body motions. In the first case, the domain expands and contracts as the surface undergoes time-dependent accretion and resorption. In the second case, material is deposited onto the top end and simultaneously removed from the bottom end, while the body is treadmilling with a constant velocity in the y-direction. It is assumed that there are no stresses at the instant that material comes into existence in the growth region $\mathcal{G}$. In addition, The stresses on the ablating surface $\tilde{\Gamma}^a$ are equivalent to the values corresponding to the same positions in the interior of the ungrown body. Therefore, both cases result in a stress-free state as material is deposited or removed from the body. These simple cases confirm that for an initially unstressed body experiencing surface growth/resorption under isothermal conditions, elastic deformation is solely dependent on externally applied forces, and cannot be generated by surface growth or resorption alone.

3.5.3 Growth and Resorption of Elliptical Cylinder Undergoing Finite Deformation

In this section, simulation results of a hollow elliptical cylinder undergoing a constant growth/resorption velocity and a temporally increasing pressure along its outer and inner boundaries (respectively) are presented. The cross-section of the cylinder consists of an initial uniform 1.5 *m* inner radius, as well as 2 *m* and 3 *m* minor and major outer radii, respectively. The applied outward pressure is prescribed as

$$p(t) = 10^7\ t \quad Pa\ ,$$

within the range $t = (0, 1.0]\ s$.

Two separate simulations are conducted: in the first, the body undergoes surface growth (Case 1), while in the second, surface resorption (Case 2). The geometry and loading for the two cases are shown in Figure 3.4. The prescribed normal growth and resorption velocities are 0.5 m/s and

$-0.1\ m/s$, respectively. Plane strain is assumed. Inertial effects are ignored for simplicity, thus displacement increments are updated rather than the velocity increments, as detailed in Algorithm 2 of Appendix A.1. Appealing to double symmetry, only one quadrant of an ellipse is used to conduct the simulation with the origin located at the center of the ellipse, as is shown in Figure 3.4. The mesh consists of 28841 bilinear quadrilateral elements and is biased towards the outer surface exposed to growth or resorption. A 2×2 Gauss-Legendre quadrature is used to numerically integrate the weak forms. Additionally, a time increment of $0.025\ s$ is used.

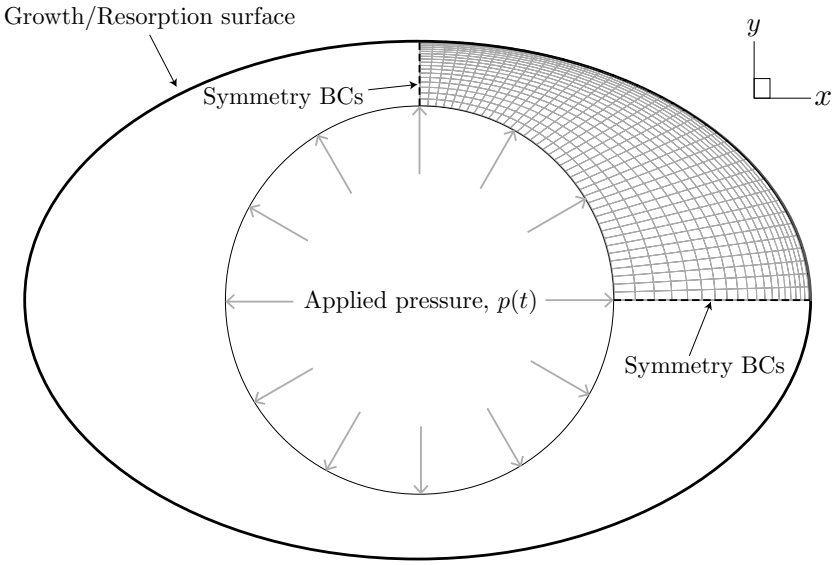

Figure 3.4: *Hollow elliptical cylinder: Loading and growth/resorption configuration (graded mesh used in simulation is shown for upper right quadrant). Coarse mesh shown for illustrative purposes.*

Accreted material is added in a stress-free state in the intermediate configuration. As mentioned in [23] and [35], material can, in principle, accrete with an inherited non-zero stress due to processes such as chemical reactions or phase changes. These effects are neglected in the current example since the knowledge of the underlying physical phenomena which produce surface growth and resorption are not considered.

The effects of surface growth and resorption on the final state of the deformations and stresses are highlighted in Figure 3.5 at the final time $1\ s$. The original set of material points is bounded by the solid red curve. The accretion of material leads to an increase in strength as is evidenced in the lower overall von Mises stress and pressure of the grown cylinder relative to the ablated one. The results in Figure 3.5 also indicate that the majority of load is taken by the material that constitutes the original boundary at $t = 0\ s$ for the grown cylinder, rather than redistributing throughout the new accretion along the boundary. The abrupt change in the von Mises stress and pressure is most pronounced along the minor radii, where steep gradients between the original boundary and the accreted regions exist. The cylinder undergoing resorption does not consist of any newly added material. The points of maximum and minimum stress therefore remain on the outer major and minor axes (respectively) throughout the resorption process.

It is inherently assumed that material is instantaneously deposited at each discrete time step.

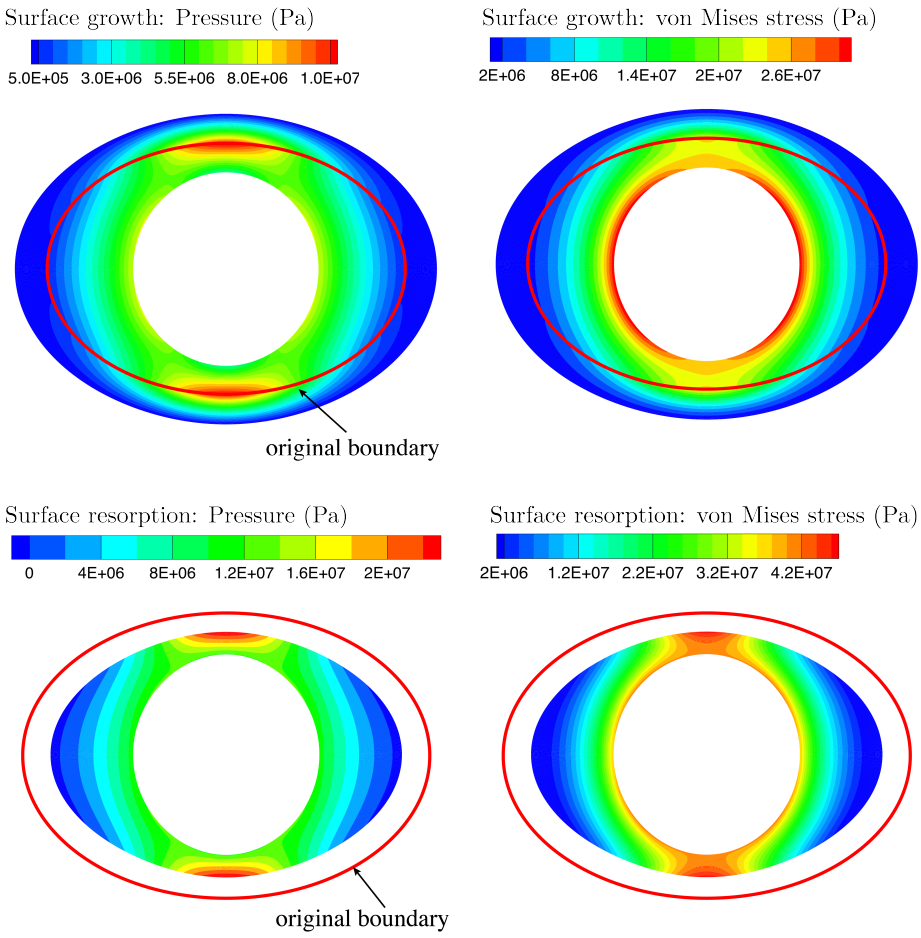

Figure 3.5: *Hollow elliptical cylinder: Contours of the pressure (left), and von Mises stress (right) for surface growth (top) and resorption (bottom)*

Therefore, the size of the time step relative to a fixed growth velocity dictates the length scale in which accretion takes place. For instance, selecting a coarse time step of $\Delta t = 0.1\ s$ leads to visibly discrete growth increments. This is illustrated in Figure 3.6 for the circumferential, radial, and longitudinal components of the Cauchy stress along a vertical and horizontal section of the ellipse at $t = 1\ s$. The observed "stair-stepping" pattern in the stress occurs due to the physical mismatch between the pre-existing material containing history of its own deformation and that of the newly added material which accretes onto the boundary with no stresses or deformations. The discontinuities are more prominent in the circumferential and longitudinal directions than they are in the radial direction. These discontinuities in the circumferential and longitudinal stress occur due to the contradicting effects of non-zero stresses that develop on the outer surface as the cylinder is loaded, and the stress-free state in which the material is initially deposited. On the contrary, the radial stress is zero along the outer surface due to the traction free boundary conditions, and hence maintains a continuous profile. Therefore, once each finite layer attaches to the cylinder,

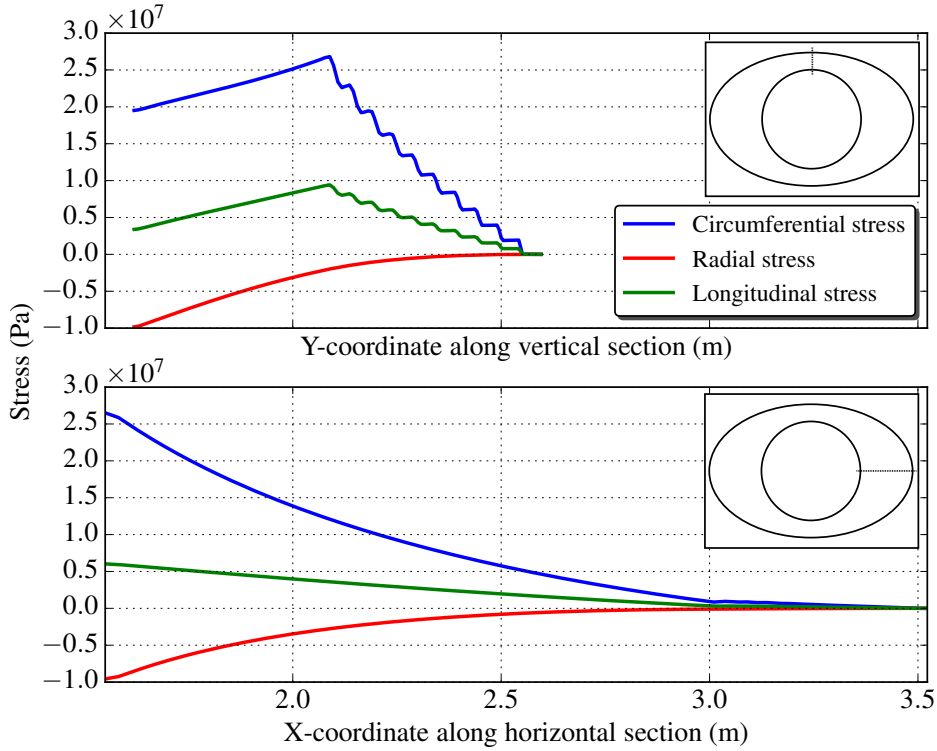

Figure 3.6: *Hollow elliptical cylinder: Circumferential, radial, and longitudinal components of the Cauchy stress along the minor radius (top) and major radius (bottom) for surface growth*

it primarily resists subsequent loading by deforming along the circumferential and longitudinal direction. Note that the mismatch in stresses between the grown and ungrown regions is more prominent along the minor radius than they are along the major radius since the circumferential stresses are greatest in this region. In addition to the discontinuity at each growth increment, the slope of the circumferential stress within the oldest growth increment nearly matches the region near the original boundary at $t = 0\ s$ whereas the newer increments consist of sequentially lower slopes. The outer-most layer of material exhibits near-zero slope in the circumferential component of the stress due to the assumed stress-free initial condition applied uniformly within the newly grown material. These trends highlight that the slopes of the stress across the growth interface nearly match, despite the fact that the stresses themselves are discontinuous.

As a physical consequence of the stress mismatch generated by growth or resorption increments, the cylinder maintains residual stresses upon unloading, as highlighted in Figure 3.7. The inner and outer surface are both traction-free once the body is unloaded, thus requiring the radial stress to be zero on these surfaces. However, the radial component of the Cauchy stress increases quadratically through the thickness of the cylinder cross-section, reaching a maximum near the center of the section thickness. The circumferential and longitudinal stresses are tensile along the inner surface and compressive at the outer surface thus implying that the unloaded section along the radius has

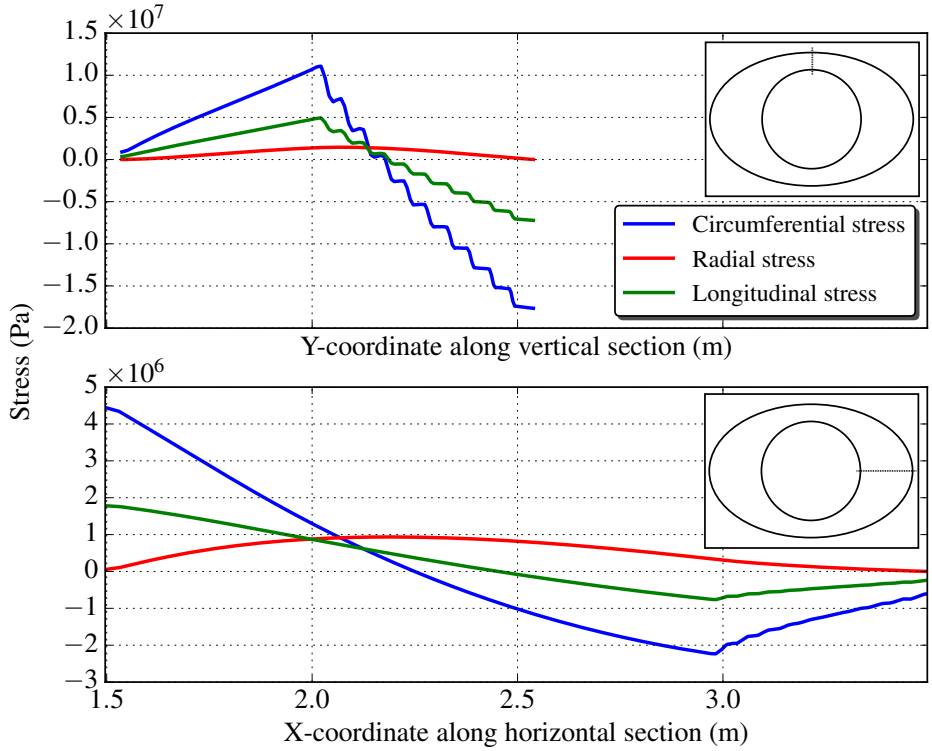

Figure 3.7: *Hollow elliptical cylinder: Circumferential, radial, and longitudinal components of the Cauchy stress along the minor radius (top) and major radius (bottom) for unloaded grown cylinder*

the tendency to bend.

The numerical results presented in [18] highlighted the same stair-stepping phenomenon exhibited in Figures 3.6 and 3.7 for one-dimensional spatial domains with the distinction that each growth interface align precisely with element boundaries. In this setting, the sharp discontinuities that appear at each growth interface are exactly captured. Although this distinction enhances the overall accuracy of the solution, the method does not easily extend to a generalized two-dimensional body. With the assumption that the discontinuities are approximated by steep gradients, the mesh motion is performed irrespective of prior locations of the growth interface. In this setting, it is assumed that the fields near each growth interface can be accurately represented as the mesh element size approaches zero.

Although the choice of time step affects the size of the growth increments and character of the solution, the discontinuities lose prominence and the solution converges to a single smooth curve as the size of the growth increments become infinitesimal relative to the scale of the physical domain. This convergence is highlighted in Figures 3.8 and 3.9 for three time steps: 0.1 s, 0.05 s, and 0.025 s. The fields of the resorpting body corresponding to case 2 are shown in dashed lines, and are also temporally convergent.

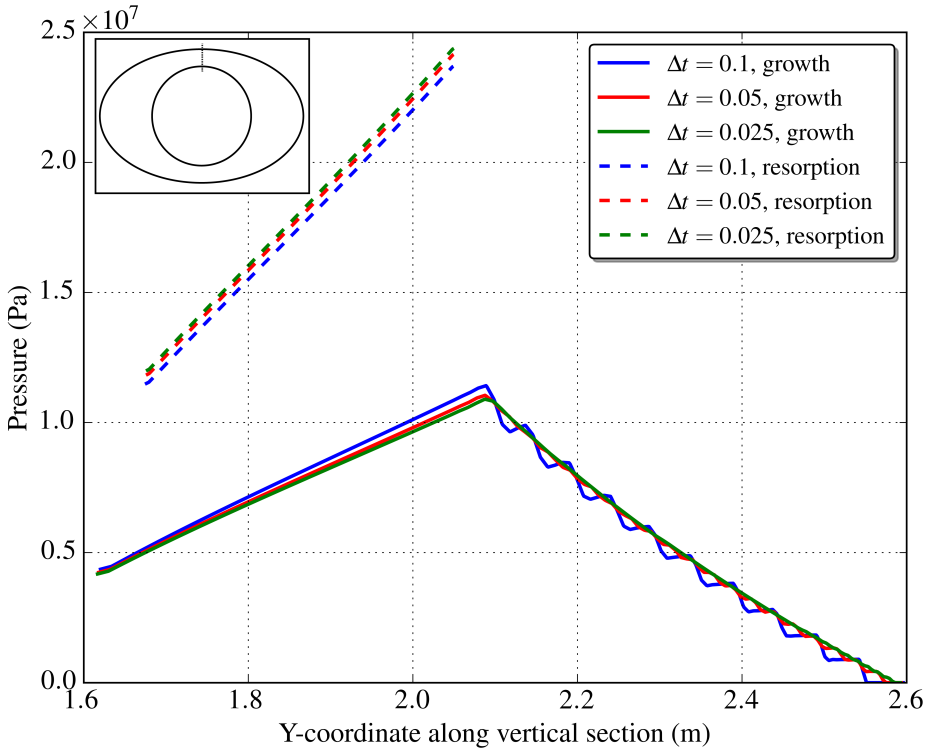

Figure 3.8: *Hollow elliptical cylinder: Temporal refinement of pressure along the minor radius for surface growth and resorption*

Uniform *h*-refinement of the mesh leads to a spatially convergent solution in the norm of the stored elastic energy of the error, as is shown in Figure 3.10. Solutions from six meshes were obtained with 741, 1711, 3081, 4851, 7021, and 28441 elements. The errors are taken relative to the solution of the finest mesh[2] (28441 elements) for each corresponding time step, and are computed based on the difference in displacement gradients. As expected, a strong positive correlation exists between temporal and spatial refinement for the grown cylinder due to the discontinuous nature of the solution for coarse time steps. In contrast, the resorpted cylinder exhibits nearly equal errors for a given mesh regardless of time step, thus indicating that temporal discretization does not play a significant role in the spatial convergence rate for the case of surface resorption.

The convergence rates for the biased mesh used in these simulations (Figure 3.2) depends on the metrics used to characterize the level of refinement of the spatial discretization. The results in Table 3.1 compares the convergence rates of the grown cylinder using four element size metrics: minimum, average, volume-averaged, and maximum element lengths. The difference in the norm of the stored energy of a neo-Hookean material asymptotically approaches that of a linear elastic

[2]To the author's knowledge, no known analytical solution exists in closed-form for a body undergoing finite deformation and surface growth/resorption. Therefore, it is assumed that the solution of the finest mesh is the "exact" solution.

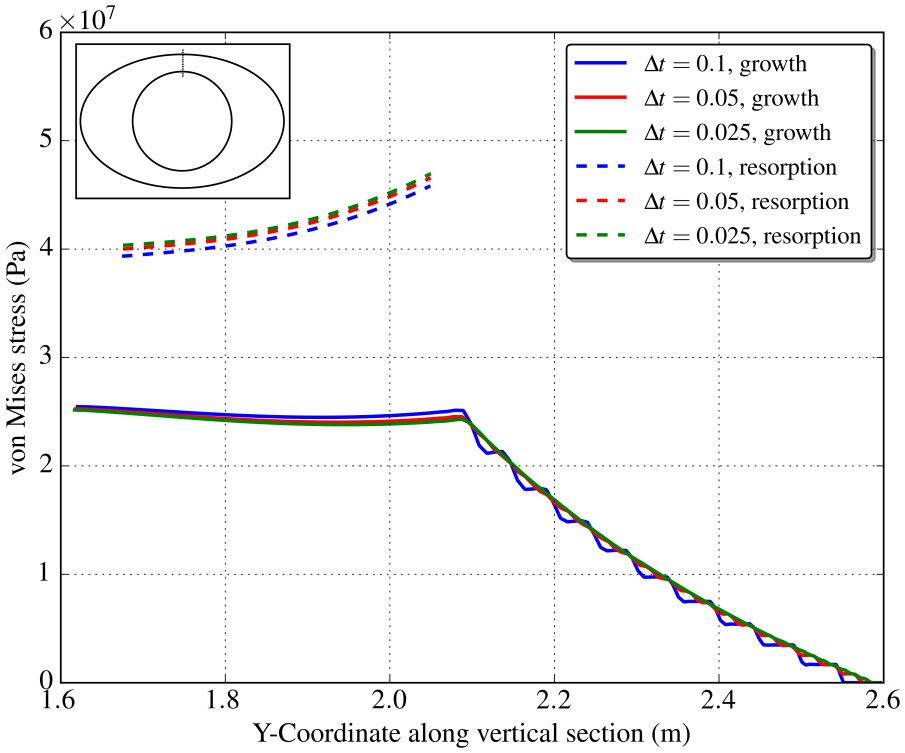

Figure 3.9: *Hollow elliptical cylinder: Temporal refinement of von Mises stress along the minor radius for surface growth and resorption*

material (also referred to as the energy norm) when the deformations are considered infinitesimal. Therefore, the theoretical convergence rate for a uniform grid and bilinear elements is 1. In an average sense, the convergence rates shown in Table 3.1 approach the theoretical value as the time discretization becomes refined.

3.6 Concluding Remarks

In this chapter, weak forms were developed based on the set of global balance laws presented in Chapter 2. The spatial discretizations were formulated within the context of the finite element method. Temporal discretization of the balance laws was developed, and an incremental interpretation of the deformation gradient based on the concept of the updated Lagrangian finite element method was introduced to describe the evolution of a domain consisting of an evolving set of material points. Additionally, an algorithm was proposed to numerically track the evolving growth/resorption front and assign fields in the intermediate configuration of the body.

Two examples were presented based on the proposed algorithm. The first example consisted of a body undergoing an imposed surface growth/resorption velocity with no applied stresses or deformations. In this example, no deformations or stresses were incurred by the body due to the

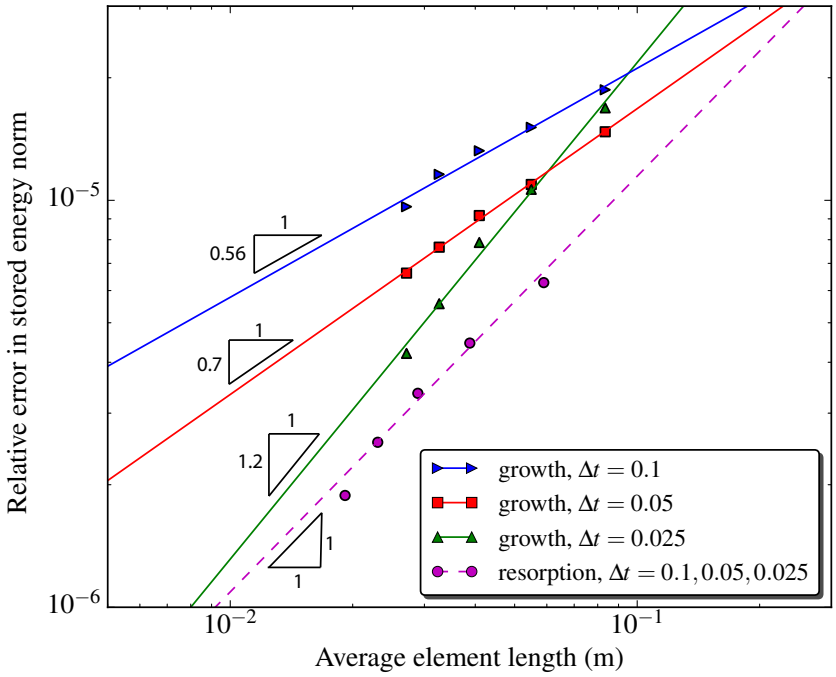

Figure 3.10: *Hollow elliptical cylinder: Spatial refinement convergence rates for surface growth and resorption using average element length*

growth and resorption. This verified that surface growth/resorption alone cannot induce stresses onto a body undergoing rigid-body motions. The second example consisted of a hollow elliptical cylinder in plane strain with an imposed internal pressure and external surface growth/resorption. The accretion of material onto the domain generated discontinuities in the fields along the growth interface due to the mismatch between the fields in the existing body and those on the accreted portions which contain no history of prior deformation. It was illustrated that as the time step is reduced, the accretion increments become infinitesimal, and the stress becomes spatially smoother in the growth area. Although the spatial convergence rate was sub-optimal with large accretion increments, it approached the expected value as the time step (and correspondingly the size of the accretion increments) was refined. This study established that the numerical accuracy for surface growth problems strongly depends on the size of the accretion increments relative to the scale of the entire domain.

	$\Delta t = 0.1$	$\Delta t = 0.05$	$\Delta t = 0.025$
Minimum element length	0.31	0.39	0.67
Average element length	0.56	0.70	1.22
Volume-averaged element length	0.65	0.82	1.43
Maximum element length	0.92	1.14	2.02

(a) *Surface growth*

	$\Delta t = 0.1$	$\Delta t = 0.05$	$\Delta t = 0.025$
Minimum element length	0.56	0.56	0.57
Average element length	1.02	1.03	1.05
Volume-averaged element length	1.16	1.18	1.20
Maximum element length	1.62	1.64	1.68

(b) *Surface resorption*

Table 3.1: *Hollow elliptical cylinder: Spatial refinement convergence rates based on element length scale metric*

Chapter 4

Application of Surface Growth/Resorption to Cell Migration

4.1 Overview

The work and results presented in this chapter showcase a novel approach for simulating cell migration through the use of the surface growth/resorption algorithm discussed in Chapters 2 and 3. The simulations illustrate the evolution of a cell's shape in a changing environment, and relate this surface phenomenon to the fields within the cell's interior. The models and numerical framework developed herein are among the first to relate cell migration to surface growth/resorption within a computational mechanics framework (alongside the recent works of [20, 21]) and hence serve as prototypes for future biomechanical modeling of cell migration. The mechanisms and kinetics of cell migration is described in Section 4.2, with a simple example illustrating the relation between cell shape and the concentration of certain proteins in Section 4.3. In Section 4.4, a viscoelastic model based on the works of [36, 37] is reviewed, and is utilized in conjunction with a mechanically-driven surface growth law in Section 4.5 to illustrate the effect of cell collision on its direction of migration.

4.2 Actin-Based Cell Motility

While many types of cells swim through biological fluids, some cells' primary motion is achieved by crawling on an underlying substrate. Neutrophils/macrophages (white blood cells), and keratocytes (epithelial cells) aid in the immune response to infection and prevent metastasis of cancerous cells by performing functions such as ingestion of pathogens. Connective tissue cells such as fibroblasts aid morphogenic development and remodeling of damaged structures. All these functions are achieved through a directed crawling motion of individual cells and groups of cells [38], [39, Chapter 16].

The coordinated migration of cells consists of four primary steps occurring *in tandem*: extension/protrusion, adhesion, translocation, and contraction, as shown in Figure 4.1 [40, Chapter 18]. The primary mechanism driving the extension/protrusion phase is thought to be the polymerization

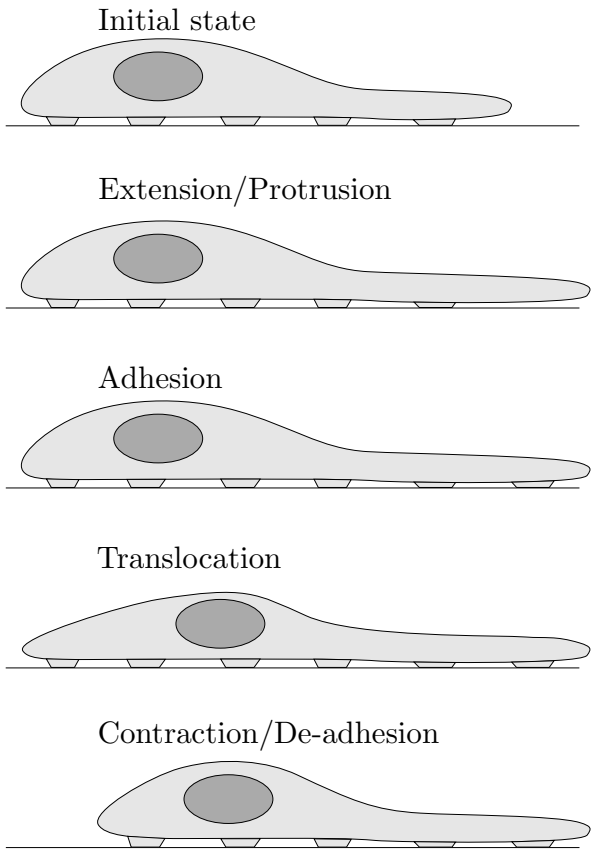

Figure 4.1: *Side view of cell in its crawling stages*

reaction of a bio-polymer termed actin (also termed F-actin or filamentous actin) along the leading edge of the cell termed the lamellipodium (or in certain cells can also occur in filopodia or pseudopodia) [41, 42]. Once the leading edge extends toward the direction of migration, it adheres to the underlying substrate via adhering molecules such as integrin. The adhesion was found to be most prominent in the lamellipodium, where it provides the traction force that resists the forward protrusion of the cell through cell-substrate binding [43]. Strong adhesion leads to persistent migration since it allows for actin filaments to remain stationary relative to the underlying substrate [38]. The position of a given material point of actin thus moves rearward as the cell progresses forward in a process termed retrograde flow. In addition to polymerization of actin, myosin motors near the cell cortex and within the cytoskeleton also enable retrograde flow by binding to actin filaments, producing forces by hydrolyzing the organic molecule adenosine triphosphate (ATP) as they move along individual actin filaments [43]. Through this process, acto-myosin contractile bundles pull the cell cortex forward leading to translocation of the cell body. The consumption of ATP alters its chemical composition to adenosine diphosphate molecules (ADP) in higher proportion near the cell rear, which attract actin depolymerizing factors (ADF) such as cofilin [44]. This protein is primarily responsible for dissociating filamentous actin into individual G-actin (globular actin) monomers, which eventually flow within the cytosol fluid back to the leading edge where they

can polymerize onto actin filaments again [45]. Lastly, the contractile forces in conjunction with weakened viniculin-rich focal adhesions enable the cell to swiftly contract its rear [44, 43].

4.2.1 Surface Growth Driven by Extension/Protrusion of Cell Membrane

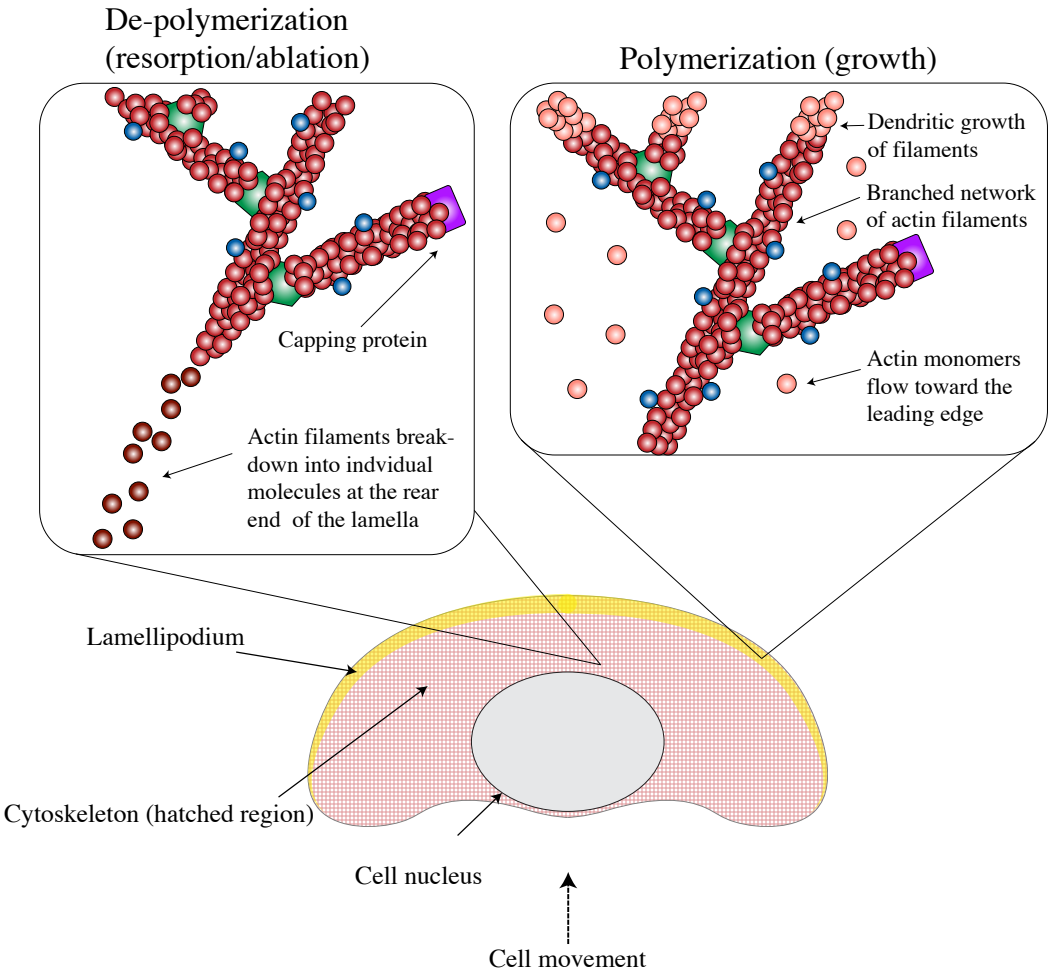

Figure 4.2: *Top view of cell migration mechanism via polymerization of actin filaments*

The polymerization along the lamellipodium/filopodium and depolymerization within the cytoskeleton together constitute a surface growth/resorption phenomenon at the nanoscale which leads to the apparent "treadmilling" motion of the entire cell on the microscale. Polymerization reactions of monomeric G-actin proteins on the order of several nanometers combine to form filaments tens of microns in length, thus resulting in a pushing motion in the lamellipodium. Within the cytoskeletal region, the actin filaments form a cross-linked network of polymers with linear densities on the order of several hundred per micron, in all encompassing a region approximately tens of microns in length and width, as shown in Figures 4.2 and 4.3 [38, 46]. Understanding the

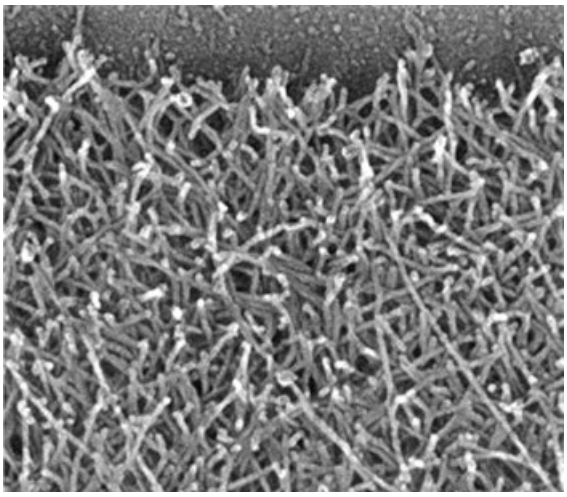

Figure 4.3: *Tomogram showing top view of nascent actin filaments at the leading edge of the lamellipodium (image length and width are both approximately* $1\mu m$*). Image taken from [44].*

dynamics and kinetics of actin is crucial in developing the correlation between polymerization, and the generation of protrusions leading to persistent migration.

The polymerization reactions are initiated by activating proteins such as WASp, and nucleator proteins such as the arp2/3 complex [38]. Actin filaments are polarized such that polymerization is preferential on its barbed end facing the leading edge of the cell, and less preferential on its pointed end. The polymerization and depolymerization of actin on the filament's barbed and pointed ends, respectively, depends on the concentration of G-actin in the surrounding cytosol fluid. Once a critical maximum G-actin concentration is reached, the barbed end grows at a rapid rate whereas a G-actin concentration below a critical concentration slows the growth of the barbed end and leads to depolymerization of the pointed end [38]. Once the actin polymerizes at its barbed end, it grows at a characteristic 70° angle relative to its parent branch in the lamellipodium, and forms parallel bands in filopodia of cells such as fibroblasts [47, 44, 41].

The elastic Brownian ratchet (EBR) model proposed in [42, 48] and reviewed in [38] offers a plausible explanation for understanding, both quantitatively and qualitatively, the nature of the protrusive force generated by growing actin filaments. This model proposed that the microscale dynamics of nascent actin filaments and the plasma cellular membrane are dominated by Brownian motion, which is induced by thermal fluctuations. This random motion implies that some actin filaments will be in direct contact with the membrane (attached filaments), while others will contain a small gap between the membrane and the end of the filament (working filaments). Working filaments are actively extending the cell towards the direction of migration by pushing the membrane. Once the working filament loses contact with the membrane, it can either be capped by capping proteins, or it can continue to grow if the G-actin concentrations are high enough and there is a sufficient gap to fit a single monomer. The attached filaments are in contact with the membrane and are in tension until they dissociate and hence become working filaments. The EBR model inherently assumes that new branches of actin filaments form prior to attachment, and hence, simply attach to existing filaments with no orientational preference [38].

The relation between growth/protrusion velocity of the lamellipodium and load that resists forward migration of the cell has been examined in numerous experiments, among which include [49, 50, 51]. In [51], bundles of actin such as those occurring in protruding filopodia are grown *in vitro* by providing monomeric G-actin for polymerization. The growth occurs until the actin filaments encounter a barrier. The stall force resulting in no net growth was correspondingly measured, and determined to be representative of the stall force for a single actin filament. The authors of [51] concluded that bundles of actin have a net compressive strength representative of a single filament, hence providing no combined strengthening. The authors of [49] measured the polymerization force of a network of actin filaments that were grown *in vitro* through the use of an atomic force microscope (AFM) cantilever that essentially acts as a deformable spring. The observed velocity of the AFM tip was inversely proportional to the load, with an exponentially increasing sensitivity as the measured force increased until the velocity reached zero, corresponding to the stall force. This identical trend between the growth velocity and resisting load was replicated in [50] with a migrating keratocyte cell colliding onto an AFM cantilever. The relation between growth velocity and protrusion force was constructed numerically using the EBR model in [48]. However, the results indicated a large decrease of the growth velocity with low resistance forces, which is contrary to the trends shown experimentally in [49, 50]. Other models such as the autocatalytic model developed in [52, 53, 54] provide a force-velocity relation that more closely captures experimental data at lower forces, however, discrepancies in the precise trends still exist.

Although the understanding of specific micro-mechanisms that drive protrusion and generate forces remains an active research topic, various works have related the overall shape and curvature of the leading edge to the underlying chemical kinetics of persistently migrating cells such as keratocytes using mathematical models and numerical simulations. In [46], transient differential equations were developed that determined the growth velocity and leading edge shape as a function of actin densities of left and right oriented filaments. The numerical solutions match the experimental observations which correlate high concentrations of actin to a flatter leading edge, and consequently, more persistent migration. Similar trends were observed in [55]. The authors assert that strong localization of actin-binding proteins such as vasodilator-stimulated phosphoroprotein (VASP) along the leading edge allows for efficient polymerization of actin, which corresponds to higher growth velocities. The level of polymerization also has a direct effect on the coherence and shape of the cell. The results in [55] correlate the efficient polymerization of actin to a smooth and flat leading edge which allows the keratocyte to migrate persistently while maintaining a canoe-like shape. On the contrary, cells that do not polymerize efficiently were observed to have a diffused VASP concentration with less uniform localizations throughout the cytoskeleton thus generating a less coherent "D" shaped cell with rough edges. The authors of [55] subsequently matched the experimental observations with numerical results that consist of phenomenological rate equations for total density of left and right oriented actin filaments as functions of VASP association/dissociation rates, lateral flow, and branching and capping. Various other notable mathematical models, numerical simulations, and experimental observations on the relation between actin polymerization, persistent growth/migration, and the resulting cell shape include [56, 57, 58].

4.3 Phenomenological Model of Cell Migration

Although much of the biophysics of migrating cells remains unknown, numerical models of cell migration have been introduced in various prior works. In [58], a two-dimensional model of a migrating cell is constructed that accounts for various intracellular interactions, such as orientation of F-actin and concentrations of myosin and G-actin, and their effects on cell shape and orientation. A collection of later works focused on the concentrations of extracellular chemo-attractants and the resulting coordinated migration patterns [59, 60].

In this section, simulations of the cell migration of a fish epidermal keratocyte are conducted through a surface balance law of the form shown in Equation (3.7). The concentration of G-actin present throughout the lamellipodium correlates to the polymerization rate, as highlighted in [46]. Therefore, the variable φ is interpreted as the concentration of G-actin on the surface of the cell. The intracellular mechanics is ignored for simplicity. With the assumption that the cell treadmills in the $+y$ direction, the source term $f(\varphi, \mathbf{x}_{\partial\tilde{\mathcal{R}}})$ is expressed as

$$\begin{aligned} f(\varphi, \mathbf{x}_{\partial\tilde{\mathcal{R}}}) &= n(\mathbf{x}_{\partial\tilde{\mathcal{R}}}) - d\varphi \,, \\ n(\mathbf{x}_{\partial\tilde{\mathcal{R}}}) &= n_{max} \frac{y - y_{min}}{y_{max} - y_{min}} + n_{min} \,, \end{aligned} \tag{4.1}$$

where $n(\mathbf{x}_{\partial\tilde{\mathcal{R}}})$ is a linear nucleation term that favors high G-actin density at the leading edge of the cell, and d is a constant dissociation term. The peak nucleation has a value of n_{max} which occurs at the highest point on the cell, y_{max}. Likewise, the lowest nucleation n_{min} occurs at the minimum y-coordinate of the cell, y_{min}. Between the two extreme points, the nucleation term is simply a linear interpolation between n_{max} and n_{min}. This nucleation profile is schematically shown as a function of the surface coordinates of the cell in Figure 4.4.

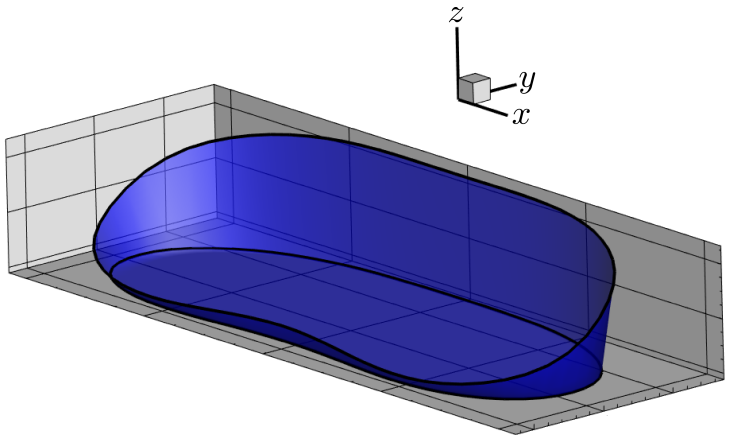

Figure 4.4: *Nucleation profile of G-actin along the surface of a keratocyte migrating in the $+y$ direction. The domain of the cell lies on the xy-plane and the height along the z-axis corresponds to the value of the nucleation of G-actin along the surface of the cell.*

Healthy keratocyte cells generally migrate in a given direction with little variation in total area

and shape [46]. The growth/resorption velocity of a migrating cell with no change in shape is characterized by the graded radial extension (GRE) model [61]. This model assumes that the surface growth velocity has the following form:

$$\mathrm{v}_{gn} \;=\; \mathbf{V} \cdot \boldsymbol{n}\,, \tag{4.2}$$

where $\mathbf{V}$ is the overall treadmilling velocity of the cell, as shown in Figure 4.5. By definition, this treadmilling velocity $\mathbf{V}$ is constant in space, although it can vary in time. Based on the GRE model, the shape of the cell is assumed from the outset and convected with a normal growth velocity of the form shown in Equation (4.2). It is important to note that the GRE model is phenomenological in nature; more specifically, it neglects the individual mechanism that drive the polymerization of actin leading to the observed treadmilling motion, including among others, interactions of the cellular cytosol fluid and plasma membrane with the F-actin network in the lamellopodium and chemical kinetics of actomyosin bundles [61, 48, 46].

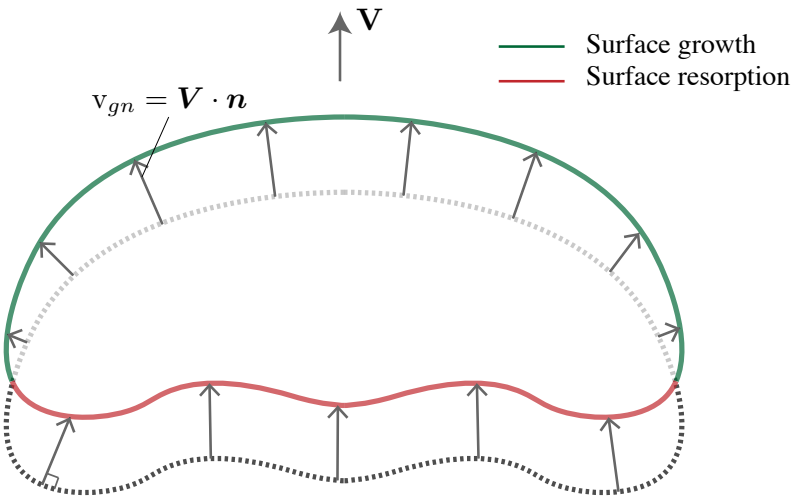

Figure 4.5: *Treadmilling surface growth/resorption velocity definition based on the graded radial extension model*

The overall treadmilling velocity is constant along the surface of the cell, and is defined in terms of the G-actin density as

$$\mathbf{V} \;=\; \alpha \mathbf{d} \frac{\int_{\partial\tilde{\mathcal{R}}} \varphi \, d\Gamma}{\int_{\partial\tilde{\mathcal{R}}} \, d\Gamma}\,, \tag{4.3}$$

where α is a proportionality constant and $\mathbf{d}$ represents the unit vector of the direction of cell migration. Note that v_{gn} is frame-invariant under the assumption that both $\mathbf{V}$ and $\boldsymbol{n}$ transform as vectors in Euclidean space, $\mathbf{V}' = \boldsymbol{Q}\mathbf{V}$ and $\boldsymbol{n}' = \boldsymbol{Q}\boldsymbol{n}$ for any proper orthogonal rotation $\boldsymbol{Q}$.

The numerical procedure highlighted in Algorithm 1 of Appendix A.1 was used to solve for the G-actin density φ using backward Euler with a time step of $\Delta t = 0.01\ s$. For simplicity, the intracellular physics was not modeled, hence material velocities and densities $\mathbf{v}$ and ρ were not solved for. The entire mesh consists of 972 bilinear quadrilateral elements, which contains 72

piecewise linear surface elements. The balance law for the G-actin concentration is numerically integrated using a two-point Gauss-Legendre quadrature. The new position of the boundary $\partial\mathcal{R}$ was determined based on the growth law in Equation (4.2) once the value of $\hat{\boldsymbol{\varphi}}^{j}_{n+1}$ was obtained for a given staggered iteration j. In this example, the only unknown is the global vector of G-actin concentrations $\hat{\boldsymbol{\varphi}}$. Since the positions of the surface depend on the surface growth velocity (and hence the G-actin concentration), the global coordinates and $\hat{\boldsymbol{\varphi}}$ are updated in a staggered manner. The process of updating the positions of the boundary, re-solving for $\hat{\boldsymbol{\varphi}}^{j}_{n+1}$, and determining $\mathbf{v}^{j}_{g,n+1}$ was repeated until the change in the updated coordinates converges to a user-specified tolerance, which is generally 2-3 orders of magnitude smaller than the length scale of the domain.

Figure 4.6 illustrates the evolution of a treadmilling keratocyte within a 120 s time frame for the parameters listed in Table 4.1. The domain includes lamellipodium and cytoskeleton regions where the F-actin density is most prominent. The initial G-actin density along the cell boundary varies linearly in the same manner that the nucleation does, and has the form (for a given point on the boundary): $\varphi_0 = n(\mathbf{x}_{\partial\tilde{\mathcal{R}}})/d$. Although the cell evidently maintains its shape throughout the migration process, the actin filaments along the surface are all propelled towards the rear edge of the cell, predominantly along the portions where the angle between the normal vector and the treadmilling direction vector $\boldsymbol{d}$ is greatest.

Symbol	**Name**	**Value**
n_{max} *	Maximum G-actin nucleation	10.0 $/\mu ms$
n_{min}	Minimum G-actin nucleation	0.01 $/\mu ms$
d *	Dissociation constant	0.1 $/s$
α	Treadmilling velocity proportionality constant	3.0e-04 $\mu m/s$
K	Diffusion constant	1.0e-06 $\mu m^2/s$

* Taken from [46] with some modifications

Table 4.1: *Parameters used for treadmilling cell*

To determine the steady-state G-actin density and its sensitivity to cell shape, a series of 15 simulations were conducted by varying the radius of curvature at the leading point of the cell labeled in Figure 4.7 between $3.5\mu m$ and $85\mu m$. The results shown in Figure 4.7 indicate that the treadmilling velocity $\mathbf{V}$ based on Equations (4.1) to (4.3) increases as the leading edge of the cell becomes flatter. This phenomenon was widely studied in prior works, such as [46, 55], which attributed the change in leading edge curvature to changes in concentrations of WASp proteins and F-actin density within the cell. Here, the results indicate a similar trend purely based on the variation in cell geometry.

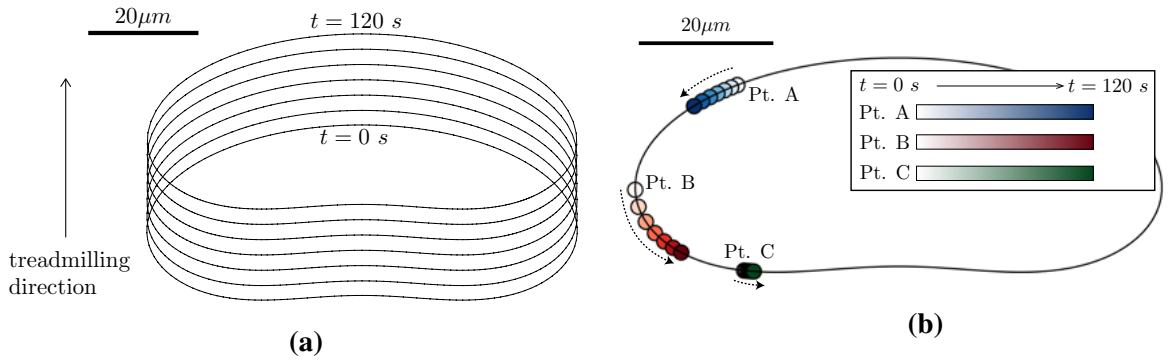

Figure 4.6: *Treadmilling shown in* 20 *s intervals with respect to (a) laboratory frame and (b) fixed points along cell boundary*

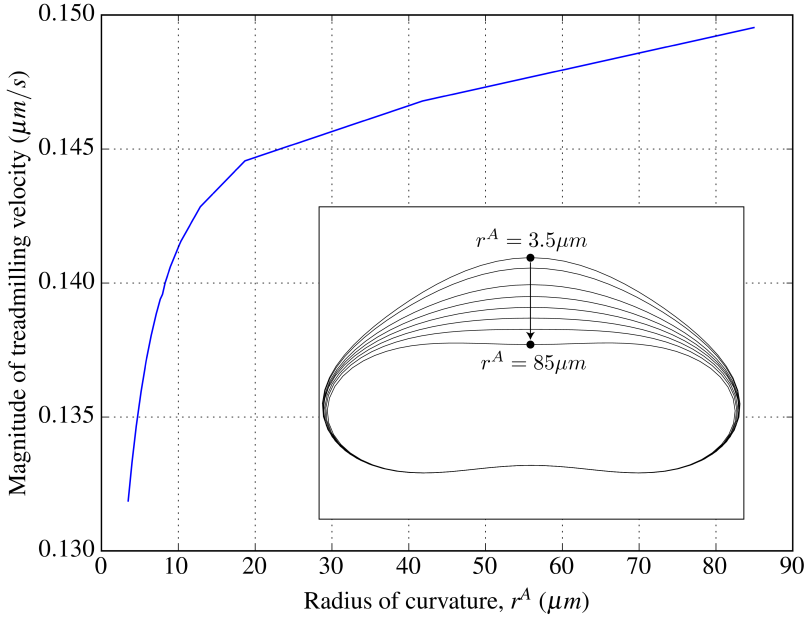

Figure 4.7: *Relation between magnitude of treadmilling velocity at steady-state and radius of curvature at the leading edge for various cell shapes*

4.4 Viscoelastic Constitutive Law

The ability of actin to grow or resorpt on the leading and trailing edges of the cell cytoskeleton relies on the stresses and deformation of individual actin filaments as well as the homogenized fields throughout the actin network. A constitutive law was developed in [62, 63, 36, 37] to capture the mechanics of the cytoskeleton based on the properties of individual filaments and the homogenized isotropic actin network. The constitutive framework used herein is summarized in Sections 4.4.1

and 4.4.2.

4.4.1 Microscale Model of Actin as a Semi-flexible Biopolymer

The cytoskeleton of migrating cells consists of cross-linked semi-flexible polymer chains in the form of actin filaments, intermediate filaments, and bundles of bound actin microtubules which on the cell scale, form a viscoelastic gel. In living cells, non-uniform distributions of actin-binding proteins and external stimuli such as motor protein activity determine the rheological properties of the cytoskeletal network [64]. Models such as the active polar gels developed in [65, 66] aim to capture the hydrodynamics of the viscoelastic actin network by treating it as an anisotropic nematic liquid crystal composed of polarized microfilaments undergoing ATP hydrolysis and other active chemical reactions. The works of [67, 68] provide numerical examples where the active gel model was used to simulate the *in vivo* mechanical response of the cell.

In vitro experiments such as [69, 70, 71] characterized the entropic properties of the actin biopolymer networks on the microscale in terms of the cross-linker and F-actin concentrations, and linked these qualities to the observed viscoelastic response on the cell-scale. The works of [71, 70] associated the short-term linear response of *in vitro* grown actin to the entropic stretching of actin filaments, dominated by the presence of cross-links, which are chemicals that bind multiple chains of protein filaments to form junctions. In this regime, the deformation of a tightly-linked network with high cross-linker and F-actin concentrations is dominated by stretching of the filaments on the microscale due to the decrease in available conformations of the filaments, and hence, a decrease in entropy [72, Pages 607–617]. The nonlinear response of the actin networks was hypothesized in [71] to take place when unbinding and rupture of cross-links occurred, leading to longer filaments with more available conformations and higher entropy whose deformations are dominated by bending due to thermal fluctuations.

The physical characteristics and mechanical behavior of actin filaments are encompassed by a theory that describes semi-flexible biopolymers termed worm-like chains (WLC), which was first proposed in terms of discrete segments in [73], and later adapted to describe entire polymers chains in various works such as [72, Pages 607–617], [62, 36, 74, 75, 76]. This theory assumes that the size of the individual monomers are vastly smaller in magnitude compared to the full contour length of the polymer chain that they combine to form, hence appearing as a continuous rod on the entire polymer chain scale. Additionally, the persistence length of worm-like chains, a characteristic length scale which defines the lower limit where thermal fluctuations induce bending, is significantly larger than the size of the individual segments/monomers it is composed of. Such polymers consist of apparently continuous individual segments which can resist bending, and are termed semi-flexible due to their relatively stiff mechanical response and straight appearance, as opposed to the natural tendencies observed in softer polymers to form entangled chains [74].

The Holzapfel-Ogden β-model developed in [62] derives the mechanical response of worm-like chains through a series of closed-form analytical expressions based on energy principles described in [75, 76] and the equilibrium of an extensible semi-flexible rod. The relation between filament force f and the total stretch relative to the filaments ends λ is expressed as

$$\frac{r}{L} = 1 + \frac{f}{\mu_0} - \frac{(1 + 2f/\mu_0)(1 + f/\mu_0)^{\beta}(1 - r_0/L)}{\{1 + fL^2/(\pi^2 B_0) + (fL)^2/(\pi^2 B_0 \mu_0)\}^{\beta}}\,, \tag{4.4}$$

where the current end-to-end distance between cross-links r is defined as

$$r = \lambda \lambda_0 r_0\,, \tag{4.5}$$

and the bending modulus B_0 is defined as

$$B_0 = L_p k_b T\,. \tag{4.6}$$

Equation (4.4) defines an implicit equation for the filament force f at its ends given a stretch λ. The values of the parameters in Equations (4.4) and (4.6) as well as their physical relevance is highlighted in Table 4.2. These parameters are chosen based on the experimental observations as well as data fits, both of which were conducted in [37]. The closed-form expression in Equation (4.4) is based on the theory of Cosserat rods with both extensional and bending energies, and is derived in [62].

Symbol	Name	Values	Physical relevance
λ_0	Initial pre-stretch	1.012	Stretch corresponding to zero force
r_0	Unstressed end-to-end distance	1.0 μm	End-to-end distance corresponding to zero force
L	Contour length	1.048 μm	Total initial arc length of actin filament
μ_0	Extension modulus	38.6 nN	Material constant describing sensitivity of filament to tensile deformation
β	Extensional exponent	0.438	Varies the sensitivity of load to changes in the stretch
L_p	Persistence length	16 μm	Maximum length scale for which the direction of tangent vector along polymer are correlated; also minimum length scale for which thermal fluctuations induce polymer bending.
k_b	Boltzmann constant	1.38E-23 J/K	Relates the probability of energy states to total entropy
T	Temperature	294.4 K	Approximate ambient temperature

Table 4.2: *Typical values (obtained from [62, 63] and Table 2 of [36]) and physical relevance of parameters in force-extension relation for worm-like polymer chain shown in Equation* (4.4)

The relation between the force and extension is sensitive to each of the parameters listed in

Table 4.2 and can vary from purely entropic in nature to purely mechanical. The extension modulus μ_0 controls the degree to which mechanical response can dominate. For instance, a high extension modulus correlates to an inextensible filament dominated by entropic stretching, as shown in Figure 4.8a. The natural tendency of actin filaments is to increase entropy and become more disordered, according the Second Law of Thermodynamics. Therefore, an increasing force must be applied as the filament extends in order to initially stretch the filament since this implies a decrease in the entropy and hence, the number of possible conformations [74]. Likewise, the force required to stretch the inextensible filament to its full contour length is infinite since this corresponds to a single straight conformation with zero entropy. The extensibility provided through a finite extensional modulus permits mechanical stretching of the filament once it reaches a straight conformation. In such a setting, decreasing the extensional modulus leads to a lower force required to mechanically stretch the filament.

The persistence length of the filament (defined in Table 4.2) controls the entropic response. As is highlighted in Figure 4.8b, a persistence length close to the contour length of the filament leads to a softer response in the low-stretch regime, with an exponentially increasing sensitivity of the force to the stretch as the filament reaches its contour length. On the contrary, a filament with a high persistence length relative to its contour length exhibits a purely mechanical response dominated by a gradual hardening at higher stretches. The extensional exponent β has a similar effect as the persistence length, as is shown in Figure 4.8b. An increase in the extensional exponent generates a sharper increase in stiffness with a relatively small transition between entropic and mechanical stretching as the filament end-to-end distance approaches its contour length whereas small extensional exponents lead to a smooth transition between entropic and purely mechanical behavior. However, unlike the extension modulus and persistence length, the extensional exponent is not a measurable quantity of individual actin filaments. Therefore, the value of β is selected to fit experimental data of entire actin networks, and can vary from case-to-case [36].

4.4.2 Continuum-level Representation of Actin Network

The closed-form expression of the filament model proposed in [62] and reviewed in Section 4.4.1 is ideal for a finite element application due to the fact that it does not require a sophisticated numerical algorithm to resolve the mechanics on the individual filament scale (the interested reader is referred to [77] for an alternative approach that does incorporate multiscale numerical algorithms to resolve the filament mechanics). This model was incorporated into a continuum-level constitutive law in [36, 37] to describe mechanics of a cell-scale actin network, which is reviewed below.

Assume a multiplicative split of the macroscale deformation gradient $\boldsymbol{F}$ into isochoric and spherical parts,

$$\boldsymbol{F} = \bar{\boldsymbol{F}}\boldsymbol{F}_{sph}\,, \tag{4.7}$$

where $\boldsymbol{F}_{sph} = J^{1/3}\boldsymbol{I}$, $\bar{\boldsymbol{F}} = J^{-1/3}\boldsymbol{F}$, and $J = det(\boldsymbol{F})$. The deformation of the actin filaments only affects the macroscopic isochoric deformation, therefore its motion is defined by $\bar{\boldsymbol{F}}$. With this assumption, suppose a semi-flexible actin filament exists in a reference configuration $\mathcal{R}_0$ whose individual kinematics are described by an isochoric macroscale deformation gradient $\bar{\boldsymbol{F}}$. Tangent

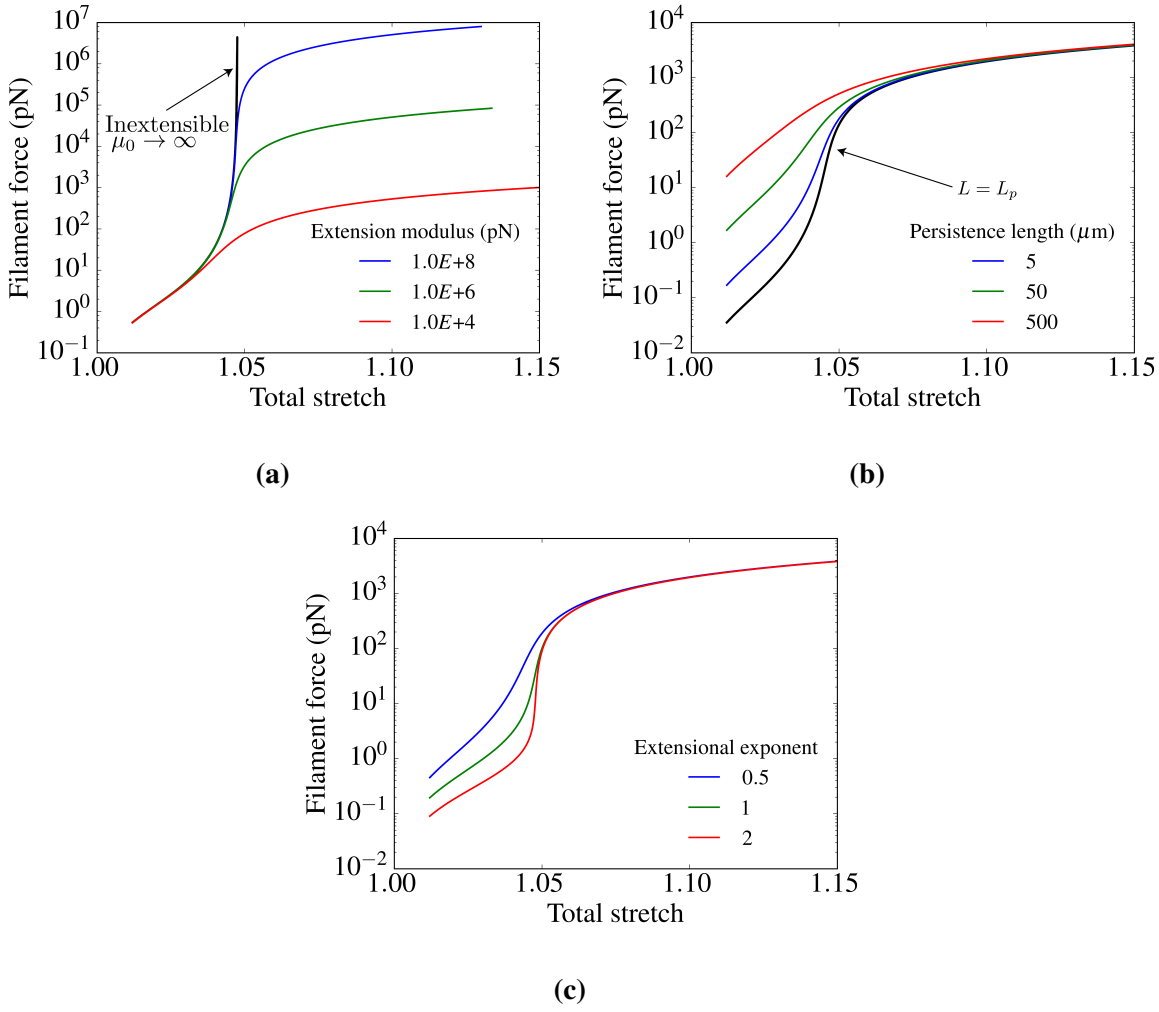

Figure 4.8: *Relation between filament force and stretch for different (a) extension moduli, (b) persistence lengths, and (c) extensional exponents*

vectors $d\mathbf{x}$ in the spatial configuration $\mathcal{R}$ are thus defined by a linear mapping acting on referential tangent vectors $d\mathbf{X}$ as

$$d\mathbf{x} = \bar{\boldsymbol{F}}\, d\mathbf{X}\,, \tag{4.8}$$

as shown in Figure 4.9. The microstretch $\bar{\lambda}$ is defined as

$$\bar{\lambda} = ||d\mathbf{x}|| = d\mathbf{X} \cdot \bar{\boldsymbol{C}}\, d\mathbf{X}\,, \tag{4.9}$$

where $\bar{\boldsymbol{C}} = \bar{\boldsymbol{F}}^T \bar{\boldsymbol{F}}$. The homogenized stretch at a given material point is computed by integrating the microstretch over a representative unit sphere (based on the non-affine microsphere model

highlighted in [78]) and hence takes the following form:

$$\lambda = \langle \bar{\lambda} \rangle = \frac{1}{|\mathcal{S}|} \left[\int_{\mathcal{S}} \bar{\lambda}^p \, da \right]^{1/p} . \tag{4.10}$$

In Equation (4.10), the averaging operator is denoted by $\langle \cdot \rangle$. Additionally, $\mathcal{S}$ denotes the domain of the unit sphere, and p is an averaging parameter. The averaging scheme in Equation (4.10) implies that the microstretch $\bar{\lambda}$ is not equivalent to the homogenized stretch λ, therefore, the deformations of the actin network are non-affine relative to the macroscale deformation [36]. The non-affinity of deformation modes in semi-flexible polymers occurs when the material microstructure consists of disordered fibers, which energetically favors bending rather than stretching generally leading to a softer macroscopic response [74, 79].

A 21-point quadrature was proposed in [78, 80] to approximate the homogenized stretch in Equation (4.10) by imposing

$$\langle \boldsymbol{t} \rangle = \mathbf{0}, \quad \langle \boldsymbol{t} \otimes \boldsymbol{t} \rangle = \frac{1}{3} \boldsymbol{I} \tag{4.11}$$

on the discrete averaging operator, where $\boldsymbol{t}$ is an orientation vector on an undeformed unit sphere. The first requirement ensures that the integral of any linear vector function vanishes on a spherical domain as it should, while the latter constraint imposes the isochoric component of a tensor such as the Cauchy stress on an undeformed sphere to be the zero tensor. The integration weights and corresponding directions for the 21-point numerical integration scheme are derived in [80].

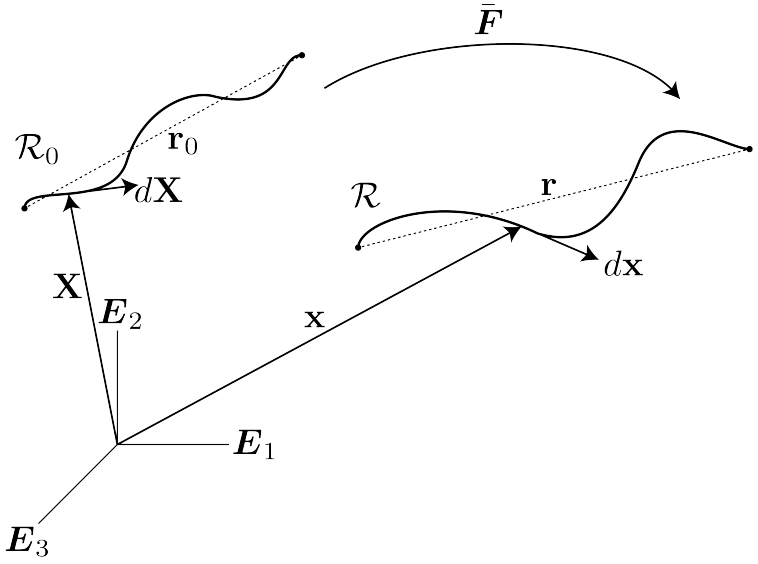

Figure 4.9: *Mapping of a worm-like chain from reference configuration to spatial configuration*

The elastic (equilibrium) and viscous (non-equilibrium) response is decoupled by assuming an additive decomposition of the Helmholtz free energy [81, 82, 83]

$$\Psi(\boldsymbol{C}, \boldsymbol{\Gamma}_1, ..., \boldsymbol{\Gamma}_m) = \Psi^{eq}(\boldsymbol{C}) + \sum_{i=1}^{m} \Psi_i^{neq}(\bar{\boldsymbol{C}}, \boldsymbol{\Gamma}_i)\,, \tag{4.12}$$

where m denotes the total number of non-equilibrium terms, and $\boldsymbol{\Gamma}_i$ is the vector of internal state variables corresponding to the i^{th} term. Assuming the decomposition of the deformation gradient in Equation (4.7), the equilibrium portion of the Helmholtz free energy is additively decomposed as

$$\Psi^{eq}(\boldsymbol{C}) = \Psi^{eq}_{sph}(J) + \Psi^{eq}_{iso}(\bar{\boldsymbol{C}})\,. \tag{4.13}$$

With this assumption, the second Piola-Kirchhoff stress tensor $\boldsymbol{S}$ is determined from the derivative of the Helmholtz free energy with respect to the right Cauchy-Green tensor $\boldsymbol{C}$ and is thus additively decomposed in the same manner

$$\boldsymbol{S} = 2\frac{\partial \Psi}{\partial \boldsymbol{C}} = \boldsymbol{S}^{eq} + \boldsymbol{S}^{neq}\,, \tag{4.14}$$

with

$$\begin{aligned} \boldsymbol{S}^{eq} &= 2\frac{\partial \Psi^{eq}}{\partial \boldsymbol{C}}\,, \\ \boldsymbol{S}^{neq} &= 2\frac{\partial \Psi^{neq}}{\partial \boldsymbol{C}}\,. \end{aligned} \tag{4.15}$$

The non-equilibrium portion of the stress is defined in terms of the "fictitious" stress of each term $\boldsymbol{Q}_i$ as

$$\boldsymbol{S}^{neq} = \sum_{i=1}^{m} \boldsymbol{Q}_i, \quad \boldsymbol{Q}_i = 2J^{-2/3} Dev\left[\frac{\partial \Psi_i^{neq}}{\partial \bar{\boldsymbol{C}}}\right]. \tag{4.16}$$

The equilibrium portion is likewise split into isochoric and spherical components

$$\boldsymbol{S}^{eq} = \boldsymbol{S}^{eq}_{sph} + \boldsymbol{S}^{eq}_{iso}\,, \tag{4.17}$$

with

$$\begin{aligned} \boldsymbol{S}^{eq}_{sph} &= J\frac{d\Psi^{eq}_{sph}}{dJ}\boldsymbol{C}^{-1}\,, \\ \boldsymbol{S}^{eq}_{iso} &= 2J^{-2/3} Dev\left[\frac{d\Psi^{eq}_{iso}}{d\bar{\boldsymbol{C}}}\right], \end{aligned} \tag{4.18}$$

where Dev$(\cdot)$ is the deviatoric projection of a given tensor. With the assumption that all processes remain isothermal, the Clausius-Planck inequality is expressed in point-wise form as

$$\frac{1}{2}\boldsymbol{S} \cdot \dot{\boldsymbol{C}} - \dot{\Psi} \geq 0\,, \tag{4.19}$$

where the dot over any symbol denotes the material time derivative. Expanding the time derivative

of the second term using chain rule, Equation (4.19) becomes

$$\frac{1}{2}\left[\boldsymbol{S} - 2\frac{\partial \Psi}{\partial \boldsymbol{C}}\right] \cdot \dot{\boldsymbol{C}} - \mathcal{D}_{int} \geq 0\,, \tag{4.20}$$

where the internal dissipation is defined in terms of the vector of state variables $\boldsymbol{\Gamma}$ as

$$\mathcal{D}_{int} = \sum_{i=1}^{m} \frac{\partial \Psi^{neq}}{\partial \boldsymbol{\Gamma}_i} \cdot \dot{\boldsymbol{\Gamma}}_i\,. \tag{4.21}$$

A material is defined to be viscoelastic if it is derived from the potential in Equation (4.12) and has a vanishing non-equilibrium Helmholtz free energy and stress (Ψ^{neq} and $\boldsymbol{S}^{neq}$, respectively) for all equilibrium states. In addition, a material complies with the Second Law of Thermodynamics if it unconditionally satisfies the inequality in Equation (4.20).

The transient evolution of the fictitious non-equilibrium stresses $\boldsymbol{Q}_i$ are assumed to be the linear ordinary differential equations postulated in [82, 81], which take the following form for the i^{th} non-equilibrium term:

$$\dot{\boldsymbol{Q}}_i + \frac{\boldsymbol{Q}_i}{\tau_i} = \theta_i \dot{\boldsymbol{S}}^{eq}_{iso}\,, \tag{4.22}$$

where τ_i is the relaxation time and θ_i is a free energy parameter that relates to the relaxation time [37]. As highlighted in [82], the evolution of the non-equilibrium stress prescribed by Equation (4.22) has several advantages:

1. Evolution equation is directly derived from the equivalent form used for infinitesimal kinematics and hence can be interpreted through a spring-dashpot model.

2. Incremental objectivity is trivially satisfied since stress evolution is prescribed in the reference configuration.

3. Linearity of the time-dependent terms allows to express the non-equilibrium stresses in convolution form.

4. Ensures a symmetric non-equilibrium tangent, since it derives directly from the form of the isochoric stress.

5. Reduces to traditional finite deformation elasticity when rates approach zero (equilibrium process).

The linearity of $\boldsymbol{Q}$ in time as shown in Equation (4.22) inherently assumes that the fictitious stresses remain close to thermal equilibrium. Moreover, it is assumed that the stresses and deformations computed according to Equation (4.22) comply with the positive dissipation inequality shown in Equation (4.22), though no rigorous proof of this assertion exists within the context of finite deformation [84]. The notion of non-equilibrium processes derived through a viscoelastic potential of the same form as Equation (4.12) was examined in [83], where a quadratic evolution law was postulated that sufficiently satisfies the positive dissipation inequality of Equation (4.20)

while reducing to linear evolution laws similar to the form of Equation (4.22) for deformations near thermal equilibrium. Although not implemented herein, nonlinear evolution laws such as the one proposed in [83] could be of importance in capturing the dynamics of cell migration, and thus, is a potential topic for future work.

The isochoric equilibrium portion of the Helmholtz free energy, Ψ_{iso}^{eq}, is directly related to the free energy of the individual filament ψ,

$$\Psi_{iso}^{eq} = n\psi(\lambda)\,, \tag{4.23}$$

where n is the filament density. Assuming that the filament end-to-end distance r is work-conjugate to the filament force f,

$$f = \frac{d\psi}{dr}\,, \tag{4.24}$$

and hence, through chain-rule,

$$\frac{d\psi}{d\lambda} = \psi' = r_0\lambda_0 f\ . \tag{4.25}$$

With the relation in Equation (4.25), $\boldsymbol{S}_{iso}^{eq}$ corresponding to the macroscale stresses can be determined based on the microscale filament force f,

$$\boldsymbol{S}_{iso}^{eq} = Dev[\tilde{\boldsymbol{S}}]\,, \tag{4.26}$$

where

$$\tilde{\boldsymbol{S}} = J^{-2/3} n r_0 \lambda_0 \lambda^{1-p} f\ \langle \bar{\lambda}^{p-2} \boldsymbol{t} \otimes \boldsymbol{t} \rangle\,, \tag{4.27}$$

and $\boldsymbol{t}$ is an undeformed unit vector as defined in Equation (4.11). Assuming the material is quasi-incompressible, the constraint $J = 1$ is enforced using a spherical Helmholtz free energy of the following form

$$\Psi_{sph}^{eq} = \frac{1}{2}\Lambda(J^2 - 1 - 2ln\ J)\,, \tag{4.28}$$

hence leading to the following definition of the spherical stress

$$\boldsymbol{S}_{sph}^{eq} = \frac{1}{2}\Lambda(J^2 - 1)\boldsymbol{C}^{-1}\,, \tag{4.29}$$

where Λ is a user-specified penalty parameter.

To obtain the update relation for the fictitious stress, both sides of Equation (4.22) can be multiplied by $exp(t/\tau_i)$, thus resulting in

$$\frac{d}{dt}\left\{ exp\left[\frac{t}{\tau_i}\boldsymbol{Q}_i\right]\right\} = exp\left[\frac{t}{\tau_i}\right]\theta_i \dot{\boldsymbol{S}}_{iso}^{eq}\ . \tag{4.30}$$

Here, the product rule was used to simplify the terms on the left-hand side. For a given time t_{n+1} and time increment $\Delta t_{n+1} = t_{n+1} - t_n$, the current value of the fictitious stress $\boldsymbol{Q}_{i,n+1}$ can be

represented in terms of the stress at t_n by integrating both sides of Equation (4.30) from t_n to t_{n+1}:

$$exp\left[\frac{t_{n+1}}{\tau_i}\right]\boldsymbol{Q}_{i,n+1} = exp\left[\frac{t_n}{\tau_i}\right]\boldsymbol{Q}_{i,n} + \int_{t_n}^{t_{n+1}} exp\left[\frac{t}{\tau_i}\right]\theta_i\dot{\boldsymbol{S}}^{eq}_{iso}\,dt\ . \tag{4.31}$$

Upon employing the midpoint rule to approximate the integral in Equation (4.31) and re-arranging terms, the update equation for the fictitious stress at t_{n+1} is expressed as

$$\boldsymbol{Q}_{i,n+1} = \boldsymbol{H}_{i,n} + \theta_i exp\left[-\frac{\Delta t_{n+1}}{2\tau_i}\right]\boldsymbol{S}^{eq}_{iso,n+1}\,, \tag{4.32}$$

where the history term is defined as

$$\boldsymbol{H}_{i,n} = exp\left[-\frac{\Delta t_{n+1}}{2\tau_i}\right]\left\{exp\left[-\frac{\Delta t_{n+1}}{2\tau_i}\right]\boldsymbol{Q}_{i,n} - \theta_i\boldsymbol{S}^{eq}_{iso,n}\right\}. \tag{4.33}$$

The tangent in the reference configuration is

$$\mathbb{C}_{n+1} = \mathbb{C}^{eq}_{sph,n+1} + \left\{1 + \sum_{i=1}^{m}\theta_i exp\left[-\frac{\Delta t_{n+1}}{2\tau_i}\right]\right\}\mathbb{C}^{eq}_{iso,n+1}\,, \tag{4.34}$$

where

$$\begin{aligned}\mathbb{C}^{eq}_{sph} &= \Lambda J^2\boldsymbol{C}^{-1}\otimes\boldsymbol{C}^{-1} - \Lambda(J^2-1)\boldsymbol{C}^{-1}\odot\boldsymbol{C}^{-1}\,,\\ \mathbb{C}^{eq}_{iso} &= J^{-4/3}Dev[\tilde{\mathbb{C}}] + \frac{2}{3}J^{-2/3}Tr\tilde{\boldsymbol{S}}\,\hat{\mathbb{P}} - \frac{2}{3}\left(\boldsymbol{C}^{-1}\otimes\boldsymbol{S}^{eq}_{iso} + \boldsymbol{S}^{eq}_{iso}\otimes\boldsymbol{C}^{-1}\right).\end{aligned} \tag{4.35}$$

The fourth order tensor $\boldsymbol{C}^{-1}\odot\boldsymbol{C}^{-1}$ is defined in components as

$$\left(\boldsymbol{C}^{-1}\odot\boldsymbol{C}^{-1}\right)_{ABCD} = \left(C^{-1}_{AC}C^{-1}_{BD} + C^{-1}_{AD}C^{-1}_{BC}\right). \tag{4.36}$$

The fourth order tensors $\tilde{\mathbb{C}}$ and $\hat{\mathbb{P}}$ are defined, respectively, as

$$\begin{aligned}\tilde{\mathbb{C}} =& \left[\psi'' n\lambda^{2(1-p)} - \psi'(p-1)n\lambda^{1-2p}\right]\langle\bar{\lambda}^{p-2}\boldsymbol{t}\otimes\boldsymbol{t}\rangle\otimes\langle\bar{\lambda}^{p-2}\boldsymbol{t}\otimes\boldsymbol{t}\rangle\\ &+ (p-2)n\psi'\lambda^{1-p}\langle\bar{\lambda}^{p-4}\boldsymbol{t}\otimes\boldsymbol{t}\otimes\boldsymbol{t}\otimes\boldsymbol{t}\rangle\,,\end{aligned} \tag{4.37}$$

and

$$\hat{\mathbb{P}} = \boldsymbol{C}^{-1}\odot\boldsymbol{C}^{-1} - \frac{1}{3}\left(\boldsymbol{C}^{-1}\otimes\boldsymbol{C}^{-1}\right). \tag{4.38}$$

Lastly, the material tangent $\mathbb{C}$ can be pushed forward to the spatial configuration as follows

$$\mathbb{c} = \frac{1}{J}(\boldsymbol{F}\otimes\boldsymbol{F}\otimes\boldsymbol{F}\otimes\boldsymbol{F})\cdot\mathbb{C}\,, \tag{4.39}$$

where the symbol $(\cdot)$ represents the contraction operation which maps a fourth-order material tensor to a fourth-order spatial tensor.

4.4.3 Viscoelasticity of Actin Networks Undergoing Oscillatory Loading

Amplitude and frequency sweep experiments are commonly used to determine the time and length scales dominating the viscoelastic response of *in vitro* actin networks [37, 85, 70]. These experiments typically apply a sinusoidal pure shear deformation to a macroscale actin network to measure loss and storage moduli associated with the offset between the applied strain and stress, as well as the relaxation times and viscosity coefficients that define transient evolution of the non-equilibrium stresses. In [37], the relaxation times τ_i, the free energy parameters θ_i, and the F-actin density n were fit to experimental data of amplitude and frequency sweeps for both one and three non-equilibrium terms. Under pure shear for a characteristic material point, the authors demonstrated reasonable accuracy of the storage and loss moduli as functions of frequency and amplitude. For the purposes of this work, it assumed that a single non-equilibrium term is used, with a relaxation time of 2 s and free energy parameter of 0.835, coinciding with the values obtained in [37].

Consider two types of actin: long filaments with low F-actin concentration (cases (a) and (b) for high and low amplitude shear, respectively), and short filaments with high F-actin concentration (cases (c) and (d) for high and low amplitude shear, respectively), as summarized in Table 4.3. The parameters for cases (a) and (b) are taken from experiments of *in vitro* actin and the corresponding data fits in [36] with an averaging parameter $p = 13.12$, as computed in [37]. Cases (c) and (d) use typical actin lengths and concentrations observed along the leading edge of the lamellipodium, based on [48, 86]. The F-actin density is computed using [36, Equation 51] with an F-actin concentration of $500\mu M$ of F-actin [86]. In addition, the averaging parameter is assumed to be 13.12, as was used in cases (a) and (b). For comparison, the unstressed end-to-end distance of the short filament actin network is selected as 97.5% of the full contour length, which is higher than the 95% assumed for cases (a) and (b).

The actin network in cases (a)-(d) is modeled using a single four-node quadrilateral element with a time step of 0.01 s and an imposed pure shear, leading to a point-wise deformation gradient of the form

$$\left[\boldsymbol{F}\right] = \begin{bmatrix} 1 & \gamma & 0 \\ 0 & 1 & 0 \\ 0 & 0 & 1 \end{bmatrix} sin(\omega t) \; . \tag{4.40}$$

The maximum amplitude of the shear deformation, γ, is chosen as 3% for cases (b) and (d), and 12% for cases (a) and (c). The angular frequency, ω, is $\pi/10$ for all cases. With these selections, case (a) precisely matches the numerical validation of the experimental results (both conducted in [37]), hence serving as a verification of algorithmic consistency for the present work. Inertia is neglected in the present setting, hence limiting the transient response to the viscoelasticity of the material. Additionally, it is assumed that the out-of-plane thickness of actin networks is generally small compared to the in-plane dimensions, as observed in lamellipodial actin networks [87, 46]. Based on these observations, the out-of-plane shear and normal stresses are approximately zero, which is enforced through the iterative procedure highlighted in [88, Chapter 6], [89]. The enforcement

of plane stress enables out-of-plane deformation, thus preventing an over-constrained system of equations which leads to element locking [90, Chapter 4].

Case	Shear Strain amplitude	Density ($1/\mu m^3$)	Length (μm)	Unstressed end-to-end distance (μm)
(a)	0.12	14.31	1.048	1.0
(b)	0.03	14.31	1.048	1.0
(c)	0.12	4000.0	0.20	0.195
(d)	0.03	4000.0	0.20	0.195

Table 4.3: *Parameters for shear stress/strain cases*

Based on the selected parameters in Table 4.3, the viscoelastic response of the actin network is significantly affected by the internal structure defined by the filament length and F-actin concentration, as well as the external loading, as shown in Figures 4.10 and 4.11. Under 3% shear deformation (denoted as γ), the shear stress-strain curve (also termed Lissajous curve) shown in Figures 4.11b and 4.11d indicates that both the long-length low-density and the short-length high-density actin networks exhibit elliptical hysteresis profiles typical of small deformation viscoelasticity. As a result, the time evolution of the in-plane shear stress component T_{xy} of the Cauchy stress maintains a sinusoidal profile similar to the applied shear deformation, γ. In contrast, an applied shear deformation of 12% generates shear stress that follows a perturbed sinusoidal time evolution, as highlighted in Figures 4.10a and 4.10c. The corresponding Lissajous curves in Figures 4.11a and 4.11c exhibit a sharp rise in slope starting near 10% strains due to the entropic effects of filament stretching discussed in Section 4.4.1. In both the 3% and 12% maximum shear strain amplitude loading, the short-length high-density actin network produces stresses that are several orders of magnitude higher than the long-length low-density actin network. This magnification in stresses arises as a result of the higher filament density, which is linearly proportional to the Helmholtz free energy, and hence, the stresses.

4.5 Cell Collisions

4.5.1 Motivation

Contact inhibition of locomotion (CIL) is the general phenomenon in which intercellular interactions lead to an apparent change in migration velocity of individual as well as collective groups of cells [91, 92, 93]. The proper efficiency of cells undergoing CIL is a strong indicator of healthy tissues. Moreover, identifying cells that exhibit irregular CIL aids in the detection of cancer metastasis [92]. These interactions consist of cells colliding onto one another, and subsequently adhering and/or re-orienting upon contact [92]. The molecular mechanisms leading to cell separation and re-orientation upon contact is not entirely known. In [92], the authors hypothesize that separation can be initiated by a combination of internalized disassembly and/or rupture of cell-cell adhesions,

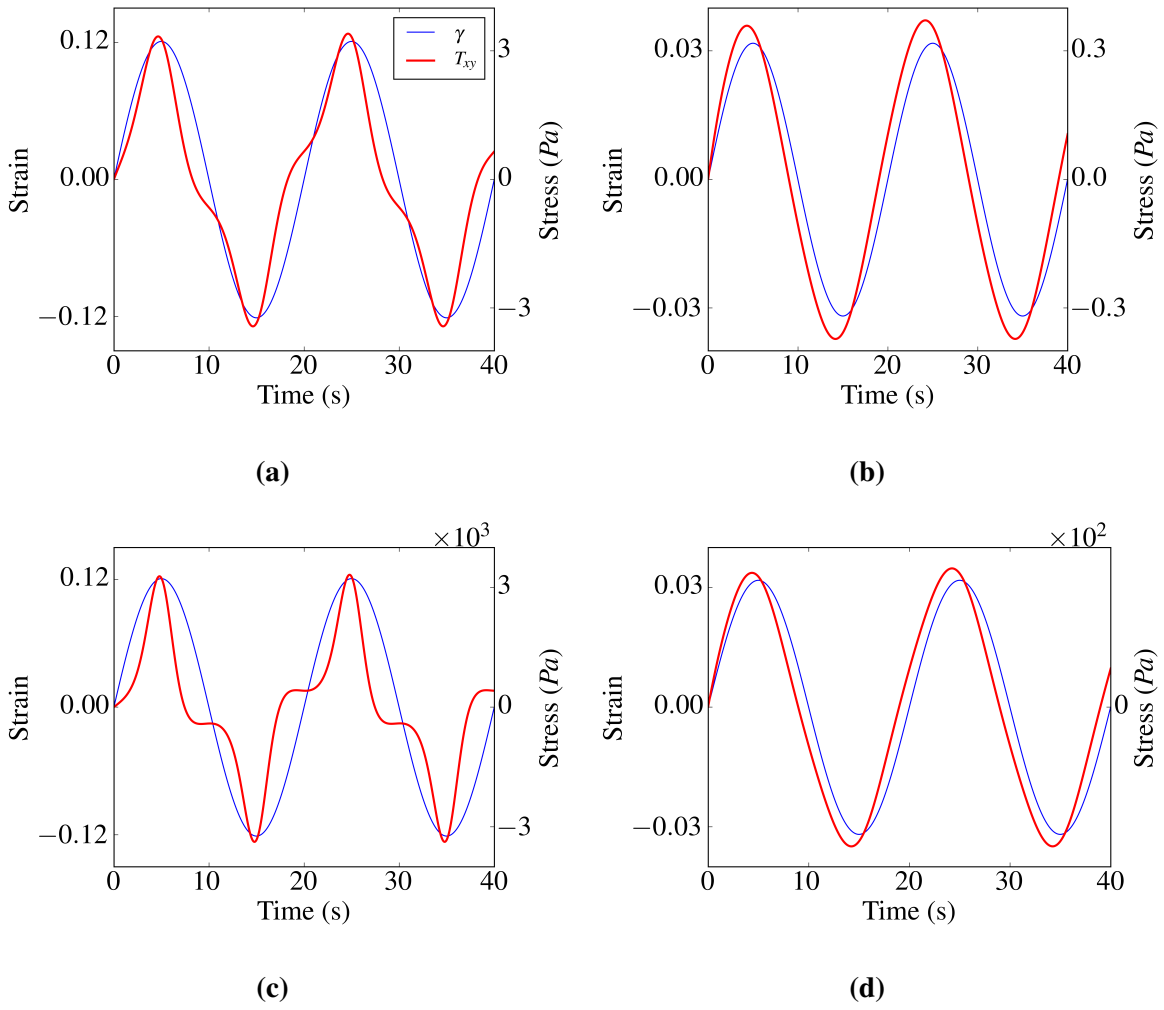

Figure 4.10: *Comparison of shear stress and strain evolution for cases (a)-(d) shown in Table 4.3*

and simultaneous re-orientation of the leading edge thus forming new protrusions in a direction where the cell is free to migrate. Various simulations have been conducted in recent years that focus on the overall shape and motion of cells undergoing binary contact (single collision of two cells) as well as interactions among clusters of cells [94, 95]. This section focuses on the treadmilling of a single cell subject to external barriers, with a mechanically-driven re-orientation of its protruding edge. A surface growth/resorption law is introduced in Section 4.5.2 to relate the change in treadmilling direction to the contact forces. Simulation of a simple cell migrating, encountering external barriers, and re-orienting its growth is presented in Section 4.5.3.

4.5.2 Surface Growth Law for Colliding Cell

The surface growth/resorption law is based on the GRE model, which assumes that the body grows and ablates without changing shape, as described in Section 4.3. The growth/resorption can thus

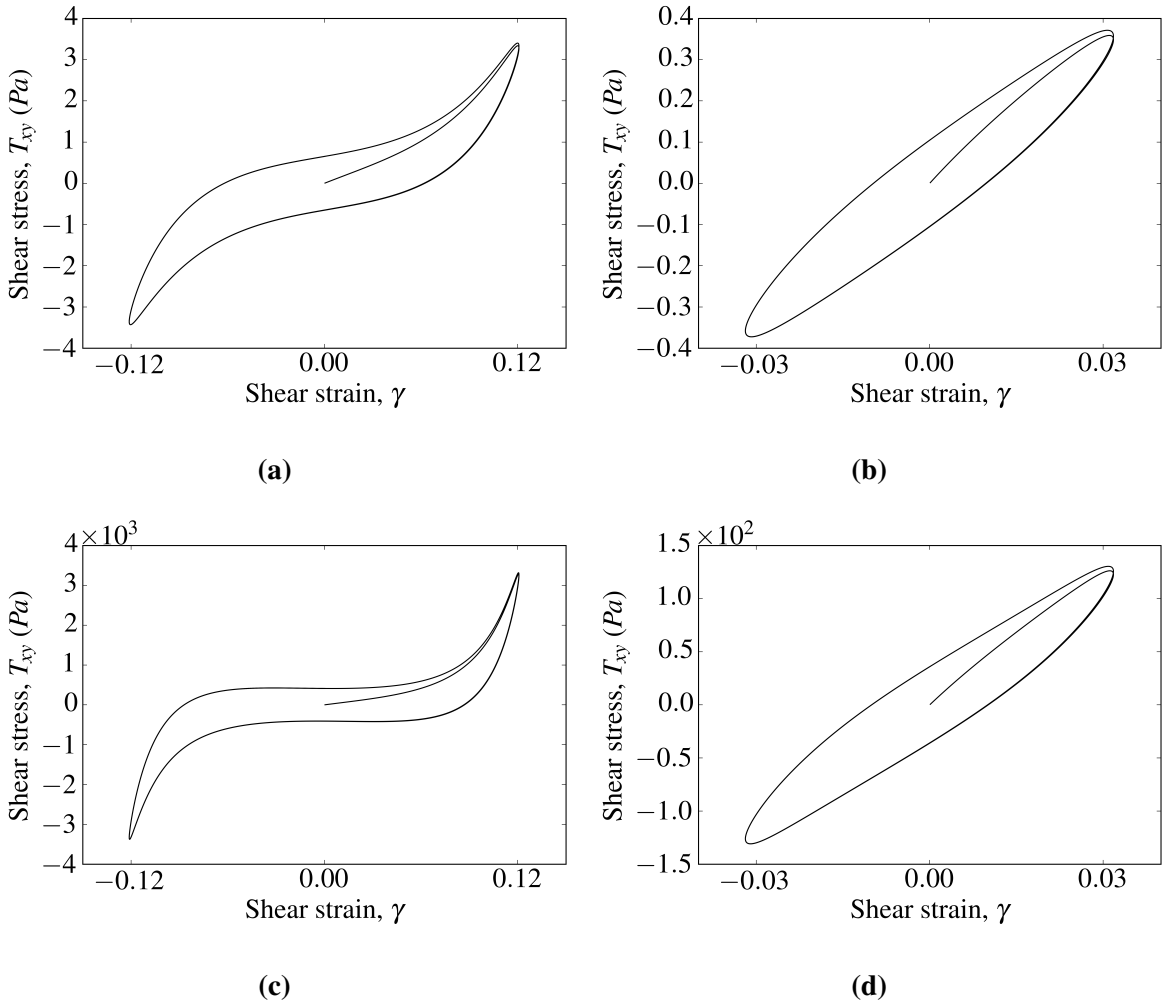

Figure 4.11: *Comparison of Lissajous curves for cases (a)-(d) shown in Table 4.3*

be characterized by a spatially constant treadmilling velocity $\boldsymbol{V}$, with a time-dependent evolution of the following form

$$\frac{d}{dt}\left(\bar{m}\mathbf{V}\right) = \alpha(||\boldsymbol{t}_c||, t)\frac{\boldsymbol{t}_c}{||\boldsymbol{t}_c||}\,, \tag{4.41}$$

$$\bar{m} = \int_{\partial\tilde{\mathcal{R}}} \rho_s \, da\,. \tag{4.42}$$

In Equations (4.41) and (4.42), ρ_s is the surface density defined on $\partial\tilde{\mathcal{R}}$, $\bar{m}$ is the total surface mass, α is a user-specified function of the magnitude of the contact force $||\boldsymbol{t}_c||$ and time t, and $\boldsymbol{t}_c$ is the net contact force in the intermediate configuration defined as

$$\boldsymbol{t}_c = \int_{\partial\tilde{\mathcal{R}}} \boldsymbol{t} \, da\,. \tag{4.43}$$

It is convenient to assume that the surface density on the boundary $\partial\tilde{\mathcal{R}}$ is directly related to the mass density ρ through the following relation:

$$\rho_s = \rho\, l_g\,, \tag{4.44}$$

where l_g is an assumed parameter which represents the average thickness of growth increments.

Each side of Equation (4.41) has units of force. The factor α modulates the sensitivity of the overall treadmilling velocity to external forces. For instance, a high value of α would suggest a rapid re-orienting of the treadmilling velocity away from the contact surface whereas a low α can generate a prolonged deceleration upon contact. This concept of interdependency between forces and surface growth/resorption was studied in prior works such as [24, 25, 3, 26]. In these works, the concept of configurational forces was applied to surface growth/resorption phenomenon to characterize the non-material motion of the surface in terms of changes in free energy of the body, and hence, to mechanical forces. In the present context, it is assumed that the physical laws governing individual mechanisms that lead to the change in treadmilling velocity are not explicitly solved for. As a consequence, the growth/resorption velocity governed by Equation (4.41) is purely phenomenological.

The relation shown in Equation (4.41) is invariant under Galilean transformations $\tilde{\boldsymbol{\chi}}^+$ of the form

$$\tilde{\mathbf{x}}^+ = \boldsymbol{c}(t) + \boldsymbol{Q}\bar{\tilde{\mathbf{x}}}\,, \tag{4.45}$$

where $\boldsymbol{c}(t)$ defines a constant translational velocity $\boldsymbol{c} = \mathbf{v}_0 t$, $\boldsymbol{Q}$ is a time-independent proper orthogonal rotation in the intermediate configuration, and $\bar{\tilde{\mathbf{x}}}$ is a point traveling with velocity $\boldsymbol{V}$. The force per length given by the relation in Equation (4.41) from a reference frame of an observer undergoing a motion $\tilde{\boldsymbol{\chi}}^+$ is

$$\frac{d}{dt}\left(\bar{m}^+\frac{d\tilde{\boldsymbol{\chi}}^+}{dt}\right) = \alpha^+(||\boldsymbol{t}_c^+||, t)\frac{\boldsymbol{t}_c^+}{||\boldsymbol{t}_c^+||}\,. \tag{4.46}$$

The treadmilling velocity $\boldsymbol{V}$ and average contact force $\boldsymbol{t}_c$, and the scalars $\bar{m}$ and α are assumed to transform as $\boldsymbol{V}^+ = \boldsymbol{Q}\boldsymbol{V}$, $\boldsymbol{t}_c^+ = \boldsymbol{Q}\boldsymbol{t}_c$, $\alpha^+ = \alpha$, and $\bar{m}^+ = \bar{m}$, respectively. Evaluating the time derivatives, the left-hand side of Equation (4.46) simplifies to

$$\begin{aligned}\frac{d}{dt}\left(\bar{m}^+\frac{d\tilde{\boldsymbol{\chi}}^+}{dt}\right) &= \frac{d}{dt}\left(\bar{m}^+(\mathbf{v}_0 + \boldsymbol{Q}\boldsymbol{V})\right)\\ &= \bar{m}^+\left(\boldsymbol{Q}\frac{d\boldsymbol{V}}{dt}\right) + \frac{d\bar{m}^+}{dt}(\boldsymbol{Q}\boldsymbol{V})\\ &= \frac{d}{dt}(\bar{m}^+\boldsymbol{V}^+)\,.\end{aligned} \tag{4.47}$$

Note that Equation (4.41) is not invariant for a general transformation where $\hat{\boldsymbol{Q}} = \boldsymbol{Q}(t)$ since the time derivative of $\tilde{\boldsymbol{\chi}}^+$ under such a transformation would contain the rotation rate term $d\hat{\boldsymbol{Q}}/dt$. In this case, the treadmilling velocity and its rate experienced from a reference frame of an inertial observer do not transform invariantly for any proper orthogonal rotation, *i.e.*, $\boldsymbol{V}^+ \neq \hat{\boldsymbol{Q}}\boldsymbol{V}$ and

$d\boldsymbol{V}^+/dt \neq \hat{\boldsymbol{Q}} d\boldsymbol{V}/dt$ for all $\hat{\boldsymbol{Q}}$.

4.5.3 Example of Cell Colliding with Multiple Barriers

The example presented here focuses on the effect of collision on a single cell's stresses and deformations within the cytoskeletal actin network, as well as the resulting re-orientation of the protruding edge. The hydrodynamics of the cytosol fluid and actin filaments, and interactions with the cell's external environment among which include extracellular adhesion and protein transport are not considered. In addition, the membrane is assumed to play a negligible role in the overall mechanical response of the cell, and is hence ignored. The constitutive model of individual filaments and the homogenized actin network reviewed in Sections 4.4.1 and 4.4.2 is used with parameter values listed in Table 4.2 and case (a) in Table 4.3. The cell is assumed to be in plane stress, as discussed in Section 4.4.3. The growth region is initially deformation-free and stress-free (both equilibrium and non-equilibrium stresses). As a consequence of the assumption of stress-free growth, newly accreted material has no initial displacements or accelerations. The contact of a single cell is enforced through a penalty-type formulation, with modifications for surface growth as described in Appendix A.6. The value of the penalty parameter is selected to be sufficiently low to reflect the finite stiffness of other cells. In this setting, the inexact contact constraint acts as a stiff Hookean spring by allowing a small amount of contact penetration to occur. Friction and adhesion between the cell, substrate, and contact surface is neglected for simplicity.

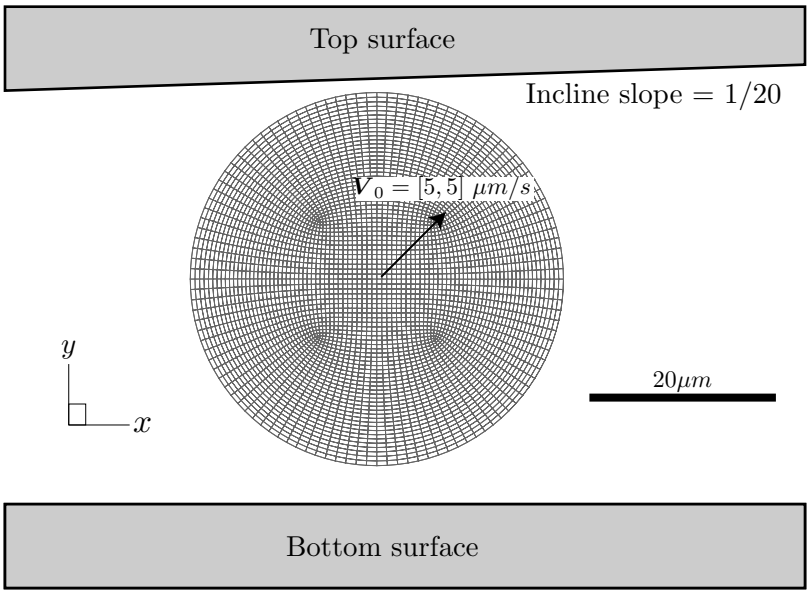

Figure 4.12: *Treadmilling and colliding cell: Initial configuration and discretized mesh*

The geometry used to simulate the migrating cell is a circle with a 20 μm radius, and initial coordinates of the center at the origin. The mesh consists of 4032 four-node bilinear quadrilateral elements. A nine-point Gauss-Lobatto quadrature rule is used, which contains sampling points on the corner nodes and mid-edges of each element. This ensures that the integration points along the

growth region will always capture the fields in the newly grown regions regardless of time step, as is described in Appendix A.5. Two barriers are placed, one inclined slightly above the initial position of the cell with a slope of $1/20$ and the other at a constant vertical height of -22 μm relative to the initial center of the domain. In the context of CIL, these barriers represent stationary clusters of cells pushing against the cell of interest when contact occurs. The initial configuration of the geometry, as well as the mesh and barrier locations, is shown in Figure 4.12. Other parameters are listed in Table 4.4.

Parameter name	**Value**
Initial treadmilling velocity	$[5,\ 5]$ $\mu m/s$
Initial material velocity	$[0,\ 0]$ $\mu m/s$
Initial density †	1.05 g/cm^3
Growth density	1.05 g/cm^3
α value	2.0e-10 μN
Average growth increment thickness, l_g	1.0μm
Maximum time step	5.0e-2 s
Minimum time step	5.0e-4 s
Incompressibility penalty parameter, Λ	1.0e-5 μPa
Contact penalty parameter, ϵ	5.0e-9 $\mu N/\mu m^3$

† Based on the evidence presented in [96], the density of typical cells is assumed to be approximately 5-10% higher than water.

Table 4.4: *Treadmilling and colliding cell: Model parameters for colliding cell example*

The simulation of the treadmilling cell was conducted for a total of 3.9 s. Three collision events occurred between the cell and the external barriers, with initial contact at approximately 0.67 s, 1.81 s, and 2.98 s, as schematically shown in Figure 4.13. The time-lapse of the cell as it treadmills and collides with external barriers is shown in Figure 4.14. The temporal evolution of the simulation step size, and the volume-averaged fields are shown in Figures 4.15 to 4.18. Upon first contact at approximately 0.67 s, both inertia and re-orientation of the surface growth and resorption leads to a change in apparent motion toward the lower barrier. Note that the release of the contact constraint generates transient oscillations in the acceleration, a classic feature inherent in the Newmark integration scheme [97]. During the second collision event, the re-orientation of cell's leading edge overcomes the effects of inertial impact and drives the cell away from the barrier. In this setting, the net surface growth/resorption direction is opposite of the material displacement and velocities between the second and third collision. The last contact event results in a net increase in the material velocity and incremental displacement as it is propelled away from the barrier by the final re-orientation of surface growth and resorption.

In contrast to elastic contact of non-growing bodies, the mechanisms driving accretion of new material can persist during contact. For instance, a plausible hypothesis to explain the separation of cells during CIL involves the continual polymerization of actin filaments along the contact interface which eventually leads to the re-orientation of the protruding edge [92]. In the current setting, material accretion at the contact point leads to larger penetration gaps due to the finite stiffness

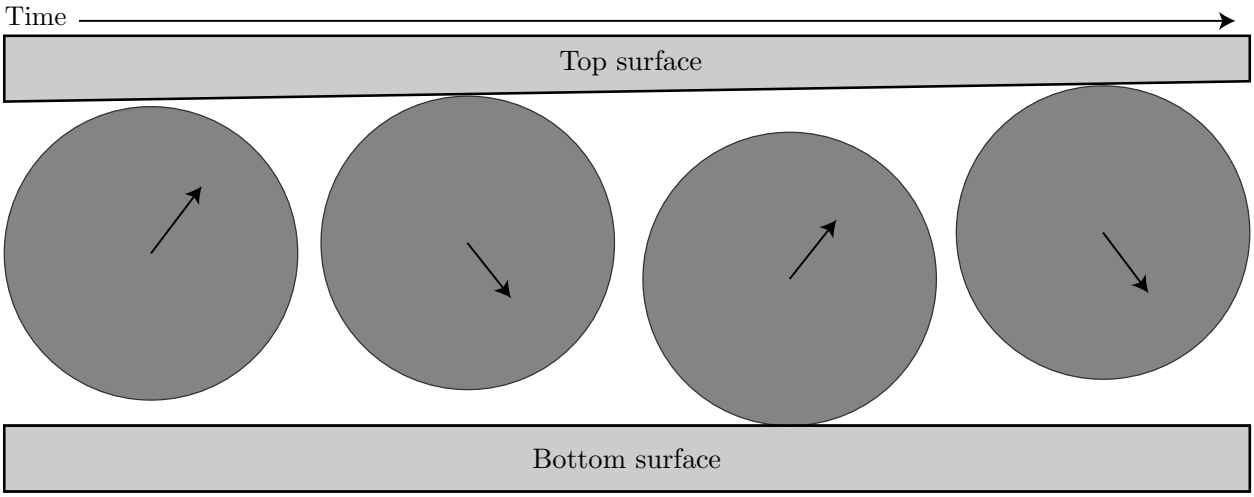

Figure 4.13: *Treadmilling and colliding cell: Schematic motion of treadmilling cell (horizontal scale is exaggerated for clarity). Arrows indicate direction of treadmilling velocity post-initial contact.*

of the barrier. This, in turn, produces higher reactionary tractions on the cell as it grows towards the barrier. The profiles in Figures 4.19 and 4.20 illustrate that both the von Mises stress and the absolute pressure near the contact point increase until this region switches from surface growth to resorption. Once the contact point resorpts away from the interface, the tractions decrease until the cell is no longer in contact with the barrier.

Upon re-orienting the surface of growth and resorption, discontinuities form in the acceleration field along the interface of the new leading edge, as shown in Figure 4.21. This phenomenon occurs due to the assumption that newly formed material does not inherit information about the acceleration of the prior existing material.[3] Since acceleration on either side of the interface is different, the inertial forces also differ. This mismatch thus generates transient stress concentrations in the absence of any applied loading, as illustrated in the bottom of Figure 4.21.

The overall deformation is small relative to the cell's full scale, which approximately maintains its initial shape even after multiple contact events. This result is in contrast to experimental observations such as those of [55], which point to significant changes in cell shape upon encountering an external barrier. A possible reason for this discrepancy is that the *in vitro* mechanics of actin networks that is used to represent the treadmilling cell in this dissertation is vastly different than that of *in vivo* cells due to numerous factors, among which include inhomogeneities of actin orientations, chemical reactions of various proteins, and spatial variation of filament lengths and densities [64, 71]. Although experiments of the mechanical behavior of *in vivo* actin networks are in their nascent phase, future breakthroughs may help improve the modeling of cell treadmilling.

[3]Discontinuities are also present in the gradient of the incremental displacement, which leads to discontinuous stresses as noted in Section 3.5.3 On the other hand, the material velocities do not inherit discontinuities, since accreted material has an initial motion which is identical to the existing material point nearest to it.

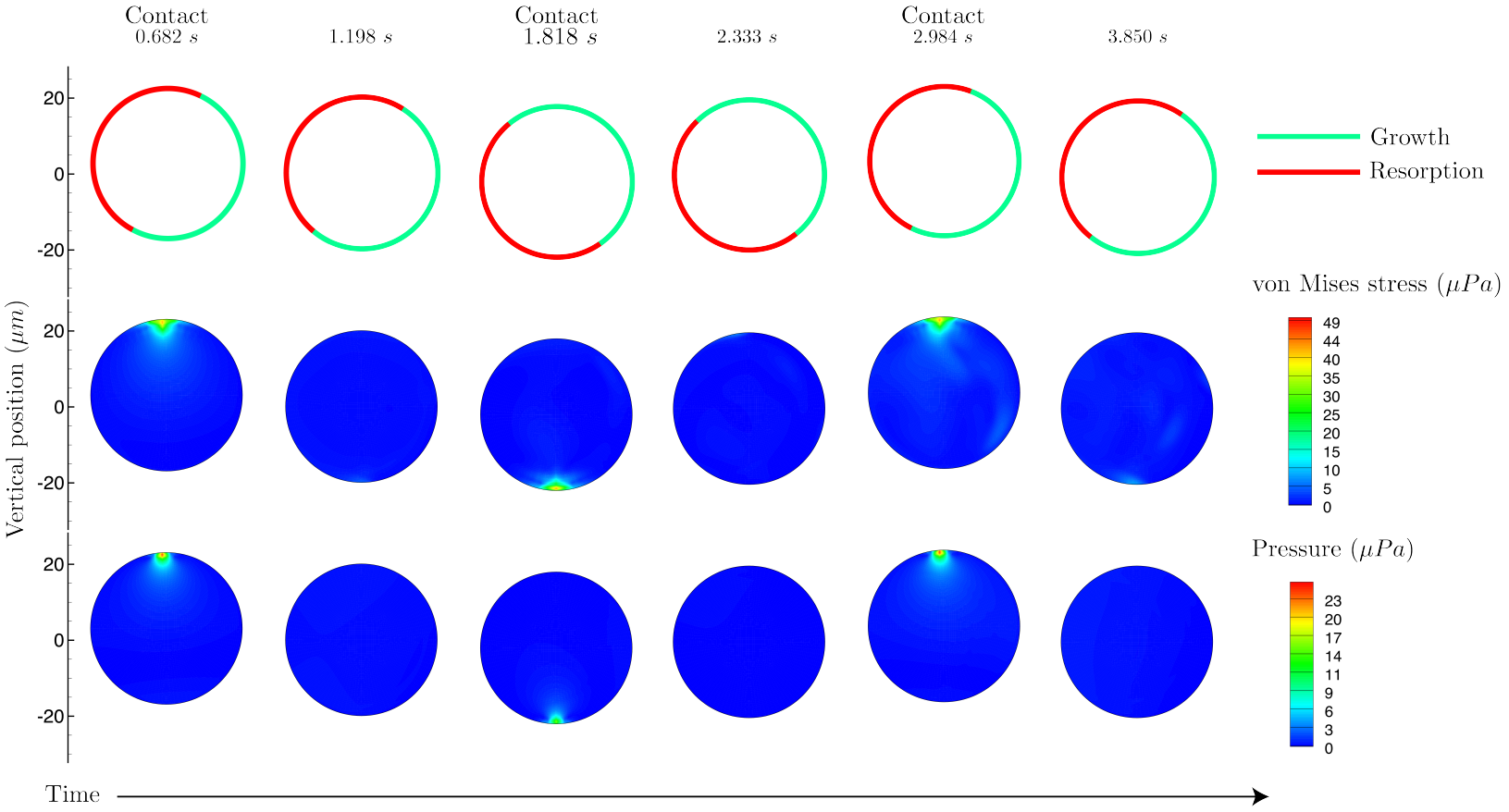

Figure 4.14: *Treadmilling and colliding cell: Time-lapse of regions of surface growth and resorption (top), von Mises stress (middle), and absolute pressure (bottom) for cell undergoing three collisions*

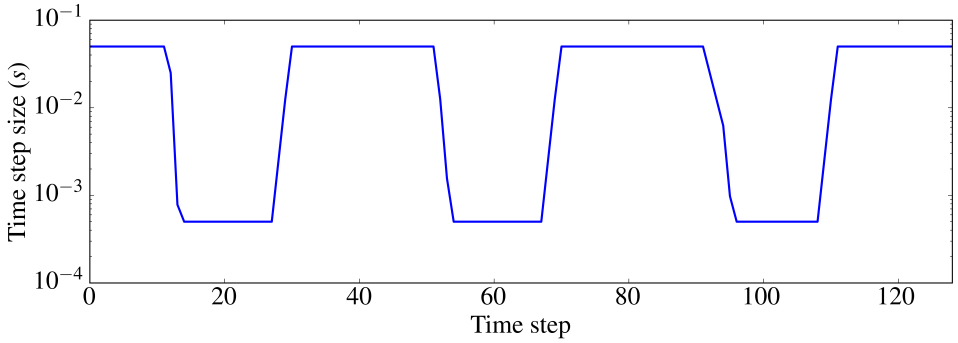

Figure 4.15: *Treadmilling and colliding cell: Time step evolution*

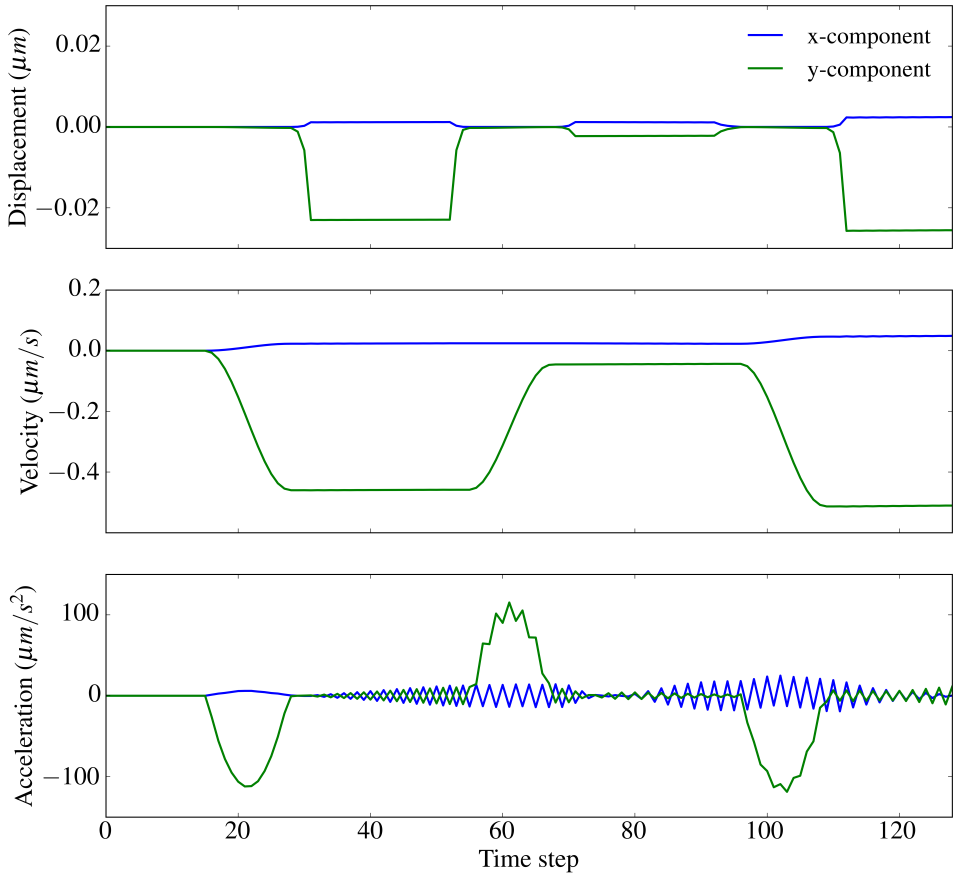

Figure 4.16: *Treadmilling and colliding cell: Evolution of average incremental material displacement (top), average material velocity (middle), and average material acceleration (bottom)*

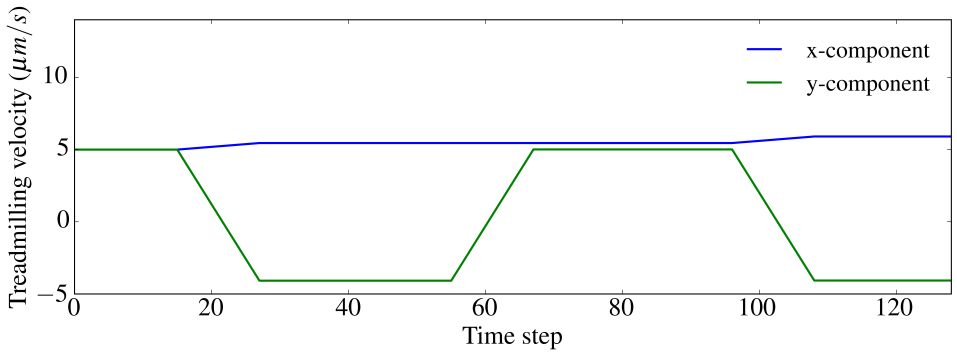

Figure 4.17: *Treadmilling and colliding cell: Evolution of treadmilling velocity*

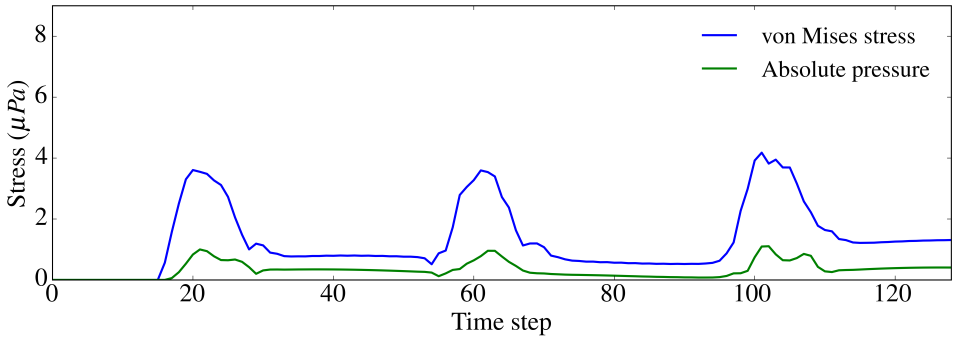

Figure 4.18: *Treadmilling and colliding cell: Evolution of average von Mises stress (top) and average absolute pressure (bottom)*

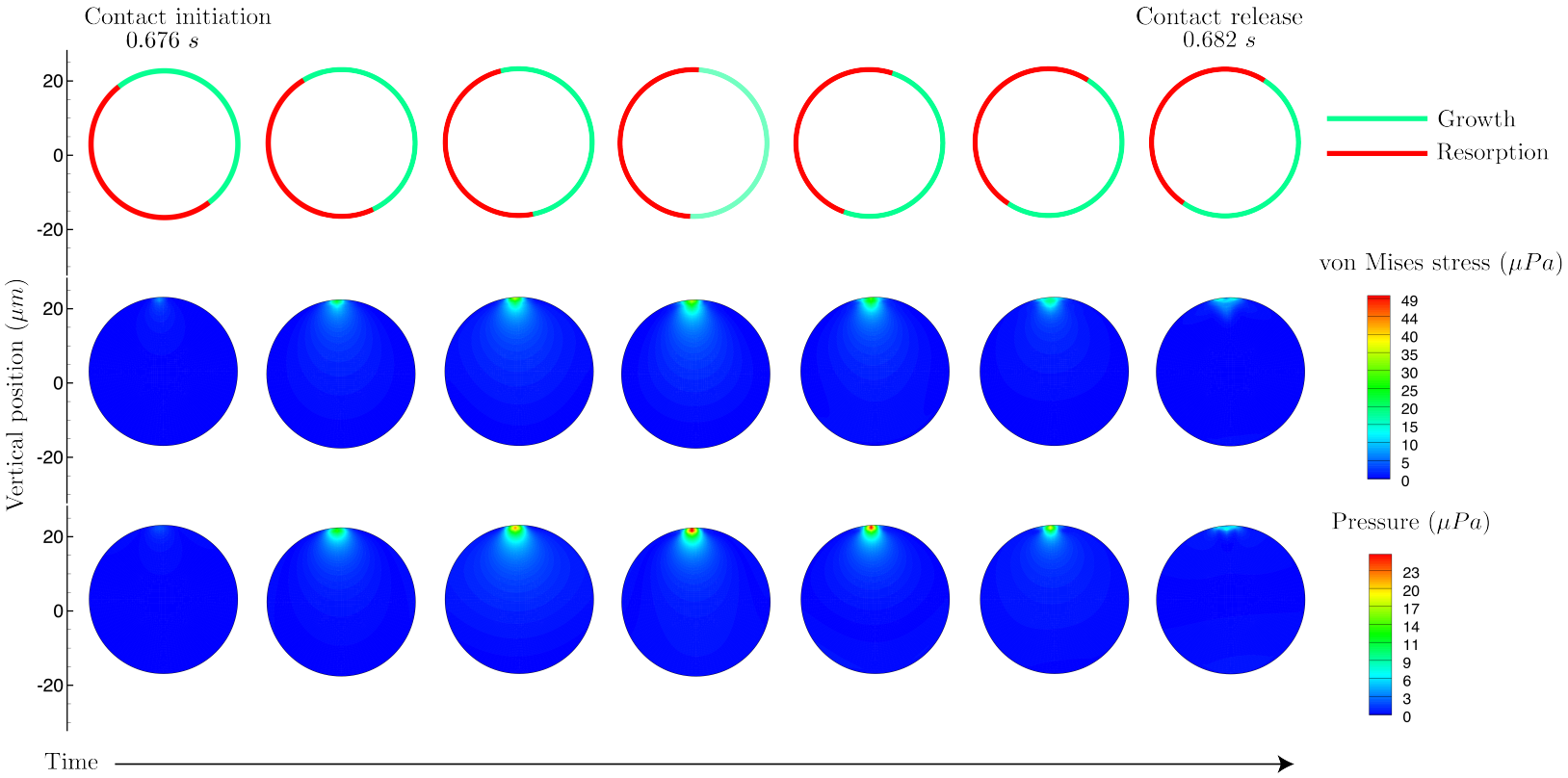

Figure 4.19: *Treadmilling and colliding cell: Time-lapse of regions of surface growth and resorption (top), von Mises stress (middle), and pressure (bottom) during first cell-barrier collision*

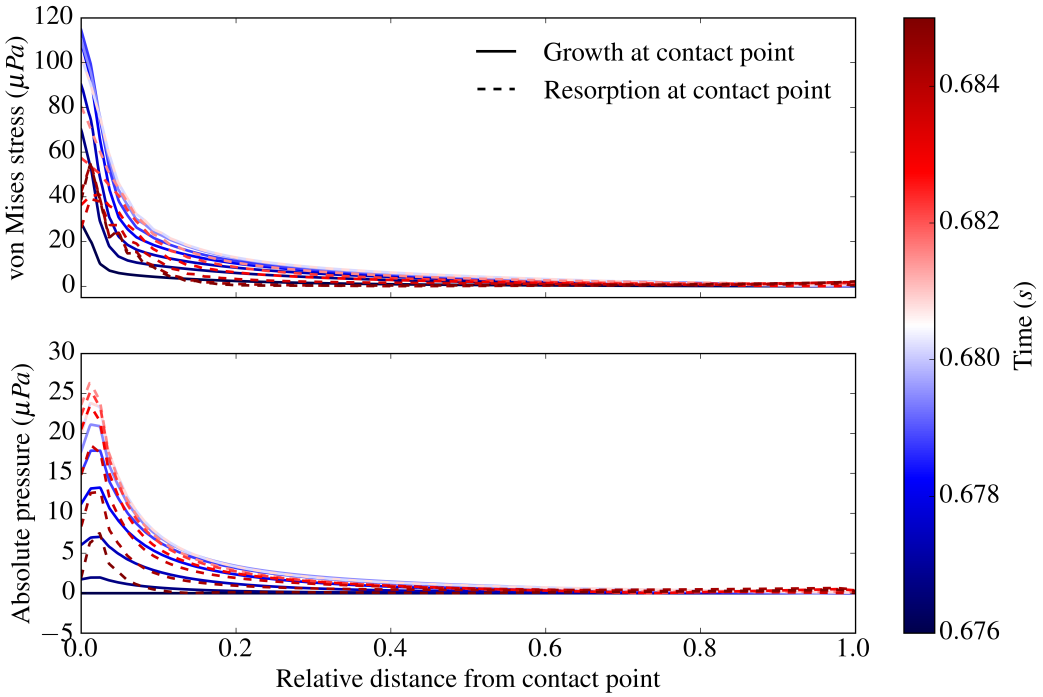

Figure 4.20: *Treadmilling and colliding cell: von Mises stress (top) and pressure (bottom) profiles taken along cross-section of cell orthogonal to contact surface during first cell-barrier collision*

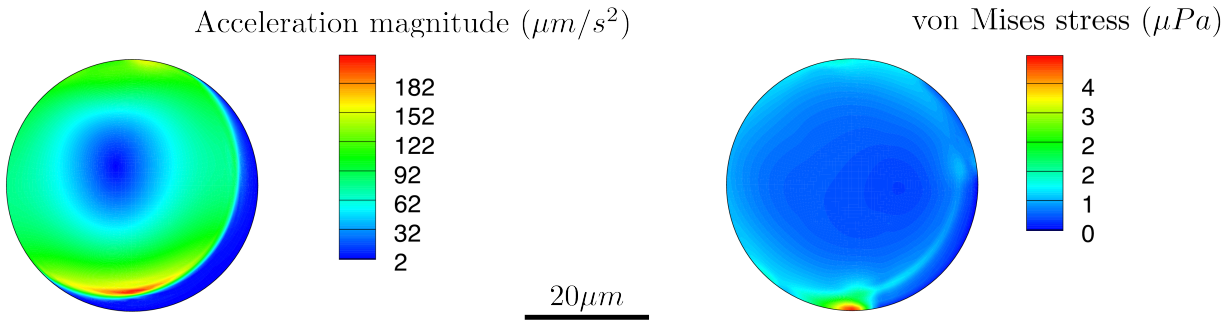

Figure 4.21: *Treadmilling and colliding cell: Acceleration magnitude (top) and von Mises stress (bottom) at the time $t = 1.198$ s during cell treadmilling after the first collision*

4.6 Concluding Remarks

In this chapter, the process of cell migration within the context of surface growth and resorption was introduced. The dynamics and kinetics of actin filaments and its correlation to the protrusion of the cell's leading edge was described. An example was provided which formulated a surface growth law relating the concentration of G-actin monomers to the cell-scale apparent treadmilling speed. In this example, it was shown that the magnitude of the steady-state cell treadmilling velocity was higher for an assumed cell cytoskeleton geometry that consisted of a flatter (lower absolute curvature) leading edge of the lamellipodium.

The second part of the chapter focused on the relation between cell migration and the stress fields within the cytoskeleton. A viscoelastic constitutive law for a continuum-level isotropic actin network based on the works of [36, 37] was reviewed. In addition, the fundamental properties of this constitutive law and their effect on the force experienced by individual filaments as well as the macro-scale stress and strain of the actin network were highlighted. An example consisting of an idealized migrating cell that encounters external barriers was presented. In this example, a traction-based growth law was introduced to account for the change and re-orientation of the cell treadmilling velocity occurring during cell-barrier contact. Simulation results illustrated that the evolution of the material fields along the contact interface depend on the surface growth/resorption velocity and its rate of change in both direction and magnitude.

Chapter 5

Conclusion

5.1 Closing Remarks

In this dissertation, a new approach to representing and simulating surface growth/resorption of deformable bodies is presented. A brief summary of contributions of the current work is listed below:

- **Physical description of a deforming body undergoing surface growth/resorption**
  - The total motion of the body is characterized in terms of a non-material surface growth/resorption transformation χ_g which defines the new interface of the body, the mapping $\overline{\chi}_g$ which maps material from its initial location and time of existence to the intermediate configuration, and the deformation mapping χ_d which describes the motion of material points relative to the intermediate configuration.
  - The global balance laws and their local equivalents are posed with respect to the current configuration, with the assumption that newly accreted regions attach to the prior existing material in an initially stress-free state.
- **Numerical algorithm**
  - Discretized weak forms are solved on a non-material mesh which convects based on the surface growth/resorption velocities. With this strategy, the fields at a given node or element is based on its spatial location rather than a fixed material point or region. Therefore, the general form of the proposed algorithm provides a framework that can be used to model a deformable body undergoing any arbitrary two-dimensional surface growth/resorption motion with either a fixed-connectivity mesh (as done in this work), or with an adaptively evolving mesh.
- **Applications of surface growth/resorption**
  - The accretion of stress-free material onto a loaded body generates a discontinuous stress profile along the interface. This was illustrated in a model problem presented in

Section 3.5.3 which consists of a cylinder undergoing simultaneous growth/resorption and deformation. The effect of the discontinuities is most prominent when the time step size is large relative to the surface growth velocity, which leads to a finite amount of instantaneously deposited material at each step. Therefore, the numerical accuracy of the fields depends both on the individual element size and the temporal refinement of the surface motion.

- The fields on a body undergoing surface growth-driven dynamic contact depend on the way in which the surface growth/resorption velocities evolve, as was illustrated for an idealized treadmilling cell in Section 4.5. These rudimentary findings could provide the framework for future numerical studies on the effects of contact-inhibited locomotion of cells.

5.2 Potential Future Research Topics

Based on the results and progress of the work documented in this dissertation, there are several recommended potential topics of future research, which are summarized below:

- **Methods development**
  - Introduce a numerical scheme that can simulate surface growth/resorption that is continuous in time. Incorporating such an algorithm into the numerical scheme provided in this work can potentially offer insight into the differences in characteristics between discrete/discontinuous and continuous surface growth. This may possibly be accomplished by predicting the distribution of initial positions of grown material at a given time step t_{n+1}, and computing the deformation gradient based on an assumed deformation history occurring within the range $(t_n, t_{n+1}]$. Corrections can be subsequently applied based on the actual deformation computed between the prior and current time steps.
  - Improve understanding of the relation between extensions of the velocity, stress, and density in the growth region, and the overall evolution of the deforming and growing/resorpting body
  - Incorporate time integration schemes that decouple the step size from the time-scale of surface growth or resorption. This could potentially be accomplished through multi-stage integration such as Runge-Kutta methods, which predict the state at t_{n+1} based on multiple intermediate steps.
  - Couple the current ALE implementation with Eulerian front-tracking approaches which solve for fields outside of the growing/resorpting body
- **Application to cell migration**
  - Incorporate effects of focal adhesion to the cell-barrier simulation. This may be important in providing the cell with a capacity to resist changes in momentum when coming into contact with external barrier.

  - Include dynamic effects of actin filament motion such as those mentioned in [76] to the constitutive model of the actin network

- **Other applications**

  - Develop adaptive meshing capabilities to efficiently discretize domains whose shape is significantly altered throughout the growth or resorption process. This can widen the applicability of the proposed algorithm toward a variety of industrial applications such as additive manufacturing.

Bibliography

[1] R. Skalak, D. A. Farrow, and A. Hoger, "Kinematics of surface growth," *Journal of Mathematical Biology*, vol. 35, no. 8, pp. 869–907, 1997.

[2] R. Skalak, G. Dasgupta, M. Moss, E. Otten, P. Dullemeijer, and H. Vilmann, "Analytical description of growth," *Journal of Theoretical Biology*, vol. 94, no. 3, pp. 555–577, 1982.

[3] J.-F. Ganghoffer, "A contribution to the mechanics and thermodynamics of surface growth. Application to bone external remodeling," *International Journal of Engineering Science*, vol. 50, no. 1, pp. 166–191, 2012.

[4] D. Adalsteinsson and J. A. Sethian, "A level set approach to a unified model for etching, deposition, and lithography," *Journal of Computational Physics*, vol. 138, no. 1, pp. 193–223, 1997.

[5] A.-K. Tornberg and B. Engquist, "The segment projection method for interface tracking," *Communications on Pure and Applied Mathematics*, vol. 56, no. 1, pp. 47–79, 2003.

[6] A. D. Drozdov, "Continuous accretion of a composite cylinder," *Acta Mechanica*, vol. 128, no. 1, pp. 117–135, 1998.

[7] K. Schwerdtfeger, M. Sato, and K.-H. Tacke, "Stress formation in solidifying bodies. Solidification in a round continuous casting mold," *Metallurgical and Materials Transactions B*, vol. 29, no. 5, pp. 1057–1068, 1998.

[8] K. Garikipati, "The kinematics of biological growth," *Applied Mechanics Reviews*, vol. 62, no. 3, pp. 030801–030801–7, 2009.

[9] C. B. Brown and L. E. Goodman, "Gravitational stresses in accreted bodies," *Proceedings of the Royal Society of London. Series A. Mathematical and Physical Sciences*, vol. 276, no. 1367, pp. 571–576, 1963.

[10] R. J. Asaro, "Somigliana dislocations and internal stresses; with application to second phase hardening," *International Journal of Engineering Science*, vol. 13, no. 3, pp. 271–286, 1975.

[11] S. A. Lychev and A. V. Manzhirov, "Reference configurations of growing bodies," *Mechanics of Solids*, vol. 48, no. 5, pp. 553–560, 2013.

[12] S. A. Lychev, "Geometric Aspects of the Theory of Incompatible Deformations in Growing Solids," in *Mechanics for Materials and Technologies* (H. Altenbach, R. V. Goldstein, and E. Murashkin, eds.), Cham: Springer International Publishing, 2017.

[13] V. E. Naumov, "Mechanics of growing deformable solids: A review," *Journal of Engineering Mechanics*, vol. 120, no. 2, pp. 207–220, 1994.

[14] V. V. Metlov, "On the accretion of inhomogeneous viscoelastic bodies under finite deformations," *Journal of Applied Mathematics and Mechanics*, vol. 49, no. 4, pp. 490–498, 1985.

[15] M. Epstein, "Kinetics of boundary growth," *Mechanics Research Communications*, vol. 37, no. 5, pp. 453–457, 2010.

[16] J. D. Humphrey and K. R. Rajagopal, "A constrained mixture model for arterial adaptations to a sustained step change in blood flow," *Biomechanics and Modeling in Mechanobiology*, vol. 2, no. 2, pp. 109–126, 2003.

[17] K. R. Rajagopal and A. R. Srinivasa, "On a class of non-dissipative materials that are not hyperelastic," *Proceedings of the Royal Society A: Mathematical, Physical and Engineering Science*, vol. 465, no. 2102, pp. 493–500, 2009.

[18] N. Hodge and P. Papadopoulos, "A continuum theory of surface growth," *Proceedings of the Royal Society of London A: Mathematical, Physical and Engineering Sciences*, vol. 466, no. 2123, pp. 3135–3152, 2010.

[19] J. Donea, A. Huerta, J. P. Ponthot, and A. Rodríguez-Ferran, "Arbitrary Lagrangian–Eulerian Methods," in *Encyclopedia of Computational Mechanics* (E. Stein, R. de Borst, and T. J. R. Hughes, eds.), Chichester, West Sussex: John Wiley & Sons, 2004.

[20] N. Hodge and P. Papadopoulos, "Continuum modeling and numerical simulation of cell motility," *Journal of Mathematical Biology*, vol. 64, no. 7, pp. 1253–1279, 2012.

[21] P. Papadopoulos and N. Hodge, "On surface growth of actin networks," *International Journal of Engineering Science*, vol. 48, no. 11, pp. 1498–1506, 2010.

[22] J. J. Ong and O. M. O'Reilly, "On the equations of motion for rigid bodies with surface growth," *International Journal of Engineering Science*, vol. 42, no. 19, pp. 2159–2174, 2004.

[23] F. Sozio and A. Yavari, "Nonlinear mechanics of surface growth for cylindrical and spherical elastic bodies," *Journal of the Mechanics and Physics of Solids*, vol. 98, pp. 12–48, 2017.

[24] J.-F. Ganghoffer, "Mechanical modeling of growth considering domain variation—Part II: Volumetric and surface growth involving Eshelby tensors," *Journal of the Mechanics and Physics of Solids*, vol. 58, no. 9, pp. 1434–1459, 2010.

[25] J.-F. Ganghoffer, "Extremum principles for biological continuous bodies undergoing volumetric and surface growth," *Bulletin of the Polish Academy of Sciences Technical Sciences*, vol. 60, no. 2, pp. 259–263, 2012.

[26] J.-F. Ganghoffer, "Mechanics and Thermodynamics of Volumetric and Surface Growth," in *Multiscale Biomechanics*, London: Elsevier, 2018.

[27] J. Sethian and Y. Shan, "Solving partial differential equations on irregular domains with moving interfaces, with applications to superconformal electrodeposition in semiconductor manufacturing," *Journal of Computational Physics*, vol. 227, no. 13, pp. 6411 – 6447, 2008.

[28] A. Romano and A. Marasco, *Continuum Mechanics: Advanced Topics and Research Trends*. Boston: Birkhäuser, 2010.

[29] P. Lidström, "Moving regions in Euclidean space and Reynolds' transport theorem," *Mathematics and Mechanics of Solids*, vol. 16, no. 4, pp. 366–380, 2011.

[30] M. E. Gurtin, A. Struthers, and W. O. Williams, "A transport theorem for moving interfaces," *Quarterly of Applied Mathematics*, vol. 47, no. 4, pp. 773–777, 1989.

[31] G. P. Moeckel, "Thermodynamics of an interface," *Archive for Rational Mechanics and Analysis*, vol. 57, no. 3, pp. 255–280, 1975.

[32] M. E. Gurtin and I. A. Murdoch, "A continuum theory of elastic material surfaces," *Archive for Rational Mechanics and Analysis*, vol. 57, no. 4, pp. 291–323, 1975.

[33] N. M. Newmark, "A method of computation for structural dynamics," *Journal of the Engineering Mechanics Division*, vol. 85, no. 3, 1959.

[34] J. Nocedal and S. J. Wright, *Numerical Optimization*. New York, NY: Springer, 2006.

[35] G. A. Ateshian, "On the theory of reactive mixtures for modeling biological growth," *Biomechanics and Modeling in Mechanobiology*, vol. 6, no. 6, pp. 423–445, 2007.

[36] M. J. Unterberger, K. M. Schmoller, A. R. Bausch, and G. A. Holzapfel, "A new approach to model cross-linked actin networks: Multi-scale continuum formulation and computational analysis," *Journal of the Mechanical Behavior of Biomedical Materials*, vol. 22, pp. 95–114, 2013.

[37] M. J. Unterberger, K. M. Schmoller, C. Wurm, A. R. Bausch, and G. A. Holzapfel, "Viscoelasticity of cross-linked actin networks: Experimental tests, mechanical modeling and finite-element analysis," *Acta Biomaterialia*, vol. 9, no. 7, pp. 7343–7353, 2013.

[38] R. Ananthakrishnan and A. Ehrlicher, "The forces behind cell movement," *International Journal of Biological Sciences*, vol. 3, no. 5, pp. 303–317, 2007.

[39] B. Alberts, A. Johnson, J. Lewis, M. Raff, K. Roberts, and P. Walter, *Molecular Biology of the Cell, 5th Ed.* New York: Garland Science, 2008.

[40] H. Lodish, C. Kaiser, M. Krieger, A. Bretscher, H. Ploegh, A. Amon, and M. Scott, *Molecular Cell Biology, 7th Ed.* New York: W. H. Freeman and Co., 2013.

[41] T. J. Mitchison and L. P. Cramer, "Actin-based cell motility and cell locomotion," *Cell*, vol. 84, no. 3, pp. 371–379, 1996.

[42] A. Mogilner and G. Oster, "Cell motility driven by actin polymerization.," *Biophysical Journal*, vol. 71, no. 6, pp. 3030–3045, 1996.

[43] K. Keren, Z. Pincus, G. M. Allen, E. L. Barnhart, G. Marriott, A. Mogilner, and J. A. Theriot, "Mechanism of shape determination in motile cells," *Nature*, vol. 453, pp. 475–480, 05 2008.

[44] T. M. Svitkina, A. B. Verkhovsky, K. M. McQuade, and G. G. Borisy, "Analysis of the actin–myosin II system in fish epidermal keratocytes: Mechanism of cell body translocation," *The Journal of Cell Biology*, vol. 139, no. 2, p. 397, 1997.

[45] T. D. Pollard and G. G. Borisy, "Cellular motility driven by assembly and disassembly of actin filaments," *Cell*, vol. 112, no. 4, pp. 453–465, 2003.

[46] H. P. Grimm, A. B. Verkhovsky, A. Mogilner, and J. J. Meister, "Analysis of actin dynamics at the leading edge of crawling cells: Implications for the shape of keratocyte lamellipodia," *European Biophysics Journal*, vol. 32, no. 6, pp. 563–577, 2003.

[47] T. D. Pollard, L. Blanchoin, and R. D. Mullins, "Molecular mechanisms controlling actin filament dynamics in nonmuscle cells," *Annual Review of Biophysics and Biomolecular Structure*, vol. 29, no. 1, pp. 545–576, 2000.

[48] A. Mogilner and G. Oster, "Force generation by actin polymerization II: The elastic ratchet and tethered filaments," *Biophysical Journal*, vol. 84, no. 3, pp. 1591–1605, 2003.

[49] S. H. Parekh, O. Chaudhuri, J. A. Theriot, and D. A. Fletcher, "Loading history determines the velocity of actin-network growth," *Nature Cell Biology*, vol. 7, pp. 1219–1223, 2005.

[50] M. Prass, K. Jacobson, A. Mogilner, and M. Radmacher, "Direct measurement of the lamellipodial protrusive force in a migrating cell," *Journal of Cell Biology*, vol. 174, no. 6, p. 767, 2006.

[51] M. J. Footer, J. W. J. Kerssemakers, J. A. Theriot, and M. Dogterom, "Direct measurement of force generation by actin filament polymerization using an optical trap," *Proceedings of the National Academy of Sciences*, vol. 104, no. 7, p. 2181, 2007.

[52] A. E. Carlsson, "Growth of branched actin networks against obstacles," *Biophysical Journal*, vol. 81, no. 4, pp. 1907–1923, 2001.

[53] A. E. Carlsson, "Growth velocities of branched actin networks," *Biophysical Journal*, vol. 84, pp. 2907–2918, 05 2003.

[54] R. B. Dickinson, L. Caro, and D. L. Purich, "Force generation by cytoskeletal filament end-tracking proteins," *Biophysical Journal*, vol. 87, no. 4, pp. 2838–2854, 2004.

[55] C. I. Lacayo, Z. Pincus, M. M. VanDuijn, C. A. Wilson, D. A. Fletcher, F. B. Gertler, A. Mogilner, and J. A. Theriot, "Emergence of large-scale cell morphology and movement from local actin filament growth dynamics," *PLOS Biology*, vol. 5, no. 9, pp. 2035–2052, 2007.

[56] A. Mogilner and B. Rubinstein, "Actin disassembly 'clock' and membrane tension determine cell shape and turning: a mathematical model," *Journal of physics. Condensed matter*, vol. 22, no. 19, pp. 194118–194118, 2010.

[57] D. Kabaso, R. Shlomovitz, K. Schloen, T. Stradal, and N. S. Gov, "Theoretical model for cellular shapes driven by protrusive and adhesive forces," *PLOS Computational Biology*, vol. 7, no. 5, pp. 1–13, 2011.

[58] B. Rubinstein, K. Jacobson, and A. Mogilner, "Multiscale two-dimensional modeling of a motile simple-shaped cell," *Multiscale modeling & simulation*, vol. 3, no. 2, pp. 413–439, 2005.

[59] G. MacDonald, J. Mackenzie, M. Nolan, and R. Insall, "A computational method for the coupled solution of reaction–diffusion equations on evolving domains and manifolds: Application to a model of cell migration and chemotaxis," *Journal of Computational Physics*, vol. 309, pp. 207–226, 2016.

[60] C. M. Elliott, B. Stinner, and C. Venkataraman, "Modelling cell motility and chemotaxis with evolving surface finite elements," *Journal of The Royal Society Interface*, vol. 9, no. 76, pp. 3027–3044, 2012.

[61] K. Keren and J. A. Theriot, "Biophysical Aspects of Actin-Based Cell Motility in Fish Epithelial Keratocytes," in *Cell Motility* (P. Lenz, ed.), New York: Springer, 2008.

[62] G. A. Holzapfel and R. W. Ogden, "On the bending and stretching elasticity of biopolymer filaments," *Journal of Elasticity*, vol. 104, no. 1, pp. 319–342, 2011.

[63] G. A. Holzapfel and R. W. Ogden, "Elasticity of biopolymer filaments," *Acta Biomaterialia*, vol. 9, no. 7, pp. 7320–7325, 2013.

[64] J. Stricker, T. Falzone, and M. L. Gardel, "Mechanics of the f-actin cytoskeleton," *Journal of Biomechanics*, vol. 43, no. 1, pp. 9–14, 2010.

[65] K. Kruse, J. F. Joanny, F. Jülicher, J. Prost, and K. Sekimoto, "Asters, vortices, and rotating spirals in active gels of polar filaments," *Physical Review Letters*, vol. 92, pp. 078101–, 02 2004.

[66] K. Kruse, J. F. Joanny, F. Jülicher, J. Prost, and K. Sekimoto, "Generic theory of active polar gels: a paradigm for cytoskeletal dynamics," *European Physical Journal E*, vol. 16, no. 1, pp. 5–16, 2005.

[67] K. Kruse, J. F. Joanny, F. Jülicher, and J. Prost, "Contractility and retrograde flow in lamellipodium motion," *Physical Biology*, vol. 3, no. 2, p. 130, 2006.

[68] Y. Sakamoto, S. Prudhomme, and M. H. Zaman, "Viscoelastic gel-strip model for the simulation of migrating cells," *Annals of Biomedical Engineering*, vol. 39, no. 11, p. 2735, 2011.

[69] M. L. Gardel, J. H. Shin, F. C. MacKintosh, L. Mahadevan, P. Matsudaira, and D. A. Weitz, "Elastic behavior of cross-linked and bundled actin networks," *Science*, vol. 304, no. 5675, pp. 1301–1305, 2004.

[70] M. L. Gardel, F. Nakamura, J. Hartwig, J. C. Crocker, T. P. Stossel, and D. A. Weitz, "Stress-dependent elasticity of composite actin networks as a model for cell behavior," *Physical Review Letters*, vol. 96, no. 8, pp. 088102–, 2006.

[71] R. Tharmann, M. M. A. E. Claessens, and A. R. Bausch, "Viscoelasticity of isotropically cross-linked actin networks," *Physical Review Letters*, vol. 98, no. 8, pp. 088103–, 2007.

[72] G. A. Holzapfel, "Similarities between soft biological tissues and rubberlike materials," in *Constitutive Models for Rubber IV: Proceedings of the 4th European Conference for Constitutive Models for Rubber*, (London), A.A. Balkema Publishers, 2005.

[73] O. Kratky and G. Porod, "Röntgenuntersuchung gelöster Fadenmoleküle," *Recueil des Travaux Chimiques des Pays-Bas*, vol. 68, no. 12, pp. 1106–1122, 1949.

[74] C. P. Broedersz and F. C. MacKintosh, "Modeling semiflexible polymer networks," *Reviews of Modern Physics*, vol. 86, no. 3, pp. 995–1036, 2014.

[75] F. C. MacKintosh, J. Käs, and P. A. Janmey, "Elasticity of semiflexible biopolymer networks," *Physical Review Letters*, vol. 75, no. 24, pp. 4425–4428, 1995.

[76] F. C. MacKintosh, "Polymer-based models of cytoskeletal networks," in *Cytoskeletal Mechanics: Models and Measurements in Cell Mechanics* (M. R. K. Mofrad and R. D. Kamm, eds.), Cambridge: Cambridge University Press, 2006.

[77] S. Klinge, S. Aygün, R. P. Gilbert, and G. A. Holzapfel, "Multiscale fem simulations of cross-linked actin network embedded in cytosol with the focus on the filament orientation," *International Journal for Numerical Methods in Biomedical Engineering*, vol. 34, no. 7, p. e2993, 2018.

[78] C. Miehe, S. Göktepe, and F. Lulei, "A micro-macro approach to rubber-like materials—part i: the non-affine micro-sphere model of rubber elasticity," *Journal of the Mechanics and Physics of Solids*, vol. 52, no. 11, pp. 2617–2660, 2004.

[79] D. A. Head, A. J. Levine, and F. C. MacKintosh, "Distinct regimes of elastic response and deformation modes of cross-linked cytoskeletal and semiflexible polymer networks," *Physical Review E*, vol. 68, no. 6, pp. 061907–, 2003.

[80] P. Bažant and B. H. Oh, "Efficient numerical integration on the surface of a sphere," *ZAMM - Journal of Applied Mathematics and Mechanics / Zeitschrift für Angewandte Mathematik und Mechanik*, vol. 66, no. 1, pp. 37–49, 1986.

[81] G. A. Holzapfel, "On large strain viscoelasticity: Continuum formulation and finite element applications to elastomeric structures," *International Journal for Numerical Methods in Engineering*, vol. 39, no. 22, pp. 3903–3926, 30 November 1996.

[82] J. C. Simo, "On a fully three-dimensional finite-strain viscoelastic damage model: Formulation and computational aspects," *Computer Methods in Applied Mechanics and Engineering*, vol. 60, no. 2, pp. 153–173, 1987.

[83] S. Reese and S. Govindjee, "A theory of finite viscoelasticity and numerical aspects," *International Journal of Solids and Structures*, vol. 35, no. 26, pp. 3455–3482, 1998.

[84] S. Govindjee, T. Potter, and J. Wilkening, "Dynamic stability of spinning viscoelastic cylinders at finite deformation," *International Journal of Solids and Structures*, vol. 51, no. 21, pp. 3589–3603, 2014.

[85] J. Xu, T. Yiider, and D. Wirtz, "Strain hardening of actin filament networks," *Journal of Biological Chemistry*, vol. 275, no. 46, pp. 35886–35892, 2000.

[86] S. A. Koestler, K. Rottner, F. Lai, J. Block, M. Vinzenz, and J. V. Small, "F- and g-actin concentrations in lamellipodia of moving cells," *PLOS ONE*, vol. 4, no. 3, pp. e4810–, 2009.

[87] J. V. Small, T. Stradal, E. Vignal, and K. Rottner, "The lamellipodium: where motility begins," *Trends in Cell Biology*, vol. 12, no. 3, pp. 112–120, 2002.

[88] O. C. Zienkiewicz, R. L. Taylor, and D. D. Fox, *The Finite Element Method for Solid and Structural Mechanics*. Oxford: Butterworth-Heinemann, 7 ed., 2014.

[89] S. Klinkel and S. Govindjee, "Using finite strain 3d-material models in beam and shell elements," *Engineering Computations: International Journal for Computer-Aided Engineering*, vol. 19, no. 3, pp. 254–271, 2002.

[90] T. J. R. Hughes, *The Finite Element Method : Linear Static and Dynamic Finite Element Analysis.* Mineola: Dover Publications, 2000.

[91] A. Roycroft and R. Mayor, "Forcing contact inhibition of locomotion," *Trends in Cell Biology*, vol. 25, no. 7, pp. 373–375, 2015.

[92] A. Roycroft and R. Mayor, "Molecular basis of contact inhibition of locomotion," *Cellular and Molecular Life Sciences*, vol. 73, no. 6, pp. 1119–1130, 2016.

[93] J. R. Davis, A. Luchici, F. Mosis, J. Thackery, J. A. Salazar, Y. Mao, G. A. Dunn, T. Betz, M. Miodownik, and B. M. Stramer, "Inter-cellular forces orchestrate contact inhibition of locomotion," *Cell*, vol. 161, no. 2, pp. 361–373, 2015.

[94] D. A. Kulawiak, B. A. Camley, and W.-J. Rappel, "Modeling contact inhibition of locomotion of colliding cells migrating on micropatterned substrates," *PLOS Computational Biology*, vol. 12, no. 12, pp. e1005239–, 2016.

[95] F. Ziebert, J. Löber, and I. S. Aranson, "Macroscopic Model of Substrate-Based Cell Motility," in *Physical Models of Cell Motility* (I. S. Aranson, ed.), pp. 1–67, Cham: Springer International Publishing, 2016.

[96] W. H. Grover, A. K. Bryan, M. Diez-Silva, S. Suresh, J. M. Higgins, and S. R. Manalis, "Measuring single-cell density," *Proceedings of the National Academy of Sciences*, vol. 108, no. 27, pp. 10992–10996, 2011.

[97] R. L. Taylor and P. Papadopoulos, "On a finite element method for dynamic contact/impact problems," *International Journal for Numerical Methods in Engineering*, vol. 36, no. 12, pp. 2123–2140, 1993.

[98] J. U. Brackbill and J. S. Saltzman, "Adaptive zoning for singular problems in two dimensions," *Journal of Computational Physics*, vol. 46, no. 3, pp. 342–368, 1982.

[99] A. M. Winslow, "Numerical solution of the quasilinear poisson equation in a nonuniform triangle mesh," *Journal of Computational Physics*, vol. 1, no. 2, pp. 149–172, 1966.

[100] T. Belytschko, N. Moës, S. Usui, and C. Parimi, "Arbitrary discontinuities in finite elements," *International Journal for Numerical Methods in Engineering*, vol. 50, no. 4, pp. 993–1013, 2001.

[101] P. Wriggers, *Computational Contact Mechanics*. Berlin: Springer, 2006.

[102] P. Wriggers and J. C. Simo, "A note on tangent stiffness for fully nonlinear contact problems," *Communications in Applied Numerical Methods*, vol. 1, no. 5, pp. 199–203, 1985.

[103] "Eigen." `http://eigen.tuxfamily.org/`, 2008–2019.

[104] L. Thomason, "Tinyxml2." `https://github.com/leethomason/tinyxml2`, 2012–2019.

[105] "Googletest." `https://github.com/google/googletest`, 2015–2019.

[106] C. Geuzaine and J.-F. Remacle, "Gmsh: a three-dimensional finite element mesh generator with built-in pre- and post-processing facilities," *International Journal for Numerical Methods in Engineering*, vol. 79, no. 11, pp. 1309–1331, 2009.

[107] D. van Heesch, "Doxygen." `http://www.doxygen.nl`, 1997–2018.

Appendix A

Numerical Algorithms

A.1 Surface Growth/Resorption Algorithm

In this section, the algorithmic procedure for updating the surface growth/resorption velocity, as well as the other field variables such as the material velocity, density, and stress is schematically illustrated. The pseudo-code shown in Algorithms 1 and 2 emphasizes the order in which each of the procedures is executed. Details of the algorithms and concepts specific to surface growth are further elaborated in Appendices A.3 to A.5.

Algorithm 1: Surface growth/resorption algorithm for dynamic bodies

Initialize field variables
Set $n = 0$
while $n < n\_steps$ **do** ▷ Begin time loop
  $t \leftarrow \tau + n\Delta t$ ▷ Update current time
  Initialize $\hat{\boldsymbol{\rho}}_{n+1}^{0} = \hat{\bar{\boldsymbol{\rho}}}_{n}$
  Initialize $\hat{\mathbf{v}}_{n+1}^{0} = \hat{\bar{\mathbf{v}}}_{n}$
  Initialize $\hat{\boldsymbol{\varphi}}_{n+1}^{0} = \hat{\bar{\boldsymbol{\varphi}}}_{n}$
  Set $j = 0$
  $j \leftarrow j + 1$
  while $j < num\_staggered\_iterations$ **do** ▷ Begin staggered iterations
    if $\mathbf{v}_g$ depends on $\boldsymbol{\varphi}$ **then**
      Set $k = 0$
      while $k \leq iter_{max}$ and $||resid||_2 \geq tol$ **do** ▷ Solve Equation (3.45)
        Compute residual and tangent based on Equation (3.45)
        Solve for increment $\leftarrow$ Compute $\hat{\boldsymbol{\varphi}}_{n+1}^{j,k+1}$
        $k \leftarrow k + 1$
      end while
    end if
    Convect mesh based on: $\tilde{\mathbf{x}}_{n+1}^{j} = \mathbf{x}_n + \mathbf{v}_{g,n+1}^{j}\Delta t$ ▷ See Appendix A.3
    Project fields in $\mathcal{M}$ onto new mesh ▷ See Appendix A.4
    Generate growth and resorption initial fields in $\mathcal{G}$, $\tilde{\Gamma}_g$, and $\tilde{\Gamma}_a$ ▷ See Appendix A.5
    Solve for $\hat{\boldsymbol{\rho}}_{n+1}^{j}$ based on Equation (3.32) assuming $\hat{\mathbf{v}}_{n+1} = \hat{\mathbf{v}}_{n+1}^{j-1}$
    Assign $\hat{\boldsymbol{\rho}}_{n+1} = \hat{\boldsymbol{\rho}}_{n+1}^{j}$
    Initialize $\hat{\mathbf{v}}_{n+1}^{j,0}$
    Set $k = 0$
    while $k \leq iter_{max}$ and $||resid||_2 \geq tol$ **do** ▷ Solve Equation (3.33)
      Update displacements and accelerations
      Update Cauchy stress, deformation gradient, and any state variables
      Compute residual and tangent based on Equation (3.33)
      Solve for increment $\leftarrow$ Compute $\hat{\mathbf{v}}_{n+1}^{j,k+1}$
      $k \leftarrow k + 1$
    end while
    Update current positions based on $\mathbf{v}_{n+1}^{j}$.
    $j \leftarrow j + 1$ ▷ Update staggered step
  end while
  $n \leftarrow n + 1$ ▷ Update simulation step
end while

Algorithm 2: Surface growth/resorption algorithm for quasi-static (non-inertial) bodies with no body forces

Initialize field variables
Set $n = 0$
while $n < n\_steps$ **do** ▷ Begin time loop
  $t \leftarrow \tau + n\Delta t$ ▷ Update current time
  Initialize $\Delta\hat{\mathbf{u}}^{0}_{n+1} = \Delta\hat{\mathbf{u}}_n$
  Initialize $\hat{\tilde{\boldsymbol{\varphi}}}^{0}_{n+1} = \hat{\tilde{\boldsymbol{\varphi}}}_n$
  Set $j = 0$
  $j \leftarrow j + 1$
  while $j < num\_staggered\_iterations$ **do** ▷ Begin staggered iterations
    if $\mathbf{v}_g$ depends on $\boldsymbol{\varphi}$ **then**
      Set $k = 0$
      while $k \leq iter_{max}$ and $||resid||_2 \geq tol$ **do** ▷ Solve Equation (3.45)
        Compute residual and tangent of Equation (3.45)
        Solve for increment $\leftarrow$ Compute $\hat{\boldsymbol{\varphi}}^{j,k+1}_{n+1}$
        $k \leftarrow k + 1$
      end while
    end if
    Convect mesh based on: $\tilde{\mathbf{x}}^{j}_{n+1} = \mathbf{x}_n + \mathbf{v}^{j}_{g,n+1}\Delta t$ ▷ See Appendix A.3
    Project fields in $\mathcal{M}$ onto new mesh ▷ See Appendix A.4
    Generate growth and resorption initial fields in $\mathcal{G}$, $\tilde{\Gamma}_g$, and $\tilde{\Gamma}_a$ ▷ See Appendix A.5
    Initialize $\Delta\hat{\mathbf{u}}^{j,0}_{n+1}$
    Set $k = 0$
    while $k \leq iter_{max}$ and $||resid||_2 \geq tol$ **do** ▷ Solve Equation (3.44)
      Update displacement increments
      Update Cauchy stress, deformation gradient, and any state variables
      Compute residual and tangent based on Equation (3.44)
      Solve for increment $\leftarrow$ Compute $\Delta\hat{\boldsymbol{u}}^{j,k+1}_{n+1}$
      $k \leftarrow k + 1$
    end while
    Update current positions based on $\Delta\hat{\boldsymbol{u}}^{j}_{n+1}$.
    $j \leftarrow j + 1$ ▷ Update staggered step
  end while
  $n \leftarrow n + 1$ ▷ Update simulation step
end while

A.2 Orthogonal Projection

The procedure described in this section is used to track the growth/resorption front (Appendix A.5) as well as the contact interface (Appendix A.6).

Consider a one-dimensional curve with the local coordinate ξ embedded in a two-dimensional Euclidean space. Consider a point outside the curve with Cartesian coordinates defined by the vector $\boldsymbol{r}$ and a curve whose points are characterized by the vector $\boldsymbol{\rho}(\xi)$. Moreover, this curve is discretized with piecewise linear functions, as shown in Figure A.1.

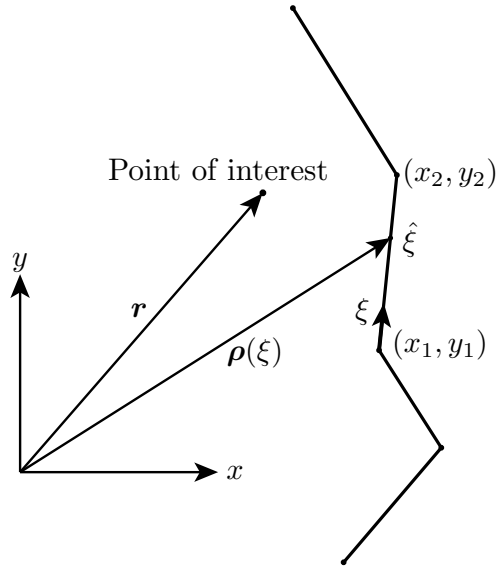

Figure A.1: *Initial set-up for a closest point projection of a point onto a one-dimensional piecewise linear curve.*

A distance function $F(\xi)$ can be defined as

$$F(\xi) = \frac{1}{2}||\boldsymbol{r} - \boldsymbol{\rho}(\xi)||_2^2 \,. \tag{A.1}$$

Here, $||\cdot||_2$ denotes the Euclidean vector norm. Seeking a minimum of the above function also obtains the point along the curve described by $\boldsymbol{\rho}$ for which its distance from $\boldsymbol{r}$ is minimized.

The above equation can generally be nonlinear, thus requiring a root-finding algorithm to obtain a solution. However, restricting the curve $\boldsymbol{\rho}$ to one-dimensional piecewise linear functions that are C^0 leads to a linear equation in ξ. One issue that arises when optimizing Equation (A.1) with C^0 functions is that their derivative is not well-defined at the intersections of the piecewise linear segments. To circumvent this difficulty, an individual optimization of Equation (A.1) is performed for each piecewise linear segment that is within a user-specified distance from the point $\boldsymbol{r}$ by constraining the solution space to $\hat{\xi} \in [0, L]$, where L is the length of a given segment. The final solution is then chosen as the minimum over all of the distances computed by the optimization of each individual segment. The optimal solution on a given segment is determined by a single iteration using Newton's method:

$$\hat{\xi} = \hat{\xi}_0 + \left[\frac{d\boldsymbol{\rho}(\hat{\xi}_0)}{d\xi}\right]^T \left(\boldsymbol{r} - \boldsymbol{\rho}(\hat{\xi}_0)\right), \tag{A.2}$$

where $\hat{\xi}_0$ is an initial guess of the solution, and $\boldsymbol{\rho}(\xi)$ is defined for a given segment as

$$\boldsymbol{\rho}(\xi) = \begin{bmatrix} \left(1 - \frac{1}{L}\xi\right)x_1 + \left(\frac{1}{L}\xi\right)x_2 \\ \left(1 - \frac{1}{L}\xi\right)y_1 + \left(\frac{1}{L}\xi\right)y_2 \end{bmatrix}. \tag{A.3}$$

Here, the start point and end point have coordinates (x_1, y_1) and (x_2, y_2) respectively. The length is defined as $L = \sqrt{(x_2 - x_1)^2 + (y_2 - y_1)^2}$. The constraint is applied in an indirect manner. If $\hat{\xi} < 0$, it is assigned as 0. Likewise, $\hat{\xi} = L$ if the above solution is greater than the length. It is assumed that the solution ξ always exists. Moreover, If the solution of Equation (A.1) is not unique, it is assumed that only one of the segments where the solution $\hat{\xi}$ lies is chosen to determine the distance between the point at $\boldsymbol{r}$ and the surface.

A.3 Mesh Motion Algorithm

In this section, the procedure for convecting the mesh of a growing/resorpting body is described. This task is performed once the growth velocities are known along the entire surface for a given time, as highlighted in Algorithms 1 and 2 of Appendix A.1.

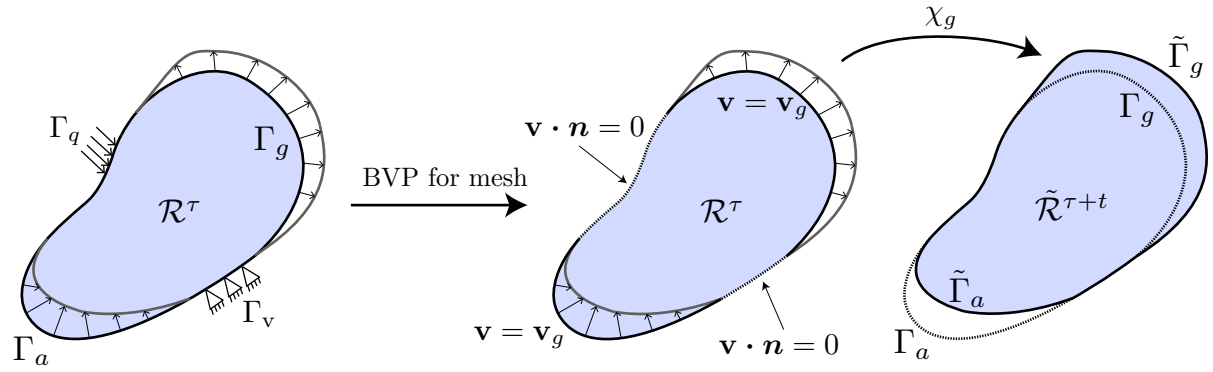

Figure A.2: *Schematic of boundary-value problem to determine mesh motion based on surface growth velocity*

With a known surface growth velocity at a given time $\tau + t$, the boundary is convected by the specified growth and resorption velocities, as is schematically illustrated in Figure A.2. On portions of the surface ∂R^τ that do not have a prescribed surface growth or resorption, the condition $\mathbf{v} \cdot \boldsymbol{n} = 0$ is enforced to allow only tangential motion of the mesh. If Neumann or Dirichlet portions of the boundary (Γ_q and Γ_v respectively) coincide with the growth/resorption surface, these regions are assumed to convect onto the boundary of the newly grown surface as well. In this case, the boundary conditions are applied on a different set of material points at time $\tau + t$ than they are at time τ.

In order to alleviate mesh distortion, the interior mesh must convect during the growth/resorption phase as well. In this work it is assumed, that the mesh connectivities (and correspondingly, the number of elements and nodes) remain unaltered as it convects. To accomplish this task with minimal change in mesh distribution and uniformity, linear momentum balance is solved on the interior mesh with the boundary conditions $\mathbf{v} = \mathbf{v}_g$ on Γ_a and Γ_g, and $\mathbf{v} \cdot \boldsymbol{n} = 0$ elsewhere. The initial velocities in the interior are set to zero, and the density and material constants are set by the user. Note that the material constitution assigned to the mesh is not physical, since it correlates to a non-material mesh motion. Once the initial data are known, the new mesh velocities $\mathbf{v}^m_{n+1}$ at a discrete time t_{n+1} are solved iteratively using the backward Euler time integration scheme,

$$\boldsymbol{M}^m \hat{\mathbf{v}}^m_{n+1} - \Delta t_{n+1} \hat{\boldsymbol{F}}^m_{n+1} \;=\; \mathbf{0}\,, \tag{A.4}$$

where $\boldsymbol{M}^m$ and $\hat{\boldsymbol{F}}^m_{n+1}$ are defined as

$$\begin{aligned} \boldsymbol{M}^m \;&=\; \mathop{\mathsf{A}}_{e=1}^{nel} \left[\int_{\Omega^e} (\boldsymbol{N}^e)^T (\bar{\boldsymbol{N}}^e \hat{\boldsymbol{\rho}}^{m,e}) \boldsymbol{N}^e \, dv \right], \\ \hat{\boldsymbol{F}}^m_{n+1} \;&=\; \mathop{\mathsf{A}}_{e=1}^{nel} \left[\int_{\Omega^e} -(\boldsymbol{B}^e)^T \hat{\boldsymbol{T}}^{m,e}_{n+1} \, dv \right]. \end{aligned} \tag{A.5}$$

In Equation (A.5), $\hat{\boldsymbol{\rho}}^{m,e}$ and $\hat{\boldsymbol{T}}^{m,e}_{n+1}$ are the fictitious element density and stress (ordered in vector form), respectively. A neo-Hookean constitutive law is used to define the fictitious stress on the mesh, which is defined as

$$\boldsymbol{T}^m = \frac{\mu^m}{J^m}(\boldsymbol{b}^m - \boldsymbol{i}) + \lambda^m \frac{log J^m}{J^m} \boldsymbol{i}\,. \tag{A.6}$$

In Equation (A.6), the Jacobian of the mesh motion is defined as $J^m = det(\boldsymbol{F}^m)$, $\boldsymbol{b}^m = \boldsymbol{F}^m(\boldsymbol{F}^m)^T$ is the left stretch, and μ^m, λ^m are the constants defining the elastic properties of the mesh. Additionally, $\boldsymbol{i}$ is the identity tensor in the spatial configuration of the mesh. The deformation gradient of the mesh $\boldsymbol{F}^m$ is obtained for a given time t_{n+1} based on the gradient of the incremental mesh displacement defined by $\Delta \boldsymbol{u}^m_{n+1} = \mathbf{x}^m_{n+1} - \mathbf{x}^m_n$ relative to the positions at time t_n

$$\boldsymbol{F}^m = \boldsymbol{I} + \frac{\partial \Delta \boldsymbol{u}^m_{n+1}}{\partial \mathbf{x}_n}\,. \tag{A.7}$$

The growth/resorption velocities on Γ_a and Γ_g, and the normal velocities on the other portions of Γ are known from the outset and are thus not included in Equation (A.4). Once the mesh velocities $\mathbf{v}^m_{n+1}$ are known, the new nodal coordinates are updated as follows

$$\mathbf{x}^m_{n+1} = \mathbf{x}^m_n + \Delta t \mathbf{v}^m_{n+1}\,. \tag{A.8}$$

The solution scheme above relies on the knowledge of the surface growth and resorption velocities $\mathbf{v}_g$ at time t_{n+1}. In cases where the growth/resorption velocities are functions of the

deformations or material velocities, $\mathbf{v}_g$ can change in time. The simplest strategy to determine the new growth/resorption velocities is an explicit update of $\mathbf{v}_{g,n+1}$ which solely relies on the deformation or material velocities at t_n, and hence there exists an inherent lag in the update of the growth velocities. Alternatively, the growth velocities at t_{n+1} can be obtained implicitly. This is achieved by iteratively obtaining a value of $\mathbf{v}_g$, convecting the mesh, and solving for the new material densities and velocities at t_{n+1} until the difference in the coordinates at an iteration reaches a minimum tolerance. The procedures for the explicit and implicit schemes are illustrated schematically in Figure B.3 and Figure B.4, respectively. Although the implicit scheme provides a more accurate growth/resorption velocity, it incurs a significantly higher computation cost due to the repetitive staggered solves for the growth/resorption and material fields.

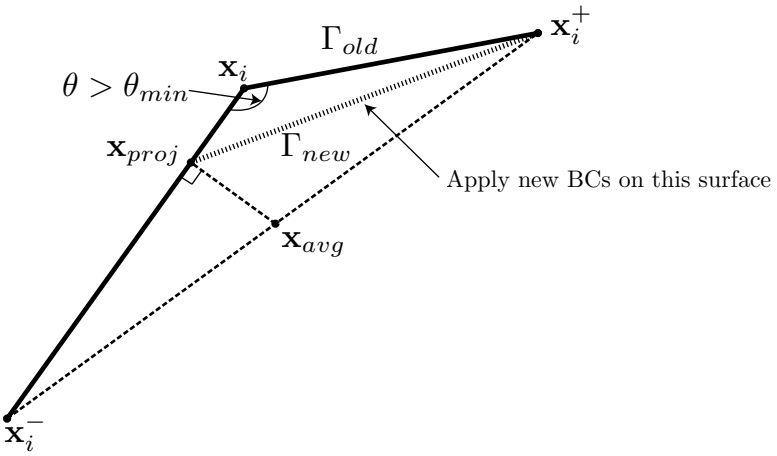

Figure A.3: *Surface smoothing algorithm for a given node based on position averaging and closest-point projection.*

Poisson smoothing provides an alternative to obtaining the mesh motion by solving a set of local balance laws at each node. This algorithm is based on the works of [98] and [99]. The authors in these works define a potential whose minimization achieves a combination of optimal mesh smoothness, orthogonality, and weighted volume. The optimization of the mesh smoothness is equivalent to solving the Poisson equation along lines of equipotential on the mesh. A finite difference approximation can easily be obtained for a given node in terms of the coordinates of its nearest neighbors by swapping the physical variables with a set of parametrized variables defined on a square grid and solving the same differential equation for the new coordinates of the mesh. This method offers a distinct advantage in that it does not require a numerical algorithm to obtain a solution since its closed form is already defined on a regular grid, and can thus be used for any set of mesh coordinates. In conjunction with the Poisson smoothing in the interior, a simple surface smoothing procedure can be implemented by averaging a boundary node's neighbor positions and projecting the averaged point onto the mesh boundary, as is illustrated in Figure A.3. The combined surface and interior smoothing algorithm is shown in Algorithm 3. Although this method is far more computationally efficient than solving a global balance law to determine the mesh motion, it is not as robust in maintaining a uniform mesh, especially in cases where the boundary is highly deformed. The interior/surface smoothing procedure was used in test problems not shown in this

Algorithm 3: Mesh smoothing algorithm

for $c = 0$ to num_cycles **do** ▷ Number of surface-interior smoothing cycles
  for $\mathbf{x}_i \in \partial\Omega$ **do** ▷ Surface smoothing
    Obtain left and right neighbors, $\mathbf{x}_i^-$ and $\mathbf{x}_i^+$
    Compute angle θ between the two vectors $\mathbf{x}_i^- - \mathbf{x}_i$ and $\mathbf{x}_i - \mathbf{x}_i^+$.
    if $\theta > \theta_{min}$ **then** ▷ Anything less than θ_{min} is considered a corner node
      Average neighbor positions, $\mathbf{x}_i = 0.5(\mathbf{x}_i^+ + \mathbf{x}_i^-)$
      Perform closest point projection to map $\mathbf{x}_i$ onto $\partial\Omega$
    end if
  end for
  for $\mathbf{x}_i \in \Omega$ **do** ▷ Interior smoothing
    Obtain neighbors in all directions
    Perform Poisson smoothing on $\mathbf{x}_i$ until desired convergence
  end for
end for
Re-assign Γ_a,Γ_g,Γ_v, and Γ_q based on new nodal locations of surface

work. This procedure was also used to smooth the initial meshes of the simulations conducted in Sections 3.5.2 and 4.5.3 (meshes are shown in Figures 3.2 and 4.12).

A.4 Field Projection Algorithm

In this section, the procedure for projecting fields between the ungrown and grown mesh is described. This step is performed once the new positions of the grown/resorpted body is known relative to its ungrown state, as highlighted in Algorithms 1 and 2 of Appendix A.1.

The projection solves for the new field variables by performing a global least-squares optimization in the spatially discretized intermediate configuration

$$\int_{\tilde{\Omega}} ||\tilde{\boldsymbol{f}} - \boldsymbol{f}||_2^2 \, dv = \min , \tag{A.9}$$

where $\tilde{\boldsymbol{f}}$ is the global vector of a given field variable in the new mesh (defined in the intermediate configuration), and $\boldsymbol{f}$ is the fixed global solution of the same field variable on the old mesh (defined in the ungrown configuration). This leads to the discretized system of equations

$$\boldsymbol{M}\tilde{\boldsymbol{f}} = \boldsymbol{b} \tag{A.10}$$

for the unknown nodal vector $\tilde{\boldsymbol{f}}$, where

$$\begin{aligned} \boldsymbol{M} &= \mathop{\mathsf{A}}_{e=1}^{nel} \left[\int_{\Omega^e} (\boldsymbol{N}^e)^T \boldsymbol{N}^e \, dv \right], \\ \boldsymbol{b} &= \mathop{\mathsf{A}}_{e=1}^{nel} \left[\int_{\Omega^e} \boldsymbol{f}^e \, dv \right]. \end{aligned} \tag{A.11}$$

The array of shape functions $\boldsymbol{N}^e$ is equivalent to $\boldsymbol{N}^e$ in Equation (3.11) when solving for vector-valued variables and $\bar{\boldsymbol{N}}^e$ when solving for scalar variables. When projecting tensors with more than two components such as the deformation gradient and Cauchy stress, each component is solved separately as a scalar field.

The integral in $\boldsymbol{b}$ is evaluated by searching for the element in the old (ungrown) mesh Ω which contains the coordinates of a given integration point $\mathbf{x}_{ip}$ in the current mesh $\tilde{\Omega}$. This search is performed for every integration point in $\tilde{\Omega}$ using the ray-casting point-in-polygon search algorithm. Selecting a point $\mathbf{x}_{ip}$, a fictional line is extended along a user-specified direction with a length that is longer than the side lengths of neighboring elements. If this line intersects the edges of a given element an odd number of times, the point is inside the element. Additionally, if the ray intersects the edge of an element an even number of times but is co-linear with two adjacent element nodes, the point lies on the edge of the element. This procedure is graphically illustrated in Figure A.4.

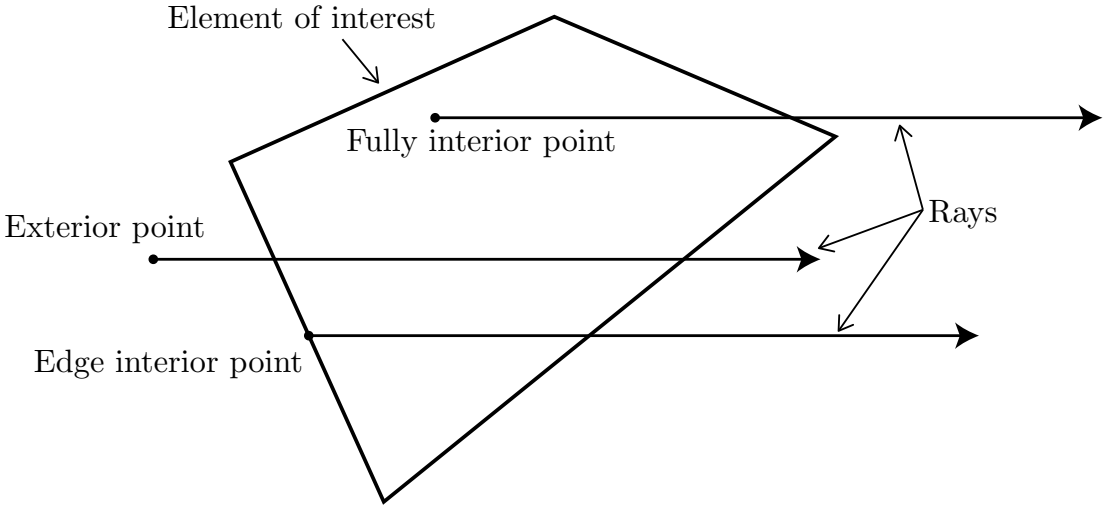

Figure A.4: *Ray-cast performed for a fully interior, edge interior, and exterior node.*

Once the element e^* encompassing $\mathbf{x}_{ip}$ in the old mesh Ω is found, the natural coordinates $\mathbf{x}^*$ in the isoparametric frame are determined by solving the vector-valued equation

$$\boldsymbol{N}^e(\boldsymbol{\xi})\hat{\mathbf{x}}^e - \mathbf{x}_{ip} = 0 \tag{A.12}$$

for the isoparametric variable $\boldsymbol{\xi}$. Here, $\boldsymbol{N}^e(\boldsymbol{\xi})$ is the typical array of shape functions for two dimensions defined by Equation (3.11) and $\hat{\mathbf{x}}^e$ is vector of nodal coordinates for the element e^*.

For four-noded quadrilateral elements, the shape functions $\boldsymbol{N}^e(\boldsymbol{\xi})$ are nonlinear in $\boldsymbol{\xi}$ and are thus obtained using Newton's method.

The contribution of $\boldsymbol{f}^e$ for elements in the intermediate configuration that contain newly accreted material lacks a physical meaning, since the field $\boldsymbol{f}$ is defined in the ungrown configuration. The value of $\boldsymbol{f}$ must exist, however, to obtain a global solution for the projected field $\tilde{\boldsymbol{f}}$. In this setting, a "fictitious" assumed field is generated in the growth regions by simply assigning the value at $\mathbf{x}_{ip}$ in those locations to the identical value at the closest point of the ungrown mesh boundary $\partial\Omega$. Although it is also possible to simply prescribe the values of $\boldsymbol{f}$ as zero (or alternatively as the actual extension solutions), the sharp discontinuities in the distribution of $\boldsymbol{f}$ along the growth front can lead to significant errors in the projected values near the growth interface.

Algorithm 4: L_2 projection for mesh of body undergoing surface growth/resorption

```
for Ω^e ∈ Ω̃ do                                  ▷ Elements in intermediate configuration
    for x̃_ip ∈ Ω^e do                            ▷ Integration points of an element
        if x̃_ip ∉ G then                         ▷ Only project points common to both meshes
            Find x* and e* based on mesh of Ω
            Interpolate within e* to find field f at x*
        else
            Construct assumed field at x̃_ip
        end if
        Assemble M^e and f^e into global system
    end for
end for
Solve for f̃
```

A.5 Front-tracking Algorithm

In this section, the algorithmic implementation for the evolution of a surface based on its growth/resorption velocity is discussed. This procedure is carried out when the growth velocity $\mathbf{v}_g$ and the corresponding positions of the grown boundary are known at a given time, as indicated in Algorithms 1 and 2 of Appendix A.1.

The algorithm used for tracking the grown configuration is based on flagging mesh nodes and element integration points as "growth" or "resorption" by projecting the given points onto the ungrown surface of the prior time step using the orthogonal projection procedure described in Appendix A.2. The pseudo-code of these algorithms for a given growth/resorption increment is shown in Algorithms 5 and 6.

Some elements can bisect the ungrown boundary as shown in Figure A.5. This occurs as a result of the misalignment of the mesh with prior discrete growth boundaries, which is a feature that is difficult to avoid for general two-dimensional surface motions. In this setting, the values at the integration points and nodes are projected from existing fields at the prior time step if they are placed within the interior of the old boundary, or they are assigned a corresponding growth

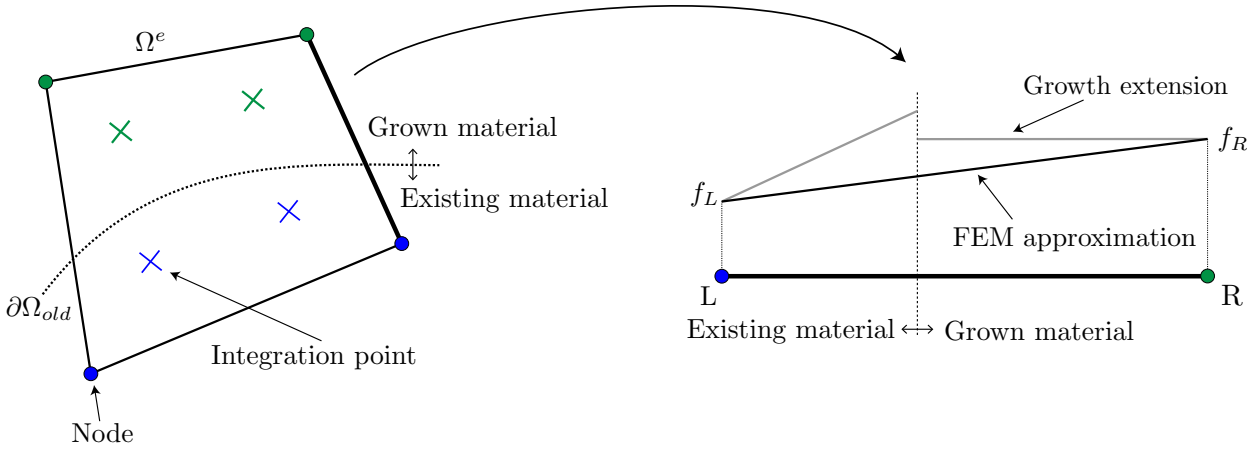

Figure A.5: *Node and integration point flagging for a single element based on distance relative to the ungrown boundary $\partial\Omega_{old}$ (left), and an example of the approximated field along an element edge using continuous interpolation functions (right)*

extension value. For fields defined on nodes in the grown region, the values within the element are interpolated using the standard finite element interpolation functions. As highlighted in Figure A.5, this interpolation scheme introduces an error for elements intersecting the growth boundary since the discontinuity in the value of the field[4] cannot be captured by smooth interpolation functions. As the element size is refined, the accuracy of the transition between growth and prior fields is expected to improve as well, as was highlighted in Section 3.5.3. While some numerical methods such as XFEM [100] specialize in the numerical treatment of discontinuities within elements, they are not an appealing option to use for problems involving surface growth since each discrete growth increment introduces a new discontinuity in the fields, which becomes a burdensome task for a simulation with hundreds or thousands of time steps.

In some cases, elements bisecting the ungrown boundary may not contain any integration points in the growth region. This is typical for problems involving small time steps and/or growth increments relative to the element sizes near the boundary. Integration schemes which sample element nodes such as the two-dimensional 3×3 Gauss-Lobatto quadrature rule can capture the growth extension fields of quantities defined at integration points for any arbitrary time step, as is illustrated in Figure A.6. This numerical scheme was used in Section 4.5.3. It is important, however, to note that any numerical quadrature scheme will entail a finite integration error since the locations and weights of these methods are derived from smooth polynomials.

[4]Some fields such as the mass density have a specified value independent of the fields in the existing body, which produce discontinuities along the growth interface. Other fields depend on the state of the body prior to growth. For instance, the material velocities are assumed to have extensions that are constant in the growth region with a value equivalent to that of the nearest node of the ungrown mesh. In this case, the field is continuous along the growth interface, but consists of a discontinuous slope.

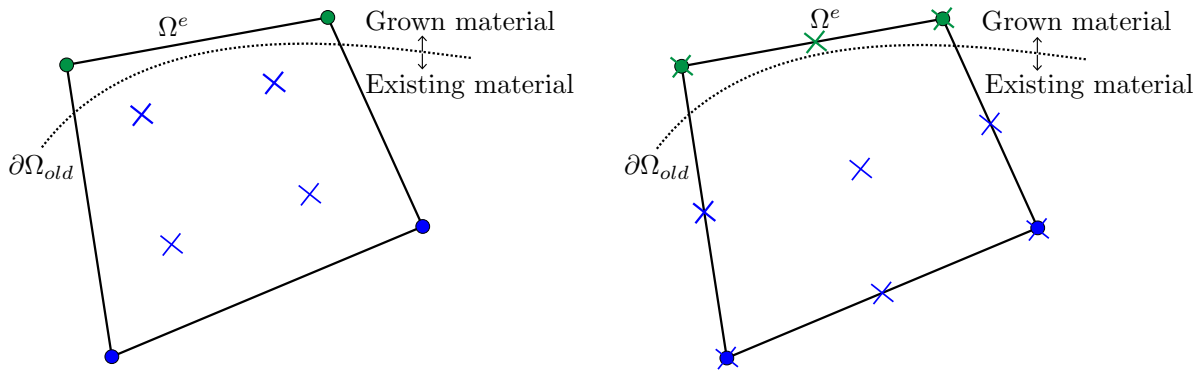

Figure A.6: *Node and integration point flagging for* 2×2 *Gauss-Legendre quadrature (left) and* 3×3 *Gauss-Lobatto quadrature (right)*

Algorithm 5: Front-tracking for nodes

for $\tilde{\mathbf{x}}_i \in \tilde{\Omega}$ **do** ▷ Interior and boundary nodes in intermediate configuration
  Compute $\mathbf{x}_{\partial\Omega_{old}}$ ▷ Closest point projection of $\tilde{\mathbf{x}}_i$ onto surface of ungrown mesh
  Compute $\boldsymbol{r}_x = \tilde{\mathbf{x}}_i - \mathbf{x}_{\partial\Omega_{old}}$
  Compute $\boldsymbol{n}_{\partial\Omega_{old}}$ ▷ Outward-facing unit normal at $\mathbf{x}_{\partial\Omega_{old}}$
  if $\boldsymbol{r}_x \cdot \boldsymbol{n}_{\partial\Omega_{old}} > 0$ **then** ▷ Growth
    Flag node at $\tilde{\mathbf{x}}_i$ as growth node
    Prescribe growth extension
  else if $\boldsymbol{r}_x \cdot \boldsymbol{n}_{\partial\Omega_{old}} < 0$ **and** $\mathbf{x}_i \in \partial\Omega$ **then** ▷ Resorption
    Flag node at $\tilde{\mathbf{x}}_i$ as resorption node
    Prescribe resorption extension
  else if $\boldsymbol{r}_x \cdot \boldsymbol{n}_{\partial\Omega_{old}} == 0$ **and** $||\mathbf{v}_g|| > 0$ **then** ▷ Tangential resorption
    Flag node at $\tilde{\mathbf{x}}_i$ as resorption node
    Prescribe resorption extension
  end if
end for

A.6 Contact Constraint under Surface Accretion

Contact between a deformable body and a rigid barrier is enforced via the penalty method for normal contact [101, Chapter 6]. The weak balance of linear momentum in Equation (3.5) contains an additional term, and hence becomes

$$\int_{\mathcal{R}^{\tau+t}} \left(\boldsymbol{\xi} \cdot \rho \dot{\mathbf{v}} + \frac{\partial^s \boldsymbol{\xi}}{\partial \mathbf{x}} \cdot \boldsymbol{T} \right) dv \;=\; \int_{\mathcal{R}^{\tau+t}} \rho \boldsymbol{b} \; dv + \int_{\Gamma_q^{\tau+t}} \left(\boldsymbol{\xi} \cdot \bar{\boldsymbol{t}} - \epsilon \boldsymbol{\xi} \cdot \boldsymbol{g}_{\bar{n}} \right) da \,, \tag{A.13}$$

where $\epsilon > 0$ is a user-specified penalty parameter and $\boldsymbol{g}_{\bar{n}}$ is the normal gap vector defined as

Algorithm 6: Front-tracking for integration points in elements

for $\Omega^e \in \tilde{\Omega}$ **do** ▷ Elements in intermediate configuration
  for $\tilde{\mathbf{x}}_{ip} \in \Omega^e$ **do** ▷ Integration points of an element
    Compute $\mathbf{x}_{\partial\Omega_{old}}$ ▷ Closest point projection of $\tilde{\mathbf{x}}_{ip}$ onto surface of ungrown mesh
    Compute $\boldsymbol{r}_x = \tilde{\mathbf{x}}_i - \mathbf{x}_{\partial\Omega_{old}}$
    Compute $\boldsymbol{n}_{\partial\Omega_{old}}$ ▷ Outward-facing unit normal at $\mathbf{x}_{\partial\Omega_{old}}$
    if $\boldsymbol{r}_x \cdot \boldsymbol{n}_{\partial\Omega_{old}} > 0$ **then** ▷ Growth
      Flag node at $\tilde{\mathbf{x}}_i$ as growth node
      Prescribe growth extension
    end if
  end for
end for

$$\boldsymbol{g}_{\bar{n}} = \begin{cases} \left[(\mathbf{x}_{\partial\mathcal{R}} - \bar{\mathbf{x}}) \cdot \bar{\boldsymbol{n}}\right]\bar{\boldsymbol{n}} & \text{if } (\mathbf{x}_{\partial\mathcal{R}} - \bar{\mathbf{x}}) \cdot \bar{\boldsymbol{n}} < 0 \\ \mathbf{0} & \text{otherwise .} \end{cases} \tag{A.14}$$

In Equation (A.14), $\bar{\mathbf{x}}$ and $\bar{\boldsymbol{n}}$ are the position vector and unit outward facing normal on the fixed barrier (respectively), and $\mathbf{x}_{\partial\mathcal{R}}$ is a given position vector of a material point in the current configuration along the boundary $\partial\mathcal{R}$. The penalty term $\epsilon\boldsymbol{g}_{\bar{n}}$ in Equation (A.13) acts as a traction that prevents penetration of the boundary $\partial\mathcal{R}$, and hence, carries a negative sign (compressive) when the constraint is active.

As noted in [101, Chapter 6], the weak form in Equation (A.13) derives from the minimization of a potential (or Hamiltonian when kinetic energy is present) subject to the inequality constraint

$$(\mathbf{x}_{\partial\mathcal{R}} - \bar{\mathbf{x}}) \cdot \bar{\boldsymbol{n}} \geq 0 \,, \tag{A.15}$$

which imposes impenetrability. The penalty method approximates the contact constraint shown above with a traction that increases with the amount of penetration, and depends on the penalty parameter ϵ.

The time and space discretization leads to the following system of equations on the element level

$$\boldsymbol{M}^e \overset{\square}{\mathbf{v}}^e + \boldsymbol{F}^e_{int} - \boldsymbol{F}^e_{ext} + \boldsymbol{G}^e_c \;=\; \mathbf{0} \,. \tag{A.16}$$

The constraint vector is defined as

$$\boldsymbol{G}^e_c = \int_{\Xi^e} \epsilon (\boldsymbol{N}^e)^T \hat{\boldsymbol{g}}^e_{\bar{n}} \, da \,, \tag{A.17}$$

where $\Xi^e = \partial\Omega^e \cap \Gamma^e_c$, Γ^e_c is the contact surface, $and \hat{\boldsymbol{g}}_{\bar{n}}$ is the discretized gap vector of length $2\texttt{nen} \times 1$ in two dimensions defined at each node. The gap vector is evaluated for nodes that are flagged for contact, which is determined by performing an orthogonal projection of each node

along $\partial\mathcal{R}$ onto the boundary of the rigid barrier using the orthogonal projection and front-tracking algorithms described in Appendices A.2 and A.5. Rather than evaluating the set of contact nodes for each global Newton iteration, this set of nodes remains fixed for each given time step. With this modification, the discrete gap vector $\hat{\boldsymbol{g}}_{\bar{n}}$ is non-zero for all nodes initially flagged for contact, regardless of the orthogonal distance between a given node and the barrier for the current iterate. As argued in [101, Chapter 6], this modification alleviates the "flip-flopping" of nodes between contact and free, which leads to an improved convergence rate.

The iterative scheme in Equation (3.34) to update the velocities for a given iteration relies on the Fréchet derivative of the discrete gap function to form the tangent matrix, which for a given element e is expressed as

$$D\boldsymbol{G}_c^e(\mathbf{v}^{n+1}) = 2\beta\Delta t \int_{\Xi^e} \epsilon(\boldsymbol{N}_{\bar{\boldsymbol{n}}}^e)^T \boldsymbol{N}_{\bar{\boldsymbol{n}}}^e \, da \,, \tag{A.18}$$

where the element matrix $\boldsymbol{N}_{\bar{\boldsymbol{n}}}^e$ is defined as

$$\boldsymbol{N}_{\bar{\boldsymbol{n}}}^e = \begin{bmatrix} N_1^e \, \bar{n}_x & 0 & N_2^e \, \bar{n}_x & 0 & \dots & N_{nen}^e \, \bar{n}_x & 0 \\ 0 & N_1^e \, \bar{n}_y & 0 & N_2^e \, \bar{n}_y & \dots & 0 & N_{nen}^e \, \bar{n}_y \end{bmatrix} . \tag{A.19}$$

The tangent shown above holds both for small deformations as well as nonlinear kinematics in the present case, since the master surface that determines the contact tractions is a fixed barrier, which is consistent with the observations made in [102]. It is well-known that as the penalty parameter ϵ approaches infinity, the solution satisfying the approximate contact constraint in Equation (A.13) approaches the solution that globally adheres to the exact constraint in Equation (A.15) (as reviewed in [101, Chapter 6]). In practice, ϵ is set sufficiently high to prevent significant penetration, while remaining low enough to ensure the solvability of Equation (A.18).

For non-growing elastic bodies undergoing dynamic contact, the traction that prevents penetration through an external surface depends on the deformation and inertia of the body at the instant of contact. When a body undergoing surface growth reaches an external barrier, the contact tractions prevent further accretion of material. The ensuing stresses and deformation thus arise from the inability of the body to grow in a desired manner. In a temporally discretized setting, the intermediate configuration is subjected to surface growth and resorption without the effects of external barriers. In order to relate the mechanical fields occurring due to contact to the surface accretion, any penetration that occurs in the intermediate configuration is pushed away from the barrier via the contact tractions arising from $\boldsymbol{G}_c$, as is illustrated in Figure A.7. As the body is pushed away from the barrier, material can continue to accrete onto a growing surface facing the barrier leading to further penetration in the intermediate configuration of the subsequent steps. In reality, the surface growth rate can be affected by its inability to accrete in a given direction. This was illustrated with the cell migration example in Section 4.5.2, where the magnitude of the surface growth of the cell in the direction of the barrier decreased upon contact, leading to an eventual reversal of the growth velocity away from the contact surface.

The shock induced onto a body at the instant of impact during dynamic/inertial contact typically requires significant temporal refinement, since this discontinuous process in time is essentially approximated by numerical integration schemes such as Newmark-β that assume regularity in the

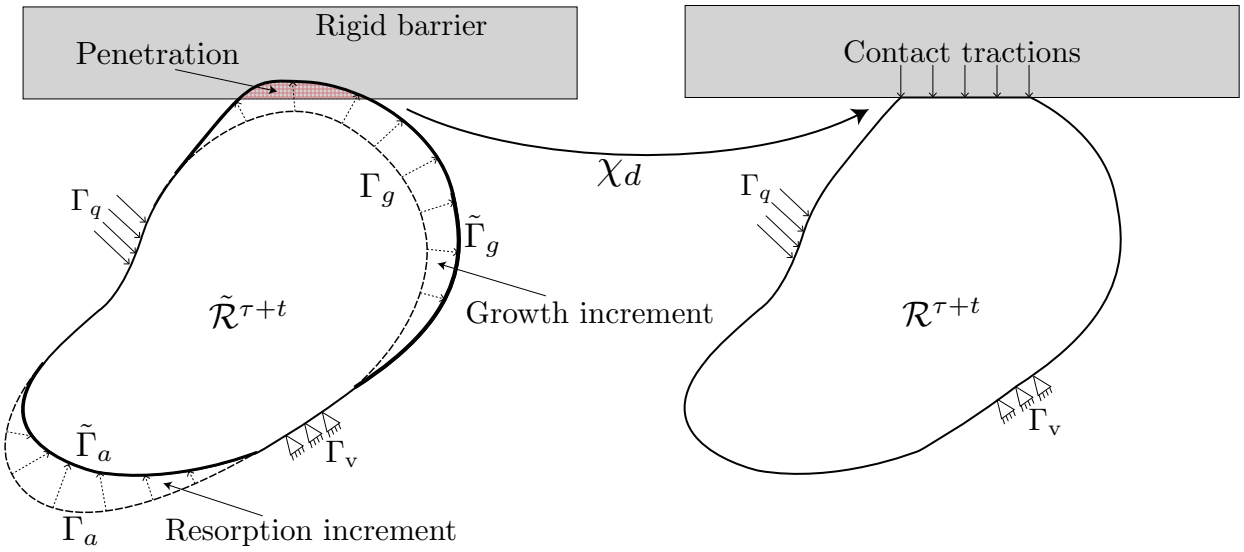

Figure A.7: *Enforcement of contact for a body undergoing surface growth through the deformation mapping from the intermediate configuration*

solution. However, the moments followed and preceded by impact may not be as sensitive to the time step, especially in circumstances such as the treadmilling cell in Section 4.5 where the body is not exposed to any external loads while moving between barriers. To improve the overall computational efficiency, the time step throughout the simulation is adapted based on the proximity of the treadmilling cell to the contact surface. When the cell approaches a barrier, the current coordinates of the body are obtained based on the growth and material velocities with a given time step. If contact occurs, the time step is reduced by a user-specified factor and the simulation step is restarted. This process repeats until none of the updated points with a reduced time step penetrate the barrier. If there are points on the boundary of the body that are in contact when the time step reaches a minimum value set by the user, the step proceeds without any further reduction in size. This continual reduction process allows the simulation time to gradually "slow down" as the body reaches the contact interface. When the body fully rebounds and is no longer in contact, the time step is increased until reaching the maximum user-specified value.

Appendix B

Code Structure

B.1 Overall Structure

The finite element code used in this dissertation was written in C++-14. The code relies on the Eigen library [103] for sparse matrix storage and linear algebra solution algorithms, the TinyXML2 library [104] for XML input file parsing, and gtest (Googletest) [105] for unit testing and black-box testing. Meshes are generated using gmsh [106]. The UML class collaboration and inheritance diagrams in Appendix B.3 are generated by Doxygen [107]. Results are output to text files in two forms:

1. Summary files contain limited information in certain time steps, based on the desired post-processed fields determined by the user.
2. Visualization files contain all pertinent information to visualize simulation results in Tecplot 360.

Namespaces encapsulate the different classes and functions based on their use. The description of each namespace is provided below:

- **Input/Output**: Input parsing, post-processing, and output for visualization
- **FEM**: Implementation of numerical quadrature, interpolation of nodal variables, wrapper methods for Eigen sparse matrices, and various other generic algorithms
- **Mesh**: Mesh optimization algorithms, storage of mesh parameters and data structures
- **Model**: Storage and implementation of model fields and balance laws
- **Debug**: Definitions and implementations of macros for unit tests and black-box tests for use with gtest

The main procedural class/method descriptions and other primary data structures are provided below:

- **MeshBase**
  - Stores array of element nodes, node neighbor lists, node element lists, element/surface connectivity arrays, and all mesh parameters
  - Performs mesh optimization, orthogonal projections, and front tracking procedures
- **ModelBase**
  - Derives from MeshBase
  - Primary class for storing and updating all field variables such as density, velocity and displacement
  - Primary implementer of surface growth and resorption
  - State is deep-copied for use in time integration procedures. The instance named old_model contains the state (implemented purely as a "const" class in every method where it is called) at the old time step t_n when updating to the new time step t_{n+1} whereas the trial_model instance is used in the iterative/staggered procedures to update the trial fields.
- **ModelParams**
  - Public data structure storing relevant parameters defining the model in ModelBase
  - Some parameters include time step, material constants and type, number of quadrature points, contact parameters, and various other factors
- **ModelArrays/ModelSurfArrays**
  - Stores, substructures, and updates sparse matrices used for solving bulk and surface balance laws and L_2-projections
- **ScalarParam/VectorParam**
  - Data structure storing the nodal arrays of scalar, and vector fields
  - Contains methods for interpolating fields and their derivatives at a point in a given element
- **Tensor/Tensor4**
  - Data structures storing a single second-order or fourth-order tensor
  - Contain overridden operators to handle tensor arithmetic
- **ScalarElemParam/TensorParam/Tensor4Param**
  - Data structure storing the global arrays of scalar, second-order, and fourth-order tensor fields defined at the integration points

- **ScalarVar/VectorVar**
  - Derive from ScalarParam and VectorParam
  - Data structure storing scalar and vector primary variables that are solved for
  - Contain linear and nonlinear solver parameters
- **MaterialBase**
  - Abstract base class with virtual methods defined for linear elastic, hypoelastic, neo-hookean, and viscoelastic materials
  - Derived material classes are instantiated through the polymorphic factory design pattern
  - Stores and updates element-level quantities such as the Cauchy stress and deformation gradient, and computes element tangent matrices
  - Scope is limited to time integration procedure
- **ChemicalKineticsBase**
  - Abstract base class with virtual methods defined for the following types of chemical kinetics: elastic brownian ratchet, simple nucleation-dissociation, Meinhardt activator-inhibitor-depleted model, and activator-depleted model
  - Derived chemical kinetics classes are instantiated through the polymorphic factory design pattern
  - Stores and updates surface element-level quantities such as surface specie concentration, and computes surface element tangent matrices
  - Scope is limited to time integration procedure
- **ContactImplementer**
  - Performs methods to track nodes in contact and compute contact tractions and tangent matrix
  - Scope is limited to time integration procedure
- **ModelFollowerTangent**
  - Computes tangent for nodes with imposed follower loads
  - Scope is limited to time integration procedure
- **ModelCore**
  - Top-level implementation class of ModelBase
  - Operates on a single unique instance of ModelBase to run simulation
  - Generates and outputs post-processed fields

B.2 UML Sequence Diagrams

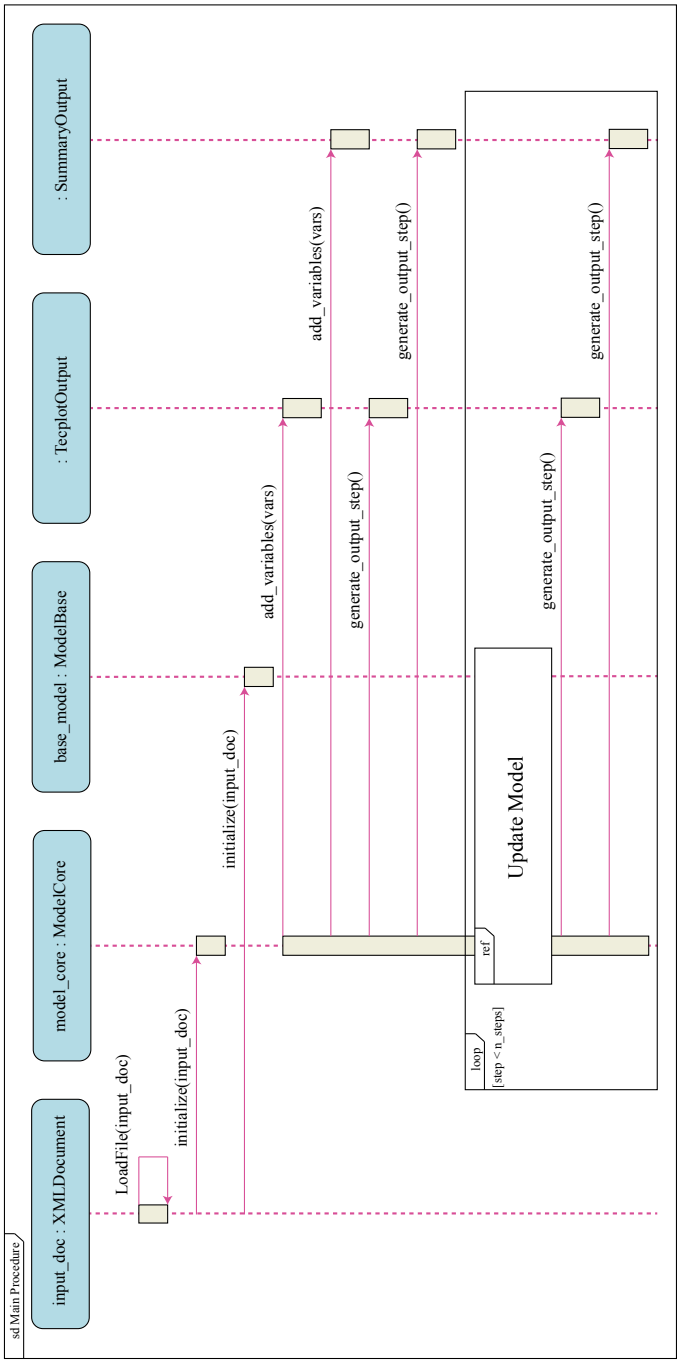

Figure B.1: *UML sequence diagram of main procedure*

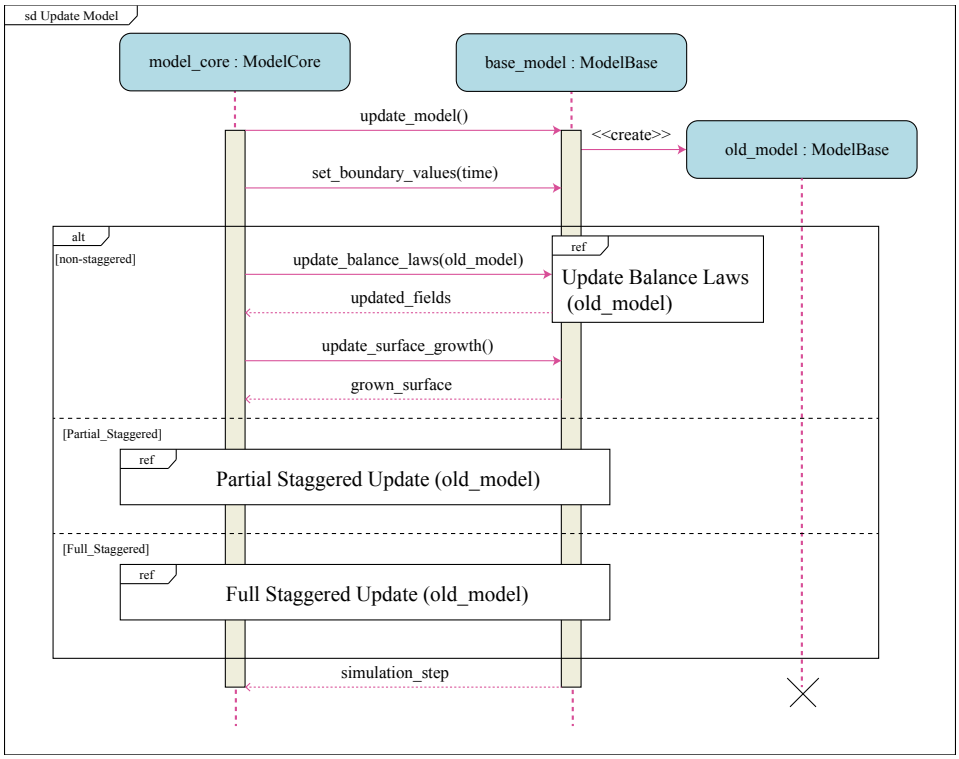

Figure B.2: *UML sequence diagram of update model procedure*

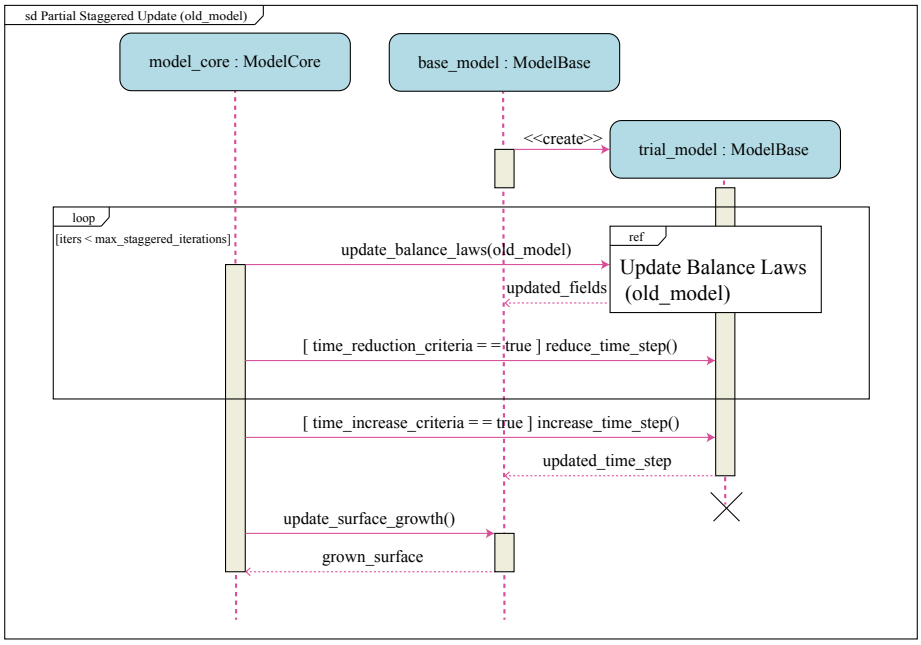

Figure B.3: *UML sequence diagram of partial staggered procedure*

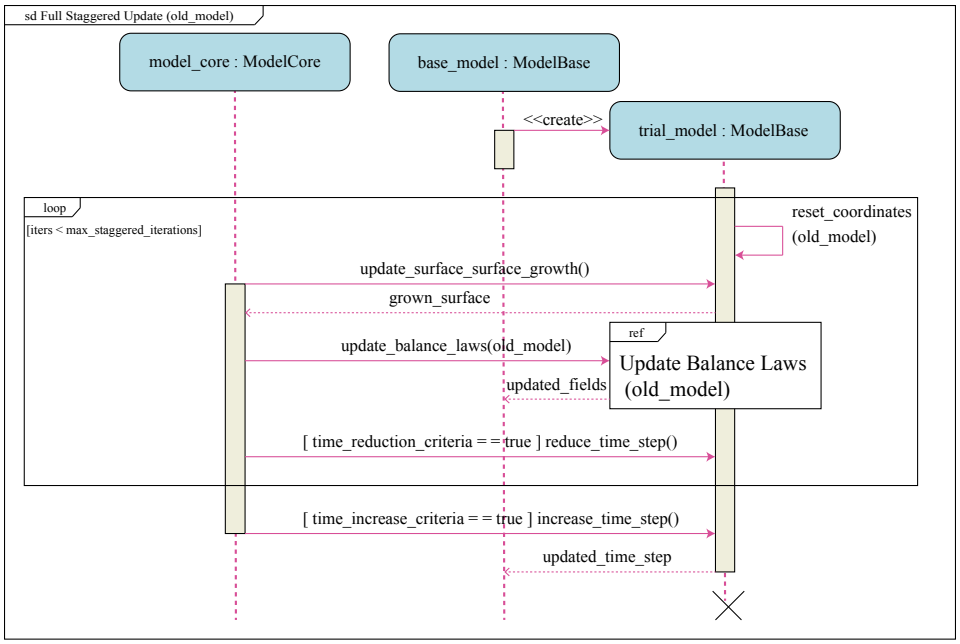

Figure B.4: *UML sequence diagram of full staggered procedure*

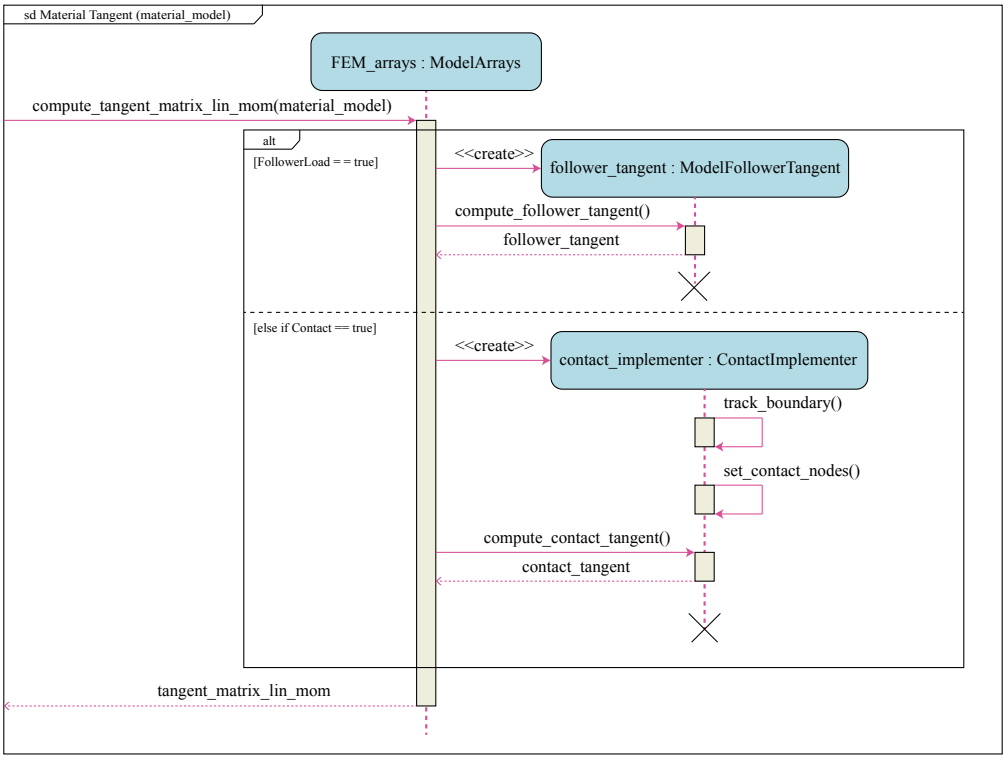

Figure B.5: *UML sequence diagram of material tangent update procedure*

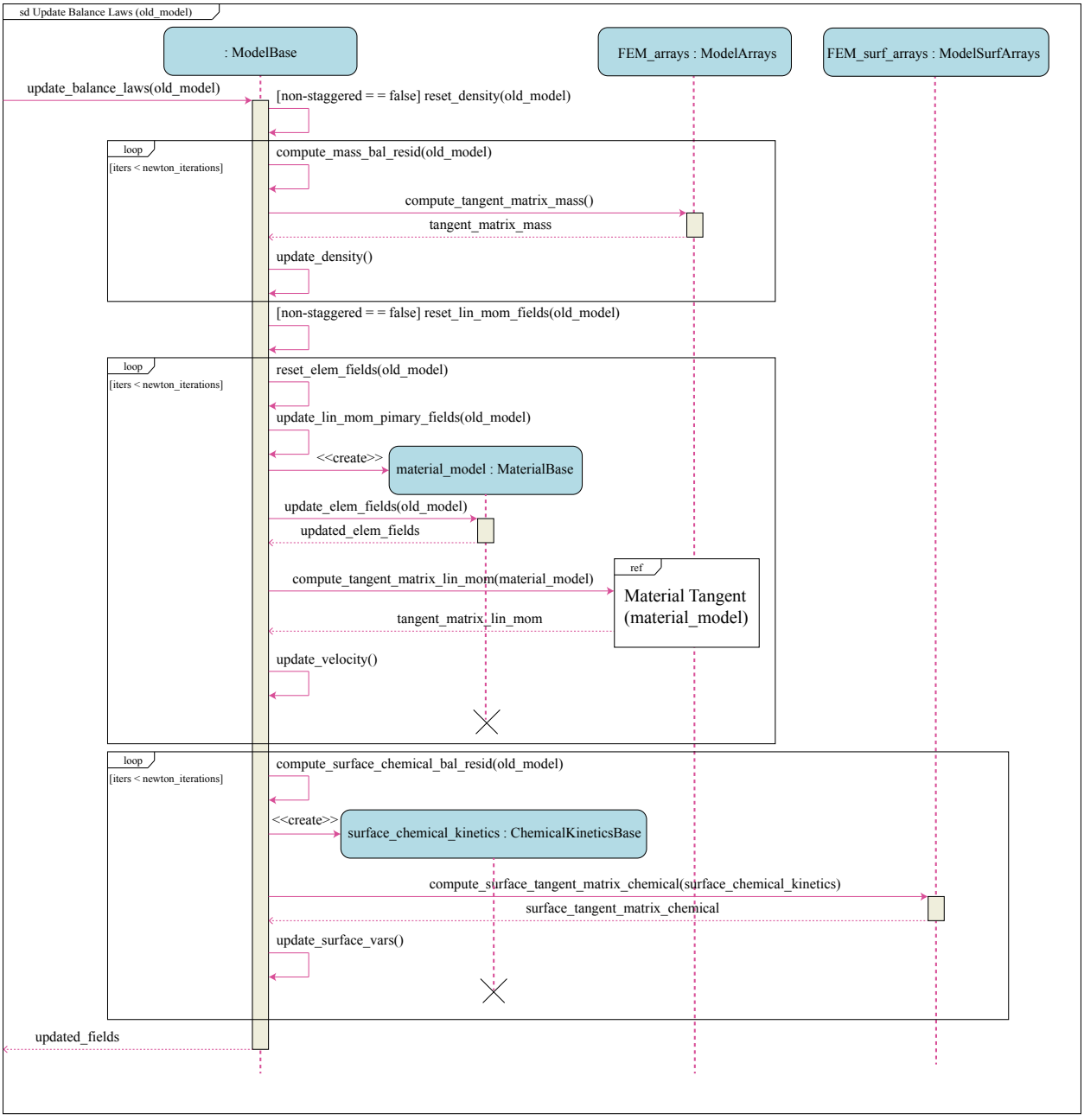

Figure B.6: *UML sequence diagram of balance laws update procedure*

B.3 UML Class Diagrams

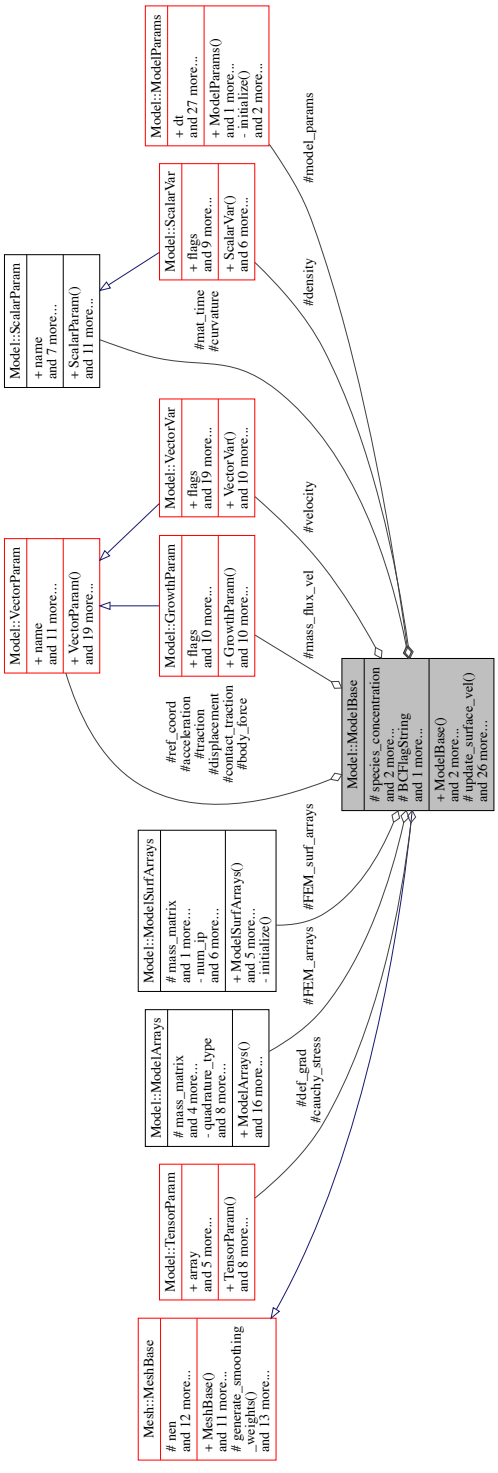

Figure B.7: *Condensed UML collaboration diagram of ModelBase class (diagrams of data structures in red boxes are truncated for clarity)*

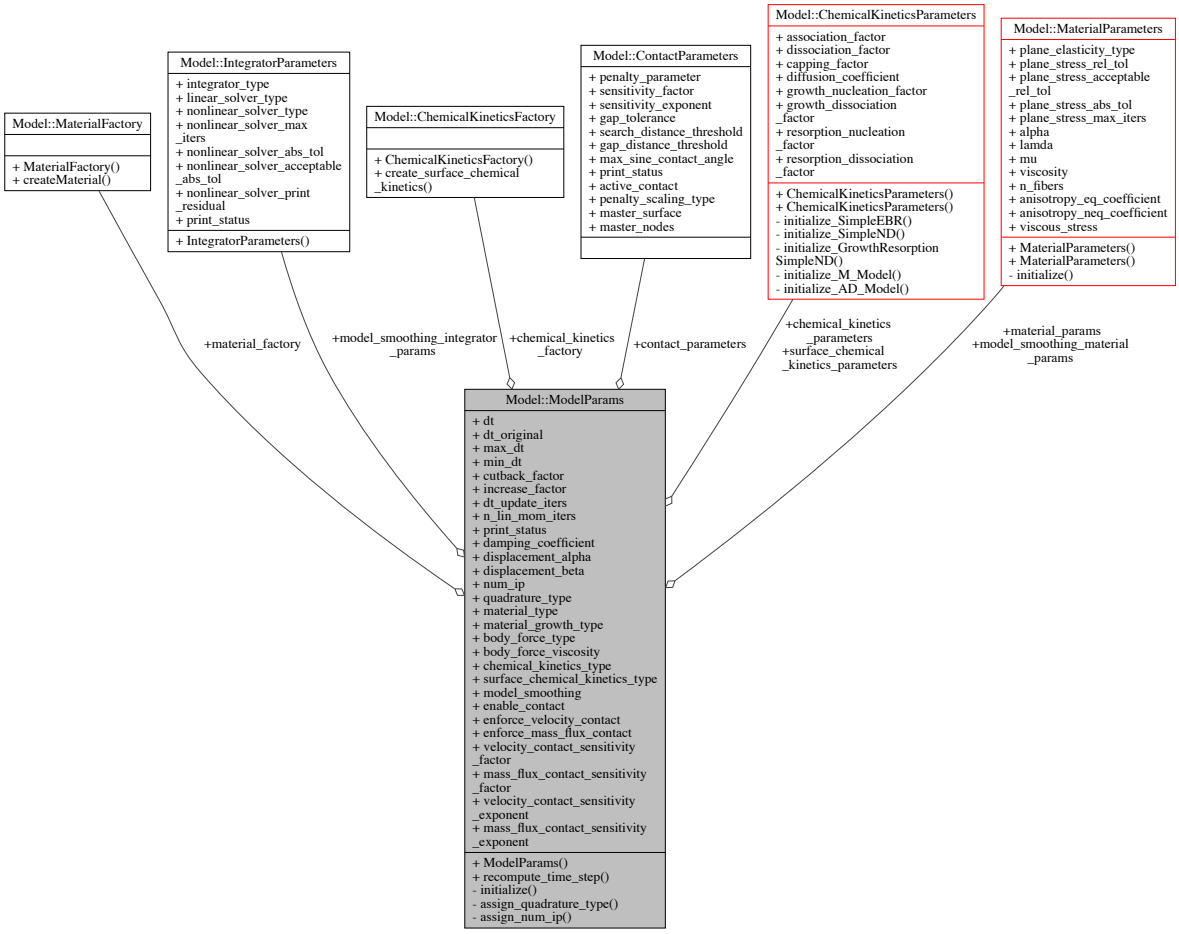

Figure B.8: *UML collaboration diagram of ModelParams class (diagrams of data structures in red boxes are truncated for clarity)*

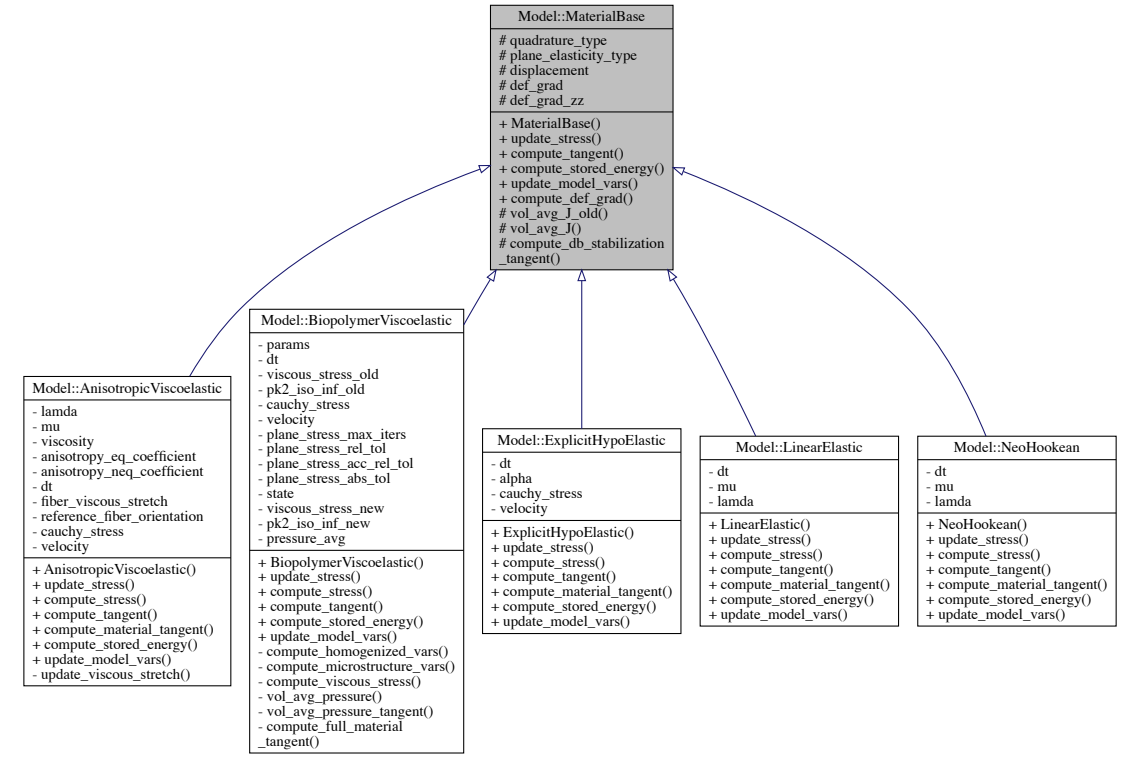

Figure B.9: *UML inheritance diagram of MaterialBase class*

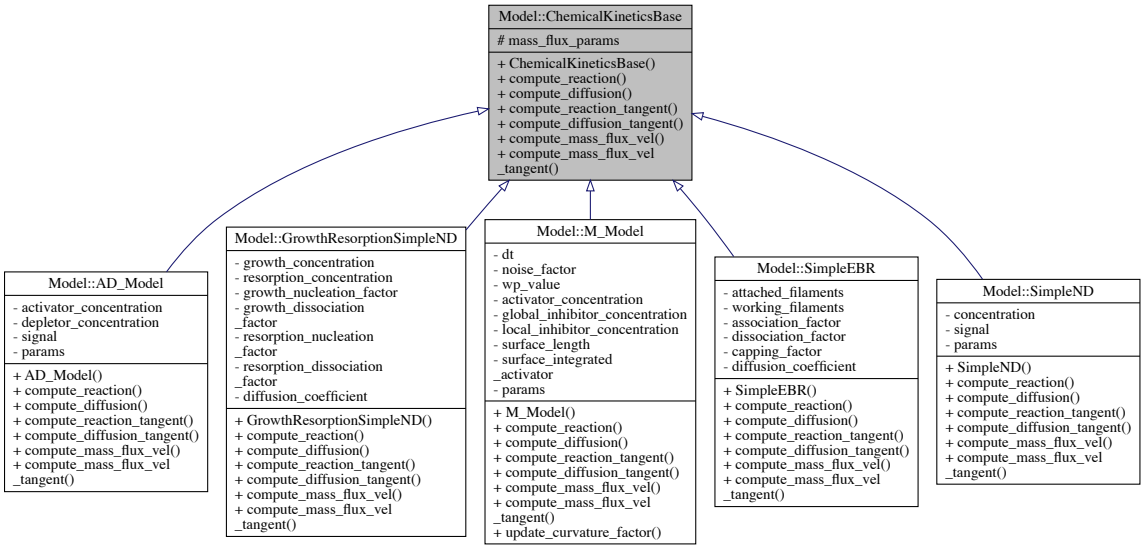

Figure B.10: *UML inheritance diagram of ChemicalKineticsBase class*